Study of Spectral Sensing using Electro-Optic Films

A Thesis

Submitted to the Faculty

of

Drexel University

by

Kashma K. Rai

in partial fulfillment of the

requirements for the degree

of

Doctor of Philosophy in

September 2009

Acknowledgement

Foremost I would like to express gratitude to my research advisor Adam Fontecchio for guiding me through the endeavors of graduate student life. His endless support and mentoring are truly remarkable!

I am fortunate to have worked with other graduate and undergraduate students at the Drexel Nanophotonics Group especially Dr. Hemang Shah, Sameet Shriyan, Jared Coyle, Dr. Anna Fox, David Delaine and Ben Pelleg with whom I have interacted over the years. Outside the lab graduate students Elina Vitol and Anbu Elanchezian have enriched my time at Drexel.

Collaboration with Dr. Claudio Zannoni and his research group at University of Bologna has deeply enhanced my learning experience. I am appreciative of him and his lab members Dr. Corrado Bacchiocchi, Isabella Miglioli, Dr. Ilaria Vecchi and Dr. Alberto Arcioni for inviting me to their lab and making my stay with them memorable and constructive.

The skilled personnel at Drexel Centralized Research Facility need a special mention for extending their help and tireless maintenance of equipment vital to my research.

On a personal level I have the deepest regards to my family, above all my parents Ramdas and Shobha Rai for their enduring belief in me, excessive to my abilities. Lastly, I am indebted to my husband Rajat who has been an unstinting friend to me for more than a decade.

Table of Contents

List of Tables

List of Figures

Abstract

Study of Spectral Sensing using Electro-Optic Films

Kashma K. Rai

Advisor: Adam K. Fontecchio, Ph.D.

Fundamental studies on light interacting with liquid crystals (LCs) and polymers have led to innovative application like the omnipresent LCDs, revolutionizing the display industry. This thesis focuses on manipulation of optical propagation through LC/polymer two phase composite material set and in-depth understanding of these systems by studying their morphology and microscopic interactions for multi-wavelength sensing applications.

Holographically formed Polymer Dispersed Liquid Crystals (HPDLCs) are the composite photorefractive material used in this work. They consist of LC nanodroplets confined in a polymer matrix, arranged in periodic planes. Applying an electric field across them modifies their periodic refractive index to a uniform refractive index state, due to LC realignment. This transforms the reflective HPDLCs into an optically transparent state.

Fabricating and assembling HPDLCs in different configurations enables wavelength filtering by controlling their optical lineshape output, for wavelength sensing applications. To increase the range of wavelengths spanned, these electro-optic thin films are arranged in serial and parallel design. A novel dynamic time multiplexing technique is used to improve the spectral range of individual HPDLC unit.

These types of field controllable HPDLC wavelength filtering devices have remote sensing, imaging spectrometry applications like hyperspectral and multispectral imaging to detect specific spectral signature of an unknown remote object source. Comparing the detected spectra to a database of known spectral fingerprints enables

identification of the unknown entity.

To further fundamentally comprehend the LC polymer interaction in HPDLC systems structural analysis data using microscopy and spectroscopy techniques is presented. To interpret the nano-scale structure accurately and better understand the confined LC behavior, variable pressure scanning electron microscopy and electron spin resonance spectroscopy is used here for the first time. Berreman 4×4 matrix technique and a phenomenological diffusion model are presented to model and predict their optical output behavior and their multipart wavelength lineshapes.

In summary this dissertation focuses on study of multi spectral sensing using HPDLCs, their fundamental studies along with modeling their behavior.

1. Scope of this dissertation

Confined liquid crystals (LCs) in diverse enclosures are extensively used in emerging electro-optic technologies. In this work optical propagation through LCs confined in a polymer matrix system are extensively studied for wavelength sensing application along with basic fundamental studies of these systems and theoretical analysis.

Wavelength sensing techniques such as remote sensing involve identifying distant objects by recording and detecting signals radiated from them, using sensors. These sensors positioned on land or space measure and analyze most frequently the electromagnetic spectral fingerprints of the object either as discrete intervals or continuous bands of electromagnetic radiation.

Remote wavelength sensing techniques such as multispectral and hyperspectral imaging have been used for hundred of applications such as investigation of the presence of vegetation, water, rocks, minerals etc. Here the signature spectral content measured such as scattering, reflectance, transmittance from the remote objects can be used to better classify and identify them by comparing them to spectral fingerprints of known objects.

Multispectral sensors measure bands of frequency and the band intervals are either discrete or overlapping. These are typically either measured by a series of sensors or sometimes by a single sensor. For example NASA and U.S. Geological surveys jointly managed satellite LANDSAT 5 launched in 1982 had multispectral sensor known as multispectral scanner(MSS) that recorded 4 spectral bands in the regions of blue, green, red and near-infrared with each of the band spanning a wavelength range of 100 nm. Hyperspectral imaging is a more advanced form where a typical a sensor measures narrower bands resulting in improved resolution. For example one of the earliest hyperspectral airborne sensors is NASAs AVIRIS(Airborne Visible/ Infrared

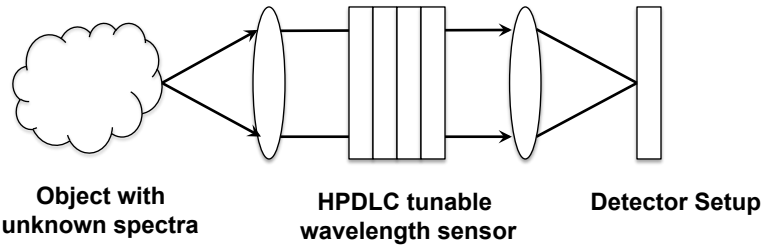

Figure 1.1: Demonstration of HPDLC filtering concept for wavelength sensing application

Imaging Spectrometer) with a band spectral resolution of 10 nm.

Many inventive technologies are being researched to realize the full potential of spectral imaging techniques with focus on factors like reducing the size of the sensors, complexity, cost, data processing and improving aspects like resolution and time response to gather spectra.

Electrically reconfigurable holographic polymer dispersed liquid crystals(HPDLCs) possess desirable properties such as ability to be nanofabricated, high color purity, fast electrical response resulting in faster data acquisition, capability of filtering wavelengths in the range from ultraviolet to infrared and detection ability of only required wavelengths, to function as opto-electrical sensors for target applications. For example a botonist working remotely on site to detect the presence of specific vegetation spectral features can use the small footprint, simple HPDLC based sensor designed to detect particular spectral fingerprints for a quick on location analysis.

In this dissertation the composite polymer/LC photorefractive HPDLCs are explored in detail for their spectral filtering ability for sensing applications. They manipulate incident light depending on their periodic grating structure and they reflect or transmit a particular wavelength of light based on application of field bias across them. Figure 7.1 shows an example of HPDLCs functioning as a spectral sensor. Here light reflected from a remote source is incident on a tunable HPDLC wave-

length filter stack and the transmitted intensity is measured by a detector setup such as a CCD detector. The tunable filter stack consists of multiple wavelength filtering HPDLCs placed adjacent to each other. Having a stack of HPDLCs that can selectively transmit or reflect multiple wavelengths gives the desired wavelength controllability, along with higher device sensitivity and reliability including an added advantage of lightweight optics.

To develop the wavelength sensing application using HPDLCs three techniques are chiefly used in this dissertation, which manipulates their fabrication and arrangement:

- Spatial multiplexing fabrication resulting in separate HPDLC units in a single layer
- Parallel stacking of HPDLC units adjacent to each other
- Dynamically varying the fabrication setup during HPDLC grating fabrication

The optical output from HPDLCs are analyzed using modeling techniques to predict their behavior and theoretically analyze their grating morphology further. The two techniques used are:

- Berreman 4×4 matrix analysis
- Phenomenological diffusion model

Liquid crystals confined in the polymer HPDLCs vary from their bulk like behavior. Understanding their morphology and confinement effects improves our understanding of the nature of HPDLCs for employing them for sensing and other applications. Lastly this dissertation also introduces two new types of experimental characterization techniques in imaging and spectroscopy which enable better fundamental understanding of optical interaction in these material system, namely:

Imaging technique:

- Variable pressure scanning electron microscope imaging(VPSEM)
- Environmental scanning electron microscope imaging(ESEM)

Spectroscopy technique:

• Electron spin resonance spectroscopy(ESR)

Thesis Outline

The outline of the thesis begins with HPDLCs basics, followed by novel characterization techniques to analyze HPDLCs and indepth investigation into wavelength sensing application.

The introductory Chapter 2 starts with a review of the two chief raw materials of HPDLCs namely liquid crystals(LCs) and polymers. Polymer dispersed liquid crystals(PDLCs), which are precursors to HPDLCs are presented followed by the holography technique to create holographically formed PDLCs or HPDLCs. Their properties and some of the important characterization tools used to gain an insight into these properties are discussed at the end of this chapter.

The two standard recipes of HPDLCs used throughout this dissertation and the holography setup used to fabricate them are detailed in the beginning of Chapter 3. This is followed by review of traditional experimental analysis techniques.

Chapter 4 details the two new types of experimental analysis techniques for morphological analysis of HPDLCs namely variable pressure/enviromental SEM and electron spin resonance spectroscopy techniques and their significant results.

The focal points of Chapter 5 is the theoretical work for predicting the optical response of HPDLCs. Here the Berreman 4×4 method is introduced for wavelength prediction and analysis.

Stacking, spatial fabrication of HPDLCs and dynamic time multiplexing method of fabrication are introduced in Chapter 6 for reflection wavelength lineshape manipulation. Their analysis is performed here using the phenomenological diffusion model and the Berreman technique for modeling the reflected wavelength.

Some of the application for HPDLCs by manipulating the reflected wavelength are

considered with respect to imaging and pressure sensing in Chapter 7 and Chapter 8 concludes all the salient points of this research work.

This research work focuses on the real world application development of HPDLCs for wavelength sensing applications by manipulating the reflected wavelength lineshape and theoretical prediction of the HPDLC lineshapes along with microscopic studies of their properties to interpret their macroscopic characteristics.

2. Introduction

Holographically-formed Polymer Dispersed Liquid Crystals(HPDLCs) are volume holograms consisting of photopolymers and liquid crystals(LCs) fabricated using holography techniques. An overview of LC, polymer, LC/polymer composites, polymer dispersed liquid crystals(PDLCs), holography fabrication, HPDLCs and their properties is presented here. This is followed by an introduction to some of the experimental analysis technique used extensively in the dissertation.

2.1 Liquid Crystals

In this section an introduction to different type of LCs with specific emphasis on nematic type LC and its physical property is described. Austrian botanist Friedrich Reinitzer is usually credited with the discovery of LCs in 1988[1]. He experimented with a cholesteric substance and observed its change to a cloudy liquid and then a clear liquid with increasing heat. Initial research on LCs was mainly theoretical work without any practical applications. However shortly before 1960 there was intense interest in application driven understanding of LCs. It was discovered that the LCs could detect small changes in parameters such as temperature, electromagnetic waves and mechanical stress paving the wave for multiple application development. In 1968 scientists at RCA demonstrated the first prototype of LCDs.

LCs are a class of materials which exhibit an intermediate phase between the solid and liquid phase. They flow like liquids and are ordered like solids. They can be broadly divided into two categories namely lyotropic and thermotropic LC. In both these cases anisotropic molecules cause orientational and sometimes positional order. In lyotropic LCs the solubility of different parts of LC molecules are different

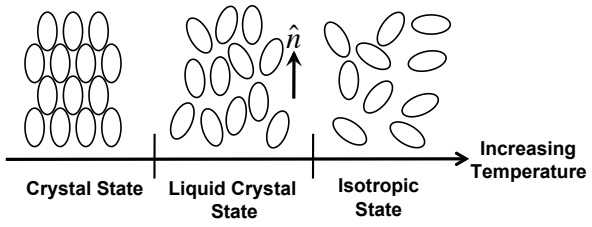

Figure 2.1: Oval shaped thermotropic LC molecules displaying crystal, liquid crystal and isotropic states with increasing temperature

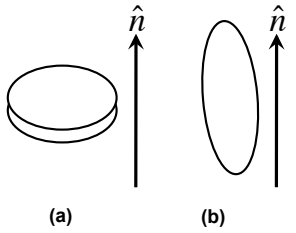

Figure 2.2: LC molecule displaying shape anisotropy. (a) Disc-like or discotic LC molecule and (b) rod-like or calamatic LC molecule

whereas thermotropic LCs have shape anisotropy. Lyotropic LCs consist of two or more compounds and the LC phase is dependent on their concentration as well as temperature[2]. This type of LC behavior is found in soap molecules in water and is responsible for the soap's ability to remove dirt. The cell membrane structure in the human body is due to the lyotropic liquid crystalline phase of the phospholipids and water molecules in the body.

In thermotropic LCs the LC phase transition occurs solely due to temperature variation in a compound and is a topic of interest in this thesis work. At high temperature the molecules in the thermotropic LCs are in an isotropic state, at low temperature they are in a crystalline state and at intermediate temperature range they form the liquid crystalline phase as shown in Figure 2.1. The liquid crystal molecules have a preferred direction of orientation called the director represented by

the unit vector $\hat{\mathbf{n}}$ in the figure. Here the director can be described as pointing in either of the two opposite directions. Thus there is no difference between the director pointing in $\hat{\mathbf{n}}$ and $-\hat{\mathbf{n}}$. The thermotropic type LCs can be broadly categorized into two main types based on shape anisotropy as disc-like or discotic and rod-like or calamatic LCs. This is illustrated in Figure 2.2.

The discotic liquid crystal molecules tend to orient perpendicular to the plane of the LC molecule indicated by the direction $\hat{\mathbf{n}}$ as shown in Figure 2.2(a). Based on the type of discotic LC orientation they can be categorized as nematic and columnar[2].

The calamatic liquid crystals shown in Figure 2.2(b) are more common compared to the discotic liquid crystals. They can be classified as smectic, chiral and nematic based on the arrangement of their molecules. Smectic LC molecules are arranged in layers and thus have positional order along with orientational order. Chiral LCs possess chirality. Here the intermolecular forces between the molecules tend to orient them at an angle with each other. The director of the molecules rotate throughout the sample specimen along an axis. Nematic LCs have a orientational order along a fixed director and do not have positional order.

There are other types thermotropic LCs such as polymer LCs and LCs exhibiting blue phase(it exist in some chiral LCs between chiral phase and isotropic phase) because of their wavelength selective Bragg structure[2], which are beyond the scope of this dissertation. Calamatic nematic LCs are the main topic of this dissertation and explored in detail in the next section.

2.1.1 Thermotropic Rod-Like Nematic Liquid Crystals

These type of LCs have anisotropically shaped molecules that have a preferred direction of orientation without positional ordering. This section quantifies their orientation order, discusses the alignment effect on LCs and also presents review on

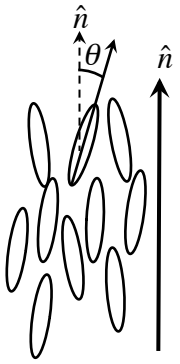

Figure 2.3: Orientation of nematic LC molecules

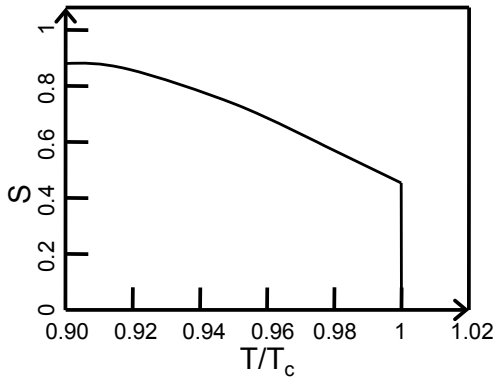

Figure 2.4: Plot of order parameter S of nematic LC as a function of temperature

LC anisotropy properties.

Order Parameter

Let θ be the angle between the LC molecule long axis and director $\hat{\mathbf{n}}$ as shown in Figure 2.3. The order parameter S which indicates the level of order or disorder in a liquid crystal material is defined as [3]

$$S = \left\langle \frac{3\cos^2\theta - 1}{2} \right\rangle \tag{2.1}$$

Here the bracket indicates either an average value over an interval of time for a particular LC molecule or the average at a particular time instant for many LC molecules.

From Equation 2.1 it can be deduced that for perfectly arranged LC molecules aligned along the director direction $\theta = 0$ results in $S = 1$ and for completely disordered orientation of LC molecules θ randomly varies from 0 to 90° and the average value $S = 0$. Thus at lower temperature when an LC phase nears the crystalline phase the order parameter nears the value of 1. At higher temperature when the LC almost reaches the isotropic state the order parameter nears 0. This can be schematically shown in the plot of Figure 2.4 for a LC material with order parameter in the range of 0.4 to 0.85. Here order parameter is plotted versus the ratio of temperature variation T and clearing temperature T_c. Temperature at which the LC material changes from LC state to isotropic temperature is know as T_c. From the plot it can be inferred that at lower T the $S = 0.85$. Increasing the temperature reduces the S until it reaches T_c where it transitions abrutly to $S = 0$. At temperatures above T_c, $S = 0$. This plot depicts LC material which exhibit first order transition marked by abrupt transition of S at T_c. In material that show second order transition there is a gradual change from LC phase to isotropic phase. To measure the value of S usually a macroscopic property of LC phase is studied. If the microscopic molecular changes are understood that cause these macroscopic property then the order parameters can be tracked. In this dissertation the order parameters of LC in confined geometry is studied using electron spin resonance techniques. Other methods such as X-ray scattering, Raman scattering, nuclear magnetic resonance are typically used to study the order parameter S.

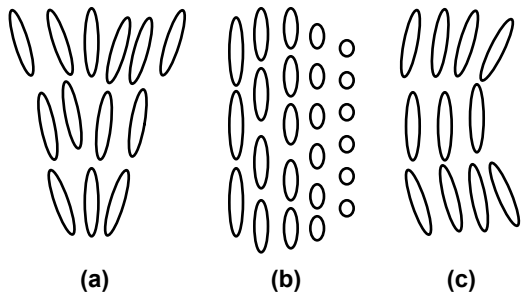

Figure 2.5: Nematics LCs showing (a)splay (b) twist and (c) bend distortions

Alignment of LCs

The alignment of the LC droplets inside polymer matrix is crucial to determine the optical properties of the HPDLCs.

In a bulk nematic LC medium the molecules exhibit a long range orientational order. However in the presence of external fields and confining surfaces the director orientation undergoes changes depending on the external forces. The LC director distortions undergoing splay, twist and bend distortions[3] as shown in Figure 2.5 can be quantized using the free energy equation. The Oseen-Zöcher-Frank equation determining the Helmholtz free energy per unit volume in vector notation is[3, 4]

$$F = \frac{1}{2}k_1 \left[\nabla \cdot \hat{n}\right]^2 + \frac{1}{2}k_2 \left[\hat{n} \cdot (\nabla \times \hat{n})\right]^2 + \frac{1}{2}k_3 \left|\hat{n} \times (\nabla \times \hat{n})\right|^2 \tag{2.2}$$

where k_1, k_2, k_3 are known as the splay, twist and bend distortion constants respectively. These three parameter determine how rigid the LC director orientational order is when exposed to external forces. Higher values of these parameters indicate higher LC order parameter.

When particular material surfaces (such as polymer in this dissertation) come in contact with LCs they force the nematic LC directors to change in a specific direction. When the director of the nematic LC is forced to lie perpendicular to surface

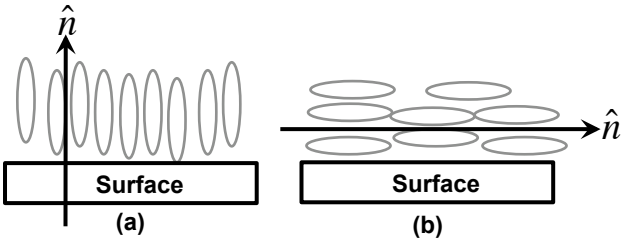

Figure 2.6: Illustration of alignment configuration of LC on a surface. (a) Homogeneous alignment of LC and (b) planar or homogeneous alignment of LC

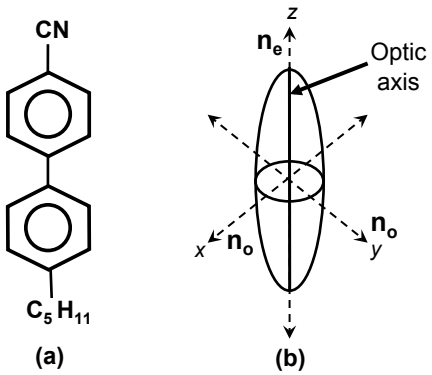

Figure 2.7: (a) Chemical structure of nematic 5CB LC and (b)representation showing refractive index anisotropy

of the material as shown in Figure 2.6(a) the alignment is termed as homeotropic. When the LC units lie parallel to the surface the alignment is termed as planar or homogeneous alignment as represented in Figure 2.6(b). The LC alignment effect in a polymer matrix will be discussed in detail with the discussion of electron spin resonance spectroscopy technique in Section 4.2

Anisotropy of LC

LC are dielectric material which orient in the direction of the external electric field applied. This property of the LC is used to modify the behavior of interaction

of light with LC. Reorientation of LCs for applied field is responsible for the uniform refractive index of the HPDLCs discussed in this dissertation and modification of their electro-optical property.

To examine the anisotropic nature of the LC, consider the chemical and optical representation of LC molecule 4-cyano-4'-n-pentylbiphenyl(5CB) shown in Figure 2.7 commercially called K15. It is the main ingredient of BL038 LC used throughout this dissertation. The chemical composition consists of two benzene rings bound by cyano group on one end and hydrocarbon chain C_5H_{11} at the other end. The chemical bonds along the long axis is different to the bonds formed perpendicular to it and results in two refractive indices in these different directions indicated as n_e and n_o in Figure 2.7(b). The long axis is known as the optic axis.

The anisotropy of the nematic LC molecules extends to properties such as refractive index, electric susceptibility and dielectric constant. The refractive index of nematic LC along the optic axis is called the extraordinary refractive index represented as n_e and the refractive index perpendicular to it is called the ordinary refractive index represented as n_o. n_o value is the same along any direction perpendicular to the optic axis as seen in the example shown in Figure 2.7(b) indicated by the xy plane. Since the LC considered here has only two refractive index it is called uniaxial LC. LCs having three different refractive indices are termed biaxial LCs which are beyond the scope of this dissertation.

Application of electric field across the nematic uniaxial LCs causes orientation changes in the director. This is due to the charge separation inside the LC molecules resulting in weak dipole moment which creates a net dipole in all the molecules exposed to this field. The net dipole moment per unit volume of the material termed as the polarization $\mathbf{P}$ of the material is proportional to the applied electric field vector $\mathbf{E}$ and is in the direction of the average dipole moment of individual LC molecules. For

nematic LCs the dipole moment is parallel to the long axis of the LC molecules and applying electric field cause alignment along this axis. The polarization parameter is represented as

$$\mathbf{P} = \varepsilon_0 \chi_e \mathbf{E}, \tag{2.3}$$

where the proportionality constants $\varepsilon_0 = 8.85 \times 10^{-12} \mathrm{C}^2/\mathrm{Nm}^2$ is the permittivity of free space and χ_e is the electric susceptibility of the material. The direction at which the field is applied to the director is an important factor to determine vector $\mathbf{P}$. The susceptibility value χ_e changes accordingly to $\chi_{||}$ or $\chi_{\perp}$ depending on whether it is quantified parallel or perpendicular to the director direction $\hat{\mathbf{n}}$.

The electric displacement vector $\mathbf{D}$ which is a measure of the electric field in a medium of polarization $\mathbf{P}$ is expressed as

$$\mathbf{D} = \varepsilon_0 \mathbf{E} + \mathbf{P} \tag{2.4}$$

This can be rewritten as

$$\mathbf{D} = \varepsilon \mathbf{E} \tag{2.5}$$

where $\varepsilon = \varepsilon_0 (1 + \chi_e)$. Here ε is the permittivity of the material across which the field is applied. The permittivity of the material in a direction parallel to the director and perpendicular to it is represented as $\varepsilon_{||}$ and $\varepsilon_{\perp}$ respectively. The permittivity or dielectric anisotropy is expressed as $\Delta\varepsilon = \varepsilon_{||} - \varepsilon_{\perp}$. The dielectric anisotropy decreases with increasing temperature and is proportional to the order parameter S[5].

Since the LC has two dielectric constants $\varepsilon_{||}$ and $\varepsilon_{\perp}$ in different directions, a propagating optical wave has two corresponding refractive indices $n_{||}$ and $n_{\perp}$. Since $n_{||}$ is the refractive index parallel to director and the optic axis is on an average parallel to the director in the nematic region of LC we can write $n_e \approx n_{||}$ and $n_o \approx n_{\perp}$. The optical anisotropy can be written as $\Delta n = n_{||} - n_{\perp}$. For the case of nematic LCs

$n_{\parallel} > n_{\perp}$ and the LC molecule has positive anisotropy.

The refractive indices are related to the dielectric constant by the relation $n_{\parallel} = \sqrt{\varepsilon_{\parallel}}$ and $n_{\perp} = \sqrt{\varepsilon_{\perp}}$ typically for optical wavelengths. Since the dielectric anisotropy directly follows the order parameter we can state that the order parameter varies as a function of $n_{\parallel}^2 - n_{\perp}^2$. A polarized light incident on this type of anisotropic sample of thickness d undergoes a phase change δ determined by

$$\delta = \frac{2\pi}{\lambda_0} \left(n_{||} - n_{\perp} \right) d \tag{2.6}$$

where $\lambda_0 = 3 \times 10^8 m/s$ is the wavelength in vacuum. When an incident light is incident on a LC in an arbitrary direction the ordinary and extraordinary refractive index experienced is

$$n_o = n_{\perp} \tag{2.7}$$

$$n_e(\theta) = \frac{n_{\parallel} n_{\perp}}{\sqrt{n_{\parallel}^2 \sin^2\theta + n_{\perp}^2 \cos^2\theta}} \tag{2.8}$$

Where θ is the angel between the long axis of LC along $n_{\parallel}$ and electric field polarization vector $\mathbf{E}$.

The next section is a brief review of polymers that interact with the nematic LCs described here to form complex phase separated structures.

2.2 Polymers

Transparent elastic polymers with phase separated nematic liquid crystal dispersions have attractive electro-optic properties for multitudes of application development. These polymer/LC composites are the key elements of this dissertation.

Natural and synthesized polymers are a vital part of our everyday life. For ex-

ample proteins are natural polymers and plastics are synthesized polymers. Natural polymers including materials such as cotton, leather and wool have been used since ancient times. The first truly synthetic polymer Bakelite, which spearheaded efforts for polymer material synthesis was created by Leo Baekeland in 1907. Bakelite found extensive commercial application for wide ranging electrical appliances[6]. However, the chemical structure of the polymers was hardly understood until the 1920s, when Herman Staudinger proposed the macromolecular hypothesis. Extensive research since then on the chemistry and kinetics to understand the structure, properties of polymers along with novel polymer synthesis have led to multitude of synthetic polymers products.

Chemically, polymer are long chain molecules consisting of repeating structural units called monomers. To create a polymer the monomer must attach to atleast two monomer units. Polymers are formed by two main methods namely addition or chain polymerization and step polymerization methods[7]. Among chain polymerization techniques free radical polymerization technique is employed here.

Chain Polymerization

The free radical chain polymerization technique undergoes three different stages namely initiation, propagation and termination.

In the initiation stage the initiator **I** reacts and absorbs the incident radiation with energy E=$h\nu$ to generate free radicals which can be written as $\mathbf{R}\cdot$. This reactive species usually attacks the monomer unit **M**, adds on to it to form reactive monomer unit $\mathbf{M}\cdot$. It can be symbolically represented as

$$\begin{aligned} \mathbf{I} + h\nu &\rightarrow \mathbf{R}\cdot \\ \mathbf{R}\cdot + \mathbf{M} &\rightarrow \mathbf{M}\cdot \end{aligned}$$

During the propagation process the reactive $\mathbf{M}\cdot$ attaches to other $\mathbf{M}$ units to form long chain reactive monomer units $\mathbf{M_x}\cdot$ resulting in rapid addition to create long polymeric chains. This is a very fast process and typically occurs in the fraction of a second. Here $\mathbf{x}$ represents the no of monomer units that have linked together.

$$\begin{aligned} \mathbf{M}\cdot + \mathbf{M} &\rightarrow \mathbf{M_2}\cdot \\ &\vdots \\ \mathbf{M_x}\cdot + \mathbf{M} &\rightarrow \mathbf{M_{x+1}}\cdot \end{aligned}$$

The termination of this reactive stage occurs either by combination or disproportionation process. In the combination type of termination two reactive growing polymeric units represented here as $\mathbf{M_x}\cdot$ and $\mathbf{M_y}\cdot$ react to eliminate the free radicals. Here $\mathbf{x}$ and $\mathbf{y}$ are the no. of monomeric units that combine to form a long chain polymeric unit of length $\mathbf{x+y}$. In the disproportionation process the radical from one long chain reactive polymer is moved to the other reactive polymer making them both unreactive. Symbolically it is represented as

$$\begin{aligned} \mathbf{M_x}\cdot + \mathbf{M_y}\cdot &\rightarrow \mathbf{M_{x+y}} \qquad \textit{Combination} \\ \mathbf{M_x}\cdot + \mathbf{M_y}\cdot &\rightarrow \mathbf{M_x} + \mathbf{M_y} \quad \textit{Disproportionation} \end{aligned}$$

HPDLCs having acrylate polymer as ingredient are synthesized using this technique.

Step Polymerization

This type of polymerization needs atleast two different kind of monomers with the right functional groups represented here as $\mathbf{M}$ and $\mathbf{N}$. In this type of reaction multiple monomeric units react with each other stepwise to form long chain polymers. This

reaction is typically slower the free radical polymerization technique. Symbolically it can be represented as

$$\begin{aligned} \mathbf{M + N} &\rightarrow \mathbf{MN} \\ \mathbf{MN + MN} &\rightarrow \mathbf{(MN)_2} \\ &\vdots \\ \mathbf{(MN)_x + MN} &\rightarrow \mathbf{(MN)_{x+1}} \end{aligned}$$

Thiolene polymer chemistry based HPDLCs are performed using this technique.

The next section discusses the formation and characteristic features of LC dispersion in polymer matrix.

2.3 Liquid Crystal/ Polymer Composites

Interesting characteristic properties of LC droplets in polymer matrix have motivated their scientific understanding and technological application development[8]. An important feature is the variation of the optical property due to realignment of dielectric LC by applying an external field in these systems. This section is a brief review of these composite structures. Depending on the LC/polymer concentration ratio LC dispersions can be categorized as polymer stabilized liquid crystals(PSLCs)[9] and polymer dispersed liquid crystals(PDLCs). In the PSLC system the LC loading is greater compared to PDLC systems. HPDLCs are specialized form of PDLCs.

PDLCs which are phase separated LC and polymer composites are described in detail in this section.

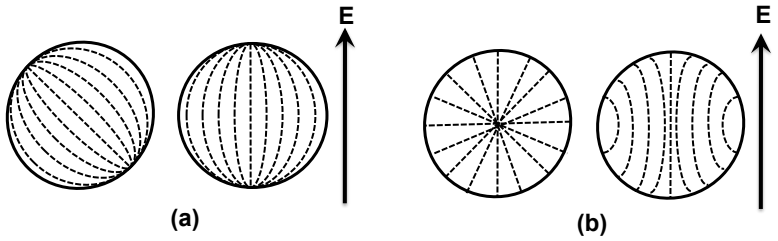

Figure 2.8: (a) Ideal bipolar or planar droplet (b) radial or homeotropic droplet

Polymer Dispersed Liquid Crystals

Confinement effects on LCs have been studied as early as the beginning of 20^{th} century. German physicist Otto Lehmann initially worked with Friedrich Reinitzer to understand the LC phase observed in cholesteric substance by Reinitzer. Lehmann continued to study the LC phase and studied the confinement effects of LCs. He analyzed the birefringence effects of suspended liquid crystal droplets in an isotropic medium using an optical polarizing microscope in 1904. He published his work titled Liquid Crystals that year[10]. Meyer proposed the bipolar droplet configuration in confined LC based on experimental observations 1969[11]. Dubois-Violette and Parodi theoretically determined stable configuration of LC in confined spherical droplet structures in 1969[12]. In 1981 Fergason filed a patent of using encapsulated LC in a suitable capsule medium and applying electric field across it for electro-optic applications[13]. Craighead et. al fabricated PDLCs by imbibing a porous membrane with LCs [14]. Phase separation method of PDLC fabrication was proposed by Doane et. al.[15].

PDLCs are two phased systems with aggregate of LC molecules forming droplets in cross linked polymer matrix binder. These LC droplets vary in size in the micrometer range and are characterized by an average director direction randomly oriented in the PDLC matrix. The PDLC film respond to interacting light by creating a controllable

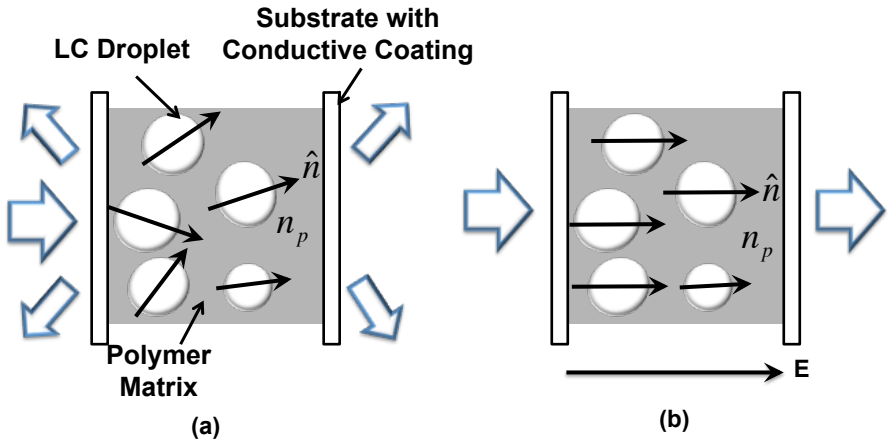

Figure 2.9: (a) The incident radiation interacting with PDLC is scattered by it and (b) the incident radiation interacting with PDLC is transmitted through it when the field **E** is applied across it

scattering effect and have been studied extensively since the early 1980.

PDLCs are fabricated by many techniques such as polymerization induced phase separation, phase separation induced by solvent evaporation from the polymer-LC mixture, thermally induced phase separation accompanied by cooling, soaking a pre-formed microporous structure with liquid crystals and emulsification process [8]. Polymerization induced phase separation(PIPS) by optical wavelength illumination is the technique extensively used in this work. Photopolymerization technique is detailed in Section 2.2. A blend of LC, low molecular weight monomer and photoinitiator is irradiated with light to induce polymerization resulting in phase separation. Acrylate and thiolene chemistry have been extensively used for PIPS.

Depending on the anchoring of the LC molecules along the LC droplet/polymer interface many different LC alignment in confined geometry are possible[8]. Schematic of two important types of droplet configuration and their reorientation to applied field are depicted here. The two types of LC droplet alignment are termed as bipolar and radial. If the LC molecules at the interface favor homogeneous anchoring(depicted in

Figure 2.6(b)), a stable configuration resulting from elastic free energy minimization causes a bipolar formation as shown Figure 2.8(a). The free energy is determined from Equation 2.2. Here the splay deformation is present at two opposite corners and bend deformation connects these ends. If the LC molecules prefer homeotropic anchoring(depicted in Figure 2.6(a)) then the energy minimization leads to a radial configuration predominantly showing splay deformation as shown in Figure 2.8(b). Electric field **E** applied across the droplets rearranges the LC molecules in the droplets as shown with anchoring effects at the interfaces. For the bipolar and radial configuration the droplets are realigned having bipolar and axial configuration respectively. Axial configuration can be found in LC droplets without the application of field for weak homeotropic anchoring at the LC/polymer interface. Figure 2.8 shows an ideal spherical shaped LC droplet. However the droplets are not perfectly spherical and the orientation of LC molecules tends to be more complex and have been rigorously studied using methods such as nuclear magnetic resonance studies[16].

A PDLC film system exhibiting its field controllable optical property is shown in Figure 2.9. Here the film is sandwiched between transparent substrate coated with a conductive coating. This coating allows application of field across it. Figure 2.9(a) shows a PDLC system with LC droplets randomly dispersed having average droplet director $\hat{\mathbf{n}}$ randomly oriented. The wavelength incident on PDLC film is scattered if the LC droplet size are comparable to the incident wavelength[17]. This renders the PDLC optically opaque. The scattering is mainly due to the mismatch between the LC droplet refractive index and the polymer refractive index and also the droplet size. If the droplets sizes are too small compared to the incident wavelengths then the scattering is weaker and the PDLCs are more transparent.

Application of electric field **E** across the film as depicted in Figure 2.9(b) aligns the liquid crystals long axis along the field. The ordinary refractive index n_o of the

LC and the polymer refractive index n_p are matched in this system. This results in a uniform refractive index in the PDLC medium and the incident light traverses through the system without scattering. Thus the PDLC transforms from a light scattering medium to an optically transparent medium upon application of field. This electro optical property is extensively studied and used in light filtering device applications.

By applying holography techniques to PDLCs the LCs droplets can be arranged in periodic layers resulting in a Bragg grating structure of alternating LC and polymer regions. The next section is a brief overview of holography techniques followed by an introduction to holographically fabricated PDLCs.

2.4 Holography

Holography interferometry technique creates a 3 dimensional representation of an object. During the holography recording process the interference pattern generated by two mutually coherent, reference wave and object wave pattern is stored in a recording medium called hologram. The interference pattern stores coded information on the amplitude and phase of the object pattern. To reconstruct the complete 3 dimensional information of the object pattern, the hologram is illuminated with the reference wave[18]. This method is different from conventional imaging techniques where 2 dimensional image of an object is stored, which contains only the spatial amplitude variation information.

The principle of holography was proposed in the late 1940's by Denis Gabor[19]. It resulted from his work on improving electron microscope imaging techniques. Gabor used a light source which had coherence length in the range of fraction of a millimeter and used inline holography technique, where scattered wave was used as one of the recording waves which resulted in weak holograms. With the advent of workable lasers in 1962 and pioneering work by Denisyuk[20], Leith and Upatneiks[21] the modern

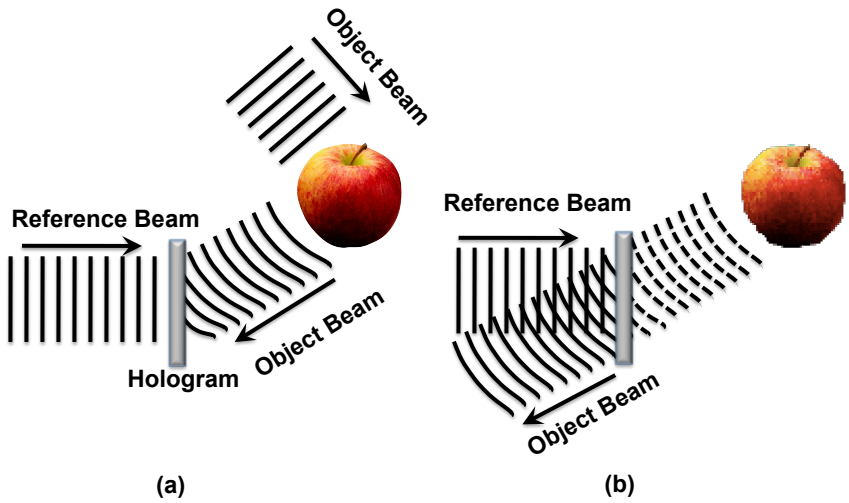

Figure 2.10: (a) Recording process of a simple reflection hologram is depicted where the reference and the object beam record an interference pattern in a photosensitive film(b) Reconstruction process is shown where the object is replayed by shining the hologram with the reference beam

methods of holography began and has found wide spread applications in areas such as telecommunications, data storage and nano fabrication.

Figure 2.10 shows a typical reflection hologram recording and reconstruction. During the holography recording process shown in Figure 2.10(a) an object beam containing the information to be recorded and an reference beam are made to interfere in a recording media. Depending on the depth of the photosensitive media a surface or volume hologram is created. For replaying the captured object information in the hologram it is shone with the reference beam as shown in Figure 2.10(b). A virtual image of the object is created at the location where the object was originally placed.

The recording medium can be a two dimensional surface or three dimensional volume. Hence in a volume hologram the photosensitive recording film is relatively thick. The transmission and reflection volume hologram creation and replaying is shown in Figure 2.11. For recording the transmission hologram the reference and

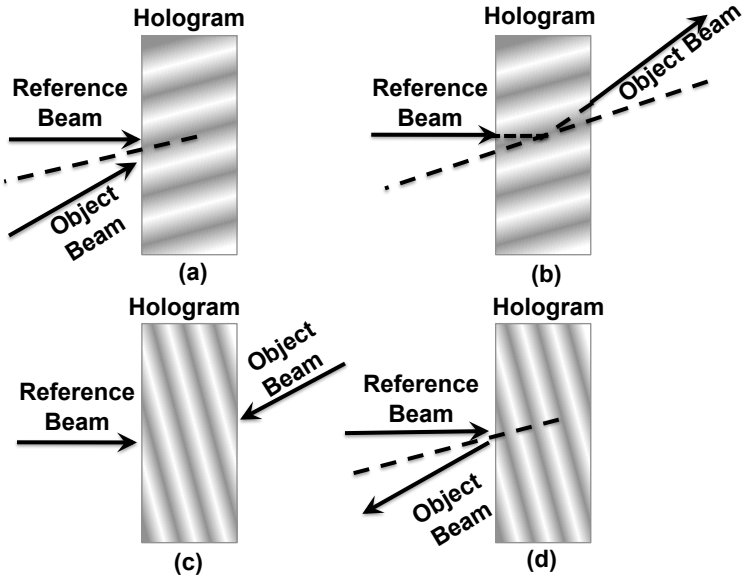

Figure 2.11: Transmission and reflection volume hologram configuration are shown here. (a) depicts the creation of the transmission hologram and (b) shows the replaying of the recorded object beam. (c) Reflection volume hologram formation is shown here and (d) depicts its reconstruction

object wave are incident on the same side of the recording medium and illuminating the recorded hologram with the reference wave reconstructs the object. This is shown in Figure 2.11(a) and (b) respectively. In the reflection type hologram the interfering waves are incident on the recording medium from two different sides as indicated in Figure 2.11(c). Figure 2.11(d) shows the replaying of the object wave by shining the hologram with the reference wave. In this dissertation reflection mode volume hologram is considered.

Consider a reflection recording configuration with the recording media's depth along the z axis as shown in Figure 2.12(a). Here the reference and object wave electric field vectors incident on the photosensitive medium are traveling with a wavelength λ, creating an angle θ with the x axis. The parameters representing the reference wave have the subscript 1 and those representing the object wave have subscript 2.

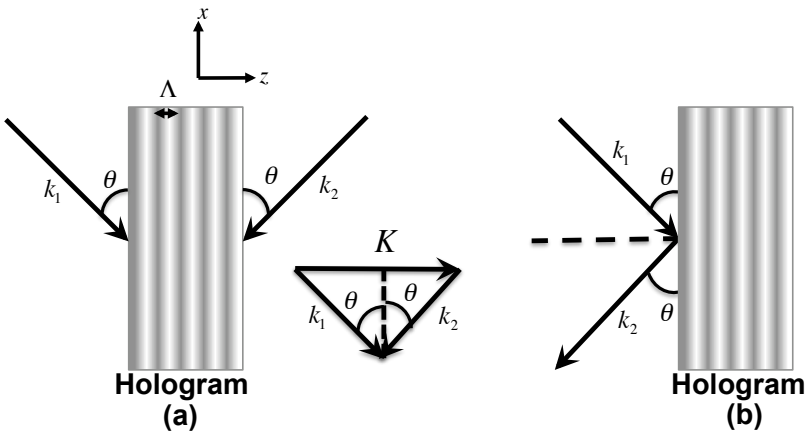

Figure 2.12: Holography configuration showing (a) recording and (b) reconstruction

The electric field vectors can be represented by monochromatic plane wave equations

$$\mathbf{E_1} = \mathbf{E_{01}} exp\left[i\left(\omega t - \mathbf{k_1}\cdot\mathbf{r}\right)\right] \quad \text{and} \quad \mathbf{E_2} = \mathbf{E_{02}} exp\left[i\left(\omega t - \mathbf{k_2}\cdot\mathbf{r}\right)\right], \tag{2.9}$$

where $\mathbf{k_1}$ and $\mathbf{k_2}$ are propagation vectors in the xz plane, $\mathbf{E_{01}}$ and $\mathbf{E_{02}}$ are the field amplitude vectors and $\mathbf{r}$ is the displacement vector from the origin.

The intensity or irradiance I which is a measure of the energy per unit area per unit time recorded at the hologram is proportional to the square of the amplitude of the electric field. Hence the intensity recorded by the interference pattern of the reference and object wave is

$$I \propto |E_{01}^2 + E_{02}^2|$$

The intensity of the interference pattern can be represented by[22]

$$I = I_1 + I_2 + 2\sqrt{I_1 I_2} cos(\mathbf{k_1}.\mathbf{r} - \mathbf{k_2}.\mathbf{r}) \tag{2.10}$$

$$I = I_1 + I_2 + 2\sqrt{I_1 I_2} cos(\mathbf{K}.\mathbf{r}), \tag{2.11}$$

where $\mathbf{K}$ termed as the grating vector lies parallel to the z axis and $\mathbf{K} = \mathbf{k_1} - \mathbf{k_2}$. The

intensity is a sinusoidally varying pattern with a periodicity denoted by $\Lambda = 2\pi/|\mathbf{K}|$. The magnitude of the propagation vectors in the hologram medium are $|\mathbf{k_1}| = |\mathbf{k_2}| = 2\pi n/\lambda$, where n is the average refractive index of the hologram. This equation can be rewritten as

$$I = I_0[1 + V cos(\mathbf{K}.\mathbf{r})], \tag{2.12}$$

where $I_0 = I_1 + I_2$ and $V = 2\sqrt{I_1 I_2}/(I_1 + I_2)$ is known as the fringe constant. From the vector diagram of Figure 2.12 the angle between the reference and the object wave is 2θ and $|\mathbf{K}| = 2(2\pi n/\lambda)\sin\theta$. This can be rewritten to determine the periodicity Λ also termed pathlength as

$$\Lambda = \frac{\lambda}{2n\sin\theta} \tag{2.13}$$

This is known as the Bragg equation.

Illuminating the recorded volume hologram with the reference wave of wavelength λ as illustrated in Figure 2.12(b) at an angle θ replays the reflection wave since the Bragg condition above is met. However if the Bragg condition is not met due to variation in the reference wavelength or the angle of incidence w.r.t x axis then the object wave is not replayed. Therefore if a broad range of white light is incident on the hologram only the wavelength that matches the Bragg equation is selectively replayed by being reflected as in the case of reflection HPDLCs.

Some of the techniques used to create hologram include material set such as silver halide emulsions, dichromated gelatin, photoresists, photothermoplastic materials, organic dyes and photopolymers [18]. Photopolymer material set is used in this dissertation. Here a homogeneous blend of LC, oligomer and photoinitiator system is exposed to a recording laser and post cured by exposing to UV light. The hologram is formed by a change in the material refractive index and is developed real time. An

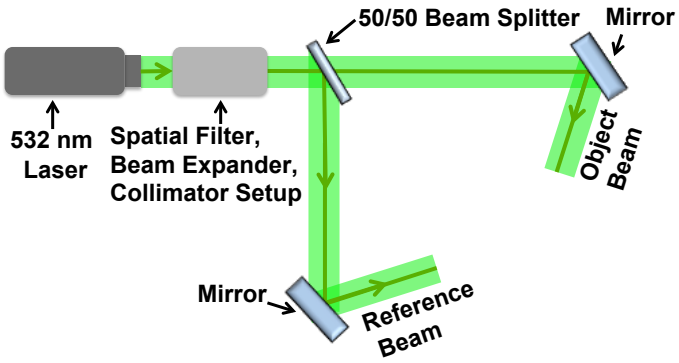

Figure 2.13: Basic holographic setup

ideal photopolymer considered should be photosensitive to all visible wavelengths of light, flexible and transparent.

A simple holographic setup shown in Figure 2.13 summarises the holographic setup used in this dissertation work. A 532nm Verdi 5W laser is used as the coherent source. The laser output has a beam diameter of 2.5mm$\pm$10%. This is passed through a spatial filter fitted with a pinhole and a magnifying objective. This render the the Gaussian wavefront emanating from the laser more flatter and beam expands the laser. The diverging beam is then collimated with a convex lens. The 50/50 beam splitter splits the laser beam into two equal intensity beams to create the reference beam and the object beam. With the aid of mirrors the two beams are made to interfere in the desired configuration. The most frequently used configurations such as the single beam method in the dissertation are discussed in detail in Section 3.2.1.

In the next section we apply the holography technique to photopolymers.

2.5 Holographic Polymer Dispersed Liquid Crystals

Holographically formed polymer dispersed liquid crystals(HPDLCs) are fabricated by applying holography principles to PDLCs. The two important differences in

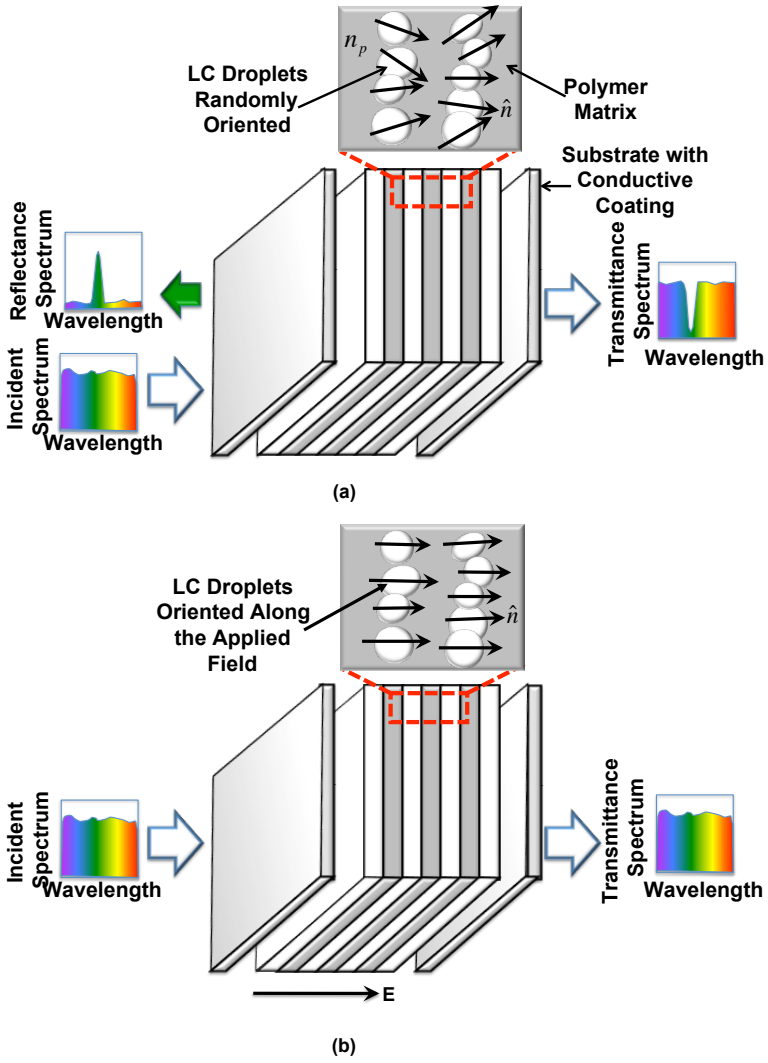

Figure 2.14: Schematic showing the optical responses of a reflection mode HPDLC to the visible wavelength spectrum (a) when no electric field is applied across it and (b) when an electric field is applied across it.

HPDLCs compared to PDLCs are their periodic structure and smaller LC droplet sizes.

Margerum et.al at Hughes Research Labs pioneered the work of creating periodicity in the PDLC medium paving the way for the creation of transmission HPDLCs in 1988[23]. They made periodically varying UV source incident on the prepolymer-LC mixture to create a grating structure. They also suggested the use of counter propagating laser beams to create periodic structure. Ingwall et. al. at Polaroid created a device by filling a cured holographic Polaroid DMP film with liquid crystals and demonstrated its electro-optic property by applying a field across it[24]. Sutherland et. al fabricated transmission gratings by applying holography technique to photoinitiator assisted PIPS process in 1993[25]. This holography fabrication technique is used throughout in this dissertation and the recipe for fabrication is detail in Section 3.1.2. The first reflection holograms using polymers and LCs were proposed by Tanaka et. al. in 1993[26]. Since then HPDLCs have been studied in various configurations extensively for multitude of applications.

HPDLCs are desired for multiple applications because of their one step fabrication,low form factor, high color purity and fast switching characteristics in the microsecond range. Depending on the fabrication setup, reflection or transmission holograms are fabricated as shown in Section 3.2.1. Reflection holograms are considered extensively in this dissertation. They are optical bandstop filters that selectively reflect wavelengths based on their Bragg grating structure of alternating polymer layers and nanometer sized LC droplet layers. They are reconfigurable and reflect or transmit incident wavelengths based on applied electric field. Applying an electric field results in an optically transparent state, allowing all incident wavelengths to be transmitted. The field response of HPDLCs is described more in detail in Section 3.2.2.

The operation of a reflection type HPDLC is shown in Figure 2.14. The HPDLC film is sandwiched between conductive coated substrates. Glass is commonly used as a substrate, coated with conductive indium tin oxide (ITO). The average orientation direction of the LC droplets represented by the unit vector $\hat{n}$ is random at zero field bias. A refractive index mismatch exists between the randomly oriented LCs and the polymer refractive index n_p as shown in Figure 2.14(a). The periodically varying refractive index due to the alternating LC and polymer regions creates a Bragg grating structure, which reflects a specific wavelength of light. This is represented by the reflectance of green wavelengths and the transmission of remnant incident wavelengths from the HPDLC hologram, as shown in Figure 2.14(a).

Applying an electric field across the HPDLC via the conductive coating reorientates the LCs along the direction of the field (Figure 2.14(b)). The LC is chosen such that the RI of the reoriented LC n_o is the same as the RI n_p of the polymer. Thus a uniform RI in the HPDLC due to RI match between the polymer and LC layers erases the Bragg grating. Thus the entire incident wavelength spectrum is transmitted without wavelength selectivity, as shown in Figure 2.14(b).

The key ingredients for grating formation are monomers, LC and initiator to sensitize this prepolymer syrup to the particular laser wavelength used in the setup and initiate the formation process. Section 3.1.2 gives an overview of the two recipes used in this dissertation. The prepolymer cell is then exposed to two counter propagating laser beams in the reflection hologram setup, which results in a standing wave pattern of the laser intensity in the prepolymer cell. The monomers polymerize in the bright region of this wave intensity, while the LCs diffuse to the dark regions, forming LC droplets. The grating formed is post cured with a UV blanket for 10mins to react any unreacted monomers in the HPDLC formed.

The grating pitch Λ, which is the width of one adjacent polymer and LC layer, is

determined by the Bragg grating equation of Equation 2.13 where λ is the laser wavelength of the holography setup and n is the average refractive index of the LC/polymer layers.

The Equation 2.13 can be rewritten to represented the reflected wavelength λ_R peak for normal source incidence as

$$\lambda_R = 2n\Lambda$$

Here n is the average refractive index of the HPDLC system.

Considering the refractive index varying sinusoidally the HPDLCs can be modeled accurately. This modulation is represented by[27]

$$n = n_0 + n_1 \cos\left(\frac{2\pi}{\Lambda} z\right) \tag{2.14}$$

where n_0, n_1 are constants, Λ grating pitch which is the measure of periodicity and z is an indicator of position in the 3 dimensional cartesian coordinate system. n_0 is the refractive index without any modulation in the medium. n_1 is the spatially modulated refractive index . Here the crest of the sinusoid corresponds to the center of the LC layer and the trough corresponds to the center of the polymer layer.

The average refractive n_0 can be expressed the weighted sum of the average LC and polymer refractive index represented as

$$n_0 = \phi_{LC} n_{LC} + (1 - \phi_{LC}) n_p$$

where ϕ_{LC} is the the volume fractions of LC in the prepolymer recipe and has a value in the range of 1.5. The refractive index mismatch of the grating is

$$\triangle_G = n_{LC} - n_{pl}$$

where n_{LC} and n_{pl} are the refractive index of the LC and polymer layer. The average refractive index of the LC layer can be represented by the weighted average equation of

$$n_{LC} = \sqrt{\frac{2n_o^2 + n_e^2}{3}}$$

n_{pl} is the refractive index of the polymer layer which also consists of LCs that have not undergone phase separation to the LC layers. Let the parameter α define the volume fraction of LC in the polymer layer. Thus

$$n_{pl} = \alpha n_p + (1 - \alpha) n_{LC}.$$

From this it can be determined that the droplet layer width is $\Lambda\alpha\phi_{LC}$. Thus the sinusoidal profile determining n_1 is

$$n_1 = \frac{2\triangle_G}{\pi} \sin(\pi\alpha\phi_{LC})$$

with values in the range of $10^{-3} - 10^{-1}$

The reflected Bragg peak wavelength, is determined from the grating pitch. Hence it is directly proportional to the grating pitch. This shows that the angle of incidence of the counter propagating beams is an important consideration in deciding the reflected wavelength of the HPDLC. To create broadband reflecting gratings, this parameter variation will play a key role.

Typically HPDLCs have a narrow peak reflection wavelength with a full width at half maximum (FWHM) of 5 to 20nm and the reflected peak corresponds to the Bragg reflecting wavelength. A typical spectrum of the reflection and transmission intensities of a HPDLC is shown in Figure 2.15(a) and Figure 2.15(b) with the FWHM indicated measured at half of maximum reflection intensity or maximum transmission intensity, respectively.

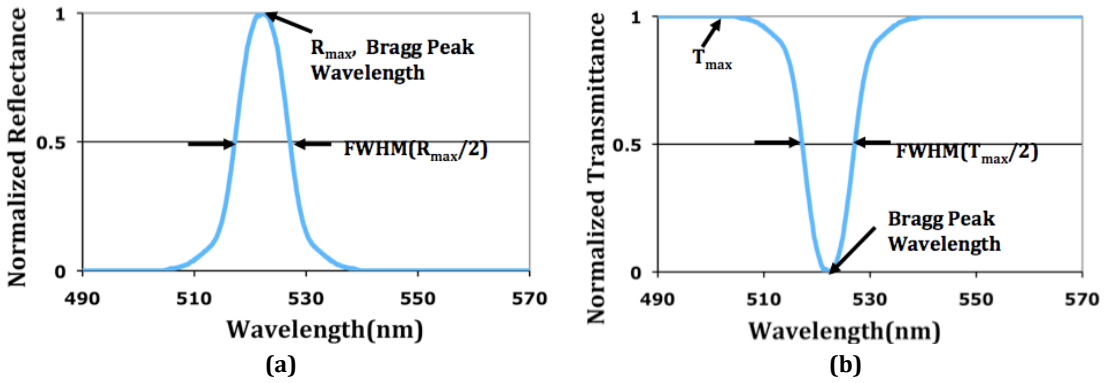

Figure 2.15: (a)Normalized reflectance response and (b)Normalized transmittance response of HPDLCs

The next section briefs some of the characterization techniques to understand the HPDLC morphology.

2.6 Characterization Techniques

Parameters such as the thickness of the HPDLC thin film, morphology features, interfacial roughness between the polymer and LC layers, LC orientation in the droplets are important considerations for the electrical and optical performance of the thin films. Hence we use multiple characterization techniques for thin film HPDLC analysis. Microscopy, spectroscopy, wavefront sensing and interferometry are some of the important analysis tools used here. Scanning electron microscopy, electron spin resonance spectroscopy, wavefront sensing and scattering analysis techniques are briefly reviewed here for HPDLC analysis.

2.6.1 Scanning electron microscopy technique

Microscopy techniques have been used since the advent of PDLCs to understand their fascinating morphology[8]. Scanning electron microscopy(SEM) has proven to

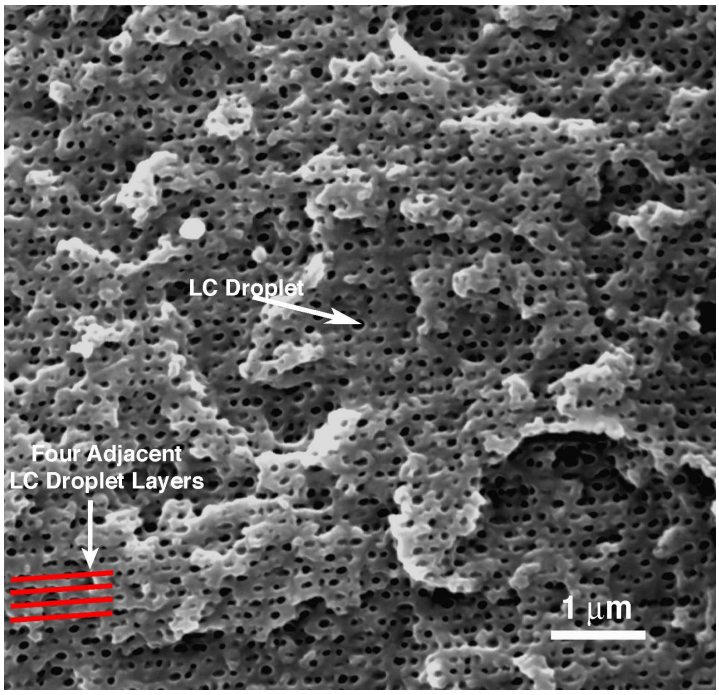

Figure 2.16: SEM image of the HPDLC made of acrylate recipe with di and tri functional oligomers

be very useful to study the nanometer scale morphology of HPDLCs. It is extensively used for the visual inspection of phase separation between LCs and polymer, the LC droplet diameter, droplet structure, grating pitch, droplet dispersion, droplet density determination etc.,

In an SEM a finely focused electron beam is irradiated on a sample surface in a raster fashion to create a micrograph [28]. Electron types generated after the interaction of the sample with the electron beam include secondary electrons(SE) and backscatter electrons(BSE) and the respective detectors to quantify them are called SE detectors and BSE detectors. The images formed by detecting these electrons will be analyzed in this dissertation.

The conventional high vacuum SEM(HV-SEM) technique requires the test sample be placed in a near vacuum chamber to prevent attenuation of the electron beam and

damage to the instrument electronics. The sample preparation for HPDLC involves freezing its surface to preserve the grating structure and fracturing the appropriate section for imaging. The LC is usually removed from the sample by soaking it with a solvent for 20 minutes. The film is then heated at about 40^0C to remove any remnant solvents and then placed on aluminum stubs to enable cross section imaging of HPDLCs. The film is held together by one-sided adhesive copper tape and fastened to the stub using silver paint. A thin conductive coating is applied on the sample surface typically by sputter coating to render it electrically conductive and prevent electric charge buildup. Thus a conductive path for electron charge flow is ensured by sputter coating the sample, using copper tape, silver paint and aluminum stubs to fasten it. The conductive coating should be of the right thickness to enable accurate imaging of the surface having good contrast without obscuring finer details of the morphology. It is important to ascertain that the polymer matrix has a rigid texture and cannot be easily distorted during imaging resulting in artifacts.

Figure 2.16 is an SEM image of the cross section of the HPDLC sample made with acrylate formulation imaged using HV-SEM. The dark voids are the LC droplets as indicated. Four lines are drawn on drawn at the center of 4 adjacent LC layers to indicate the layered structure surrounded by the polymer matrix. The distance between these lines indicate the grating pitch which is the thickness of one layer of LC and polymer or the distance between the centers of two adjacent LC layers.

The LC droplet removal during sample preparation is disadvantageous since it results in variation of grating profile. Air now fills the LC droplets voids resulting in the possible reduction in the grating pitch. Variable pressure SEM(VPSEM) and environmental SEM (ESEM) are two new techniques used here for the first time for morphology study of HPDLCs at high resolution without the need for LC removal or conductive coating. Here the samples are imaged in a gaseous environment which

permits the imaging of non conductive samples without any special coating on them. The specimen preparation involves freeze fracturing the sample followed by direct imaging in the SEM chamber.

In this work the HPDLC grating structure is imaged in conventional HV-SEM and VPSEM and the grating structure is compared. The potential of the ESEM technique for imaging the HPDLC structure is explored.

The orientation of the LCs inside the droplets is complex and the study of these confinement effect with the aid of spin resonance technique is described in detail in the next section.

2.6.2 Electron Spin Resonance Spectroscopy Technique

LC droplets confined in small geometries, embedded in polymer matrix have interesting optical properties. Confinement effects at the polymer/LC interface reorient the LC molecule to minimize their elastic free energy expressed in Equation 2.2. Many configuration of LC droplets can be present and are not completely understood. Electron spin resonance spectroscopy(ESR) aids in determining the orientational order inside the droplets using the spin labeling technique[29]. This sections aims to give a brief overview of the ESR technique to interpret the molecular order and dynamics of LCs.

In the ESR spin labeling technique the LC is doped with paramagnetic spin probes having unpaired electrons and the spectrum absorbed by the unpaired electrons is measured. Spectral features such as the line shapes and resonant frequency are analyzed using rigorous theoretical techniques to determine the environment conditions of the spin probe. Hence the spin probe is carefully chosen to match the surrounding LC molecules and its dynamics to reflect them.

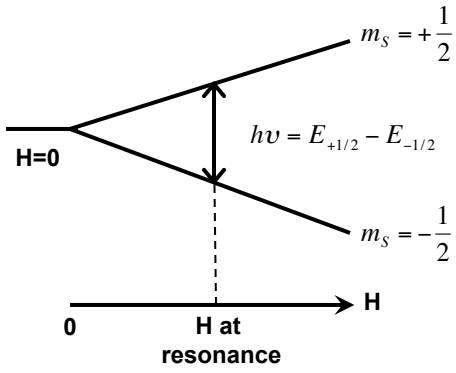

Figure 2.17: Illustration of resonance condition in ESR spectroscopy. Here a fixed field of energy $h\nu$ is applied on a system with unpaired electrons. In the presence increasing magnetic field **H** the energy level of the unpaired electron splits due to Zeeman effect having energy $E_{+1/2}$ and $E_{-1/2}$. Resonance condition occurs when the energy difference between the two split levels is equal to the fixed applied energy

Zeeman Effect

ESR technique is based on Zeeman effect, which is the splitting of the electron energy levels due to the spin or intrinsic angular momentum of an electron in the presence of strong magnetic field. For spin probes with unpaired electrons the spin angular momentum $S = 1/2$ and can have two energy level with spin quantum numbers $m_S = 1/2$ and $m_S = -1/2$. In the presence of a strong magnetic field the orbital of the unpaired electrons split into two energy levels and the energy at each of the levels with $m_S = \pm 1/2$, is proportional to the applied magnetic field determined as[29]

$$E_{+1/2} = +\frac{1}{2} g\beta_e \mathbf{H} \qquad E_{-1/2} = -\frac{1}{2} g\beta_e \mathbf{H} \tag{2.15}$$

where g is the spectroscopic fission factor constant, β_e is the Bohr Magneton constant and **H** is the strength of the magnetic field. The difference in the energy between the two levels is

$$\Delta E = E_{+1/2} - E_{-1/2} = g\beta_e \mathbf{H} \tag{2.16}$$

Applying an electromagnetic field of frequency ν with energy equal to the energy difference between the split orbitals, causes the unpaired electron to absorb it and transition from one orbital to the other. This is mathematically represented as

$$h\nu = \Delta E = g\beta\mathbf{H} \tag{2.17}$$

Thus, when the energy difference between the split orbital energy levels caused by a strong magnetic field corresponds to an incident electromagnetic radiation energy, resonance takes place and the electron absorbs the energy and transitions from one energy level to another. Typically in ESR experiments the electromagnetic field frequency ν is fixed and the magnetic field is varied using electromagnets. The resonance condition in ESR technique is illustrated in Figure 2.17.

Relaxation Mechanism

Typically in a spin probe, both the spin states are nearly equally populated with electrons with a very small difference which is used to measure the ESR spectrum.Two types of relaxation are responsible to maintain the population difference and equilibrium state and aid in interpretation of the linewidth of the absorption peak. The mechanisms are the spin lattice relaxation and transverse time relaxation.

In spin lattice relaxation the system is restored to equilibrium by heat energy transfer to the surrounding medium which is characterized by time T_1. This is a non radiative process of transition from higher energy to lower energy state.

A tilt in the magnetic moment of the electrons makes them have a precessional motion. This create a variation in their magnetic parameters.The time taken for this process is called the transverse relaxation time T_2. These relaxation parameter determine the absorption spectrum which corresponds to a Lorentzian line shape function. However typically the first derivative of the absorption spectrum is shown

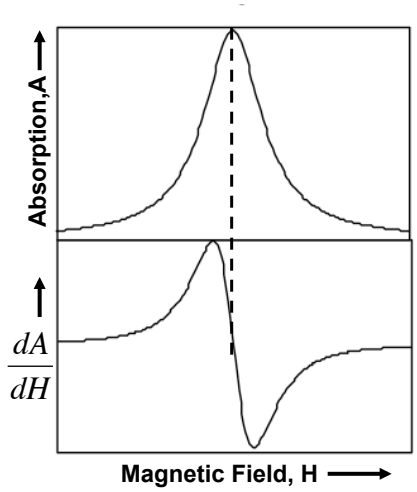

Figure 2.18: ESR absorption spectrum A and its first derivative dA/dB as a function of magnetic field strength H

in the ESR spectrometer. Figure 2.18 shows the absorption spectrum and its first derivation as a function of the magnetic field strength H.

Hyperfine Coupling

A single absorption peak in shown in Figure 2.18. This is not always the case. Interaction between the electron spin momentum S and the nuclear spin momentum I cause more than one peak in the ESR spectrum. This cause further splitting of the Zeeman levels creating the hyperfine structure discussed in the next section.

Nitroxide Spin Probe

The BL038 LC extensively used in this dissertation is doped here with a stable nitroxide spin probe 3β-DOXYL-5α-Cholestane(CSL) free radical purchased from Aldrich for ESR analysis. This radical has rigidity, shape and size similar to 5CB, a chief ingredient of BL038 LC. CSL has been previously used extensively for study of 5CB LC [30, 31, 32]

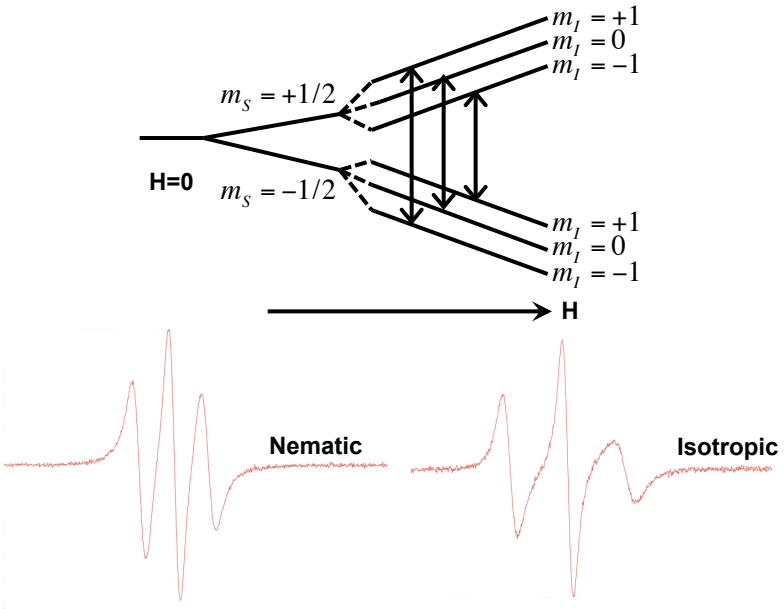

Figure 2.19: Illustration of the unpaired electron orbital in a CSL spin probe during resonance condition indicating the hyperfine structure and three distinct energy transitions and ESR spectra plot at nematic and isotropic temperature ranges of 5CB LC doped with CSL

In the CSL spin probe the unpaired electron orbital splits into two orbitals represented as $m_s = +1/2$ and $m_s = -1/2$ in the presence of magnetic field due to Zeeman effect . Each of the orbitals are further subdivided into 3 more levels due to the interaction between the electron spin and nuclear spin momentum creating hyperfine structure represented by $m_I = +1$, $m_I = 0$ and $m_I = -1$. Hence in the presence of a fixed electromagnetic radiation of frequency ν, varying magnetic field induces there different electron absorption transition during resonance condition for CSL in 5CB. Figure 2.19 shows the resonance condition and two ESR spectra of 5CB LC doped with CSL probe when they are in the nematic and isotropic state. The three peaks are due to the three transition indicated in the figure due to hyperfine structure formation.

Figure 2.20 is the chemical structure of CSL. The structure has a chosen ordering

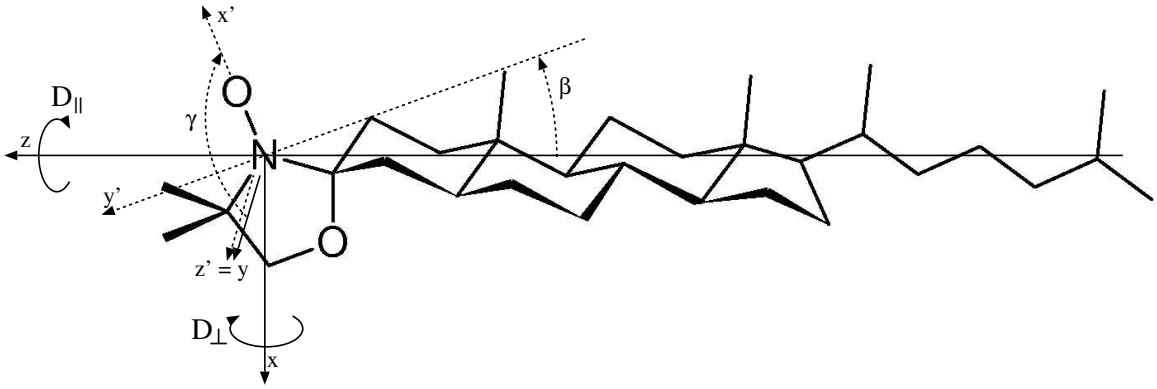

Figure 2.20: Chemical Structure of the CSL spin probe together with the chosen ordering orientation of xyz and magnetic molecular frames x'y'z', the Euler angles β and γ, between the molecular frames and the principal components. $D_\perp$(reorientation of the molecular long axis) and $D_\parallel$(rotation around the molecular long axis), of the rotational diffusion tensor

$(x, y, z,$ solid line) and magnetic $(x', y', z',$ dashed line) molecular frames and the indication of its two main reorientational motions, tumbling and spinning, with the corresponding components of the rotational diffusion tensor: $D_\perp$(reorientation of the molecular long axis) and $D_\parallel$(rotation around the long axis), respectively.

The molecular magnetic frame (x', y', z') was chosen according to the standard system of coordinates for the N-O paramagnetic moiety with the x' axis along the N-O bond[30] and the z' axis perpendicular to the five-membered ring, i.e. parallel to the pz orbital containing the unpaired electron density. According to a standard approach, the z axis of the ordering frame is considered parallel to the principal axis of inertia of the probe (its long axis) and, to simplify the rotation which takes the ordering into the magnetic frame,[30] the y axis is considered parallel to the z' axis. To reduce the correlation among variable parameters, the Euler angles, β and γ, between the molecular frames, were fixed in the fits to 15° and 90°, respectively, in agreement with previous results obtained in related systems.[30, 31, 32]

Theory

The complex theoretical simulation of the ESR spectra was done using the slow tumbling theory[29] devised by Jack Freed and collaborators.

HPDLC is a complex system with different types of LC orientations which form the ESR spectra. This is due to the surface and local curvature of the nanodroplets and multiple local domains with different order and fluidity as suggested by the previous DNMR studies[33]. Here a weighted sum of different spectral contribution namely monodomain model(N), three dimensional partially ordered polydomain (3DPOP), bidimensional polydomain (2D), isotropic (ISO) and rigid-limit (RL) are performed to get the best theoretical fit for the experimental spectra. The resultant spectra explains the different surroundings encountered by the spin probe which helps to judge the environment prevailing in the confined LCs.

Thus the experimental ESR spectrum of the HPDLC samples, $I(\omega - \omega_0)$, was modeled as the weighted sum of several spectral contributions, I_i, corresponding to different conditions where the CSL spin probe is supposed to be located.

$$I(\omega - \omega_0) = \sum_i I_i(\omega - \omega_0)\, f_i\,, \tag{2.18}$$

where f_i is the fractional contribution of the i-th environment.

Nematic Monodomain Model(N) In the monodomain model all the local domain directors existing in the LC droplet are oriented in the same direction. The unsaturated, high-field ESR monodomain spectrum $I_m(\omega - \omega_0, \beta_d)$ at frequency ω and at an angle β_d between the director and the magnetic field is calculated using the standard Stochastic Liouville Equation (SLE) approach of Freed and collaborators

[29, 34, 35] which predicts that:

$$I_m(\omega-\omega_0;\beta_d)=\frac{1}{\pi}\langle\langle v|\left[(\hat{\mathbf{\Gamma}}-i\mathcal{L})+i(\omega-\omega_0)\mathbf{I}\right]^{-1}|v\rangle\rangle\,, \tag{2.19}$$

where $\omega_0 = g_0\beta_e B_0/\hbar$, $\mathcal{L}$ is the Liouville superoperator obtained from the orientation dependent spin Hamiltonian, $\hat{\mathbf{\Gamma}}$ is the diffusion superoperator describing the reorientational motion of the probe, $|v\rangle$ is a vector containing spin transition moments averaged over the equilibrium ensemble and $\mathbf{I}$ is the identity.

The local order is described by the complex orientational order parameter $\langle P_2\rangle$ defined as

$$\langle P_2\rangle \equiv \langle D^2_{0,0}\rangle = \frac{\int D^2_{0,0}(\beta)\,\exp[-U(\beta)/kT]\,\sin\beta\;d\beta}{\int \exp[-U(\beta)/kT]\,\sin\beta\;d\beta}\,, \tag{2.20}$$

where β is the probe orientation with respect to the domain director, $U(\beta)$ is the reorientational motion of the probe, $D^L_{M,K}$ are the orientational Wigner rotation matrices with L, M, K integer; $L \geq 0$; $|M|$ and $|K| \leq L$, forming the basis set for the orientations.

Three Dimensional Partially Ordered Polydomain(3DPOP) In the 3DPOP environment the spin probe is assumed to reorient in a distribution of ordered domains with local director orientation β_d with respect to the magnetic field. The corresponding ESR spectrum, $I_{3DPOP}(\omega-\omega_0)$, is given by the superposition of the monodomain spectra [36, 37]:

$$I_{3DPOP}(\omega-\omega_0)=\int_0^{\pi} I(\omega-\omega_0;\beta_d)\,P(\beta_d)\,\sin\beta_d\;d\beta_d\,. \tag{2.21}$$

where, to further limit the number of model parameters, the unknown distribution of the domain directors, $P(\beta_d)$, has been modeled, as it is usually done (e.g. in the EPRLL "family" of ESR spectra simulation programs [38]), by a uniaxial, $\langle P_2\rangle$-type

distribution $P(\beta_d) \propto \exp[\lambda_d P_2(\cos\beta_d)]$ where P_2 is a second rank Legendre polynomial and λ_d is a positive constant. The order of the domain directors is described by the orientational order parameter $\langle P_2\rangle_d$ defined as

$$\langle P_2\rangle_d = \frac{\int P_2(\cos\beta_d)\ \exp[\lambda_d P_2(\cos\beta_d)]\ \sin\beta_d\ d\beta_d}{\int \exp[\lambda_d P_2(\cos\beta_d)]\ \sin\beta_d\ d\beta_d}\,. \tag{2.22}$$

A value of $\langle P_2\rangle_d = 0$ represents the limiting case of a spherical distribution of the domain directors, $P(\beta_d) = 1/\pi$, whereas for $\langle P_2\rangle_d = 1$ the system is a monodomain aligned parallel to the magnetic field where $P(\beta_d) = \delta(\beta_d)$.

Bidimensional Polydomain(2D) The 2D environment is modeled as the 3DPOP one by changing the spherical distribution to cylindrical

$$I_{2D}(\omega - \omega_0) = \frac{1}{\pi}\int_0^{\pi} I(\omega - \omega_0; \beta_d)\ d\beta_d\,. \tag{2.23}$$

Isotropic(ISO) The ISO contribution is calculated by setting at zero the strength of the ordering potential, λ_{20}.

Rigid Limit(RL) A simple approach is adopted for the RL component which is modeled as a powder spectrum where reorientational relaxation effects are neglected (see e.g. [36] and refs. therein).

Thus the orientational order of the HPDLCs were determined by applying the slow tumbling theory to obtain the best fit for the ESR spectra. The next section is a brief review to understand the quality of the HPDLC wavefronts.

2.6.3 Wavefront Analysis

Wavefront sensing technique is used to determine the quality of the wavefront transmitted through the HPDLC. For example wavefront analyzer from AOA, Inc

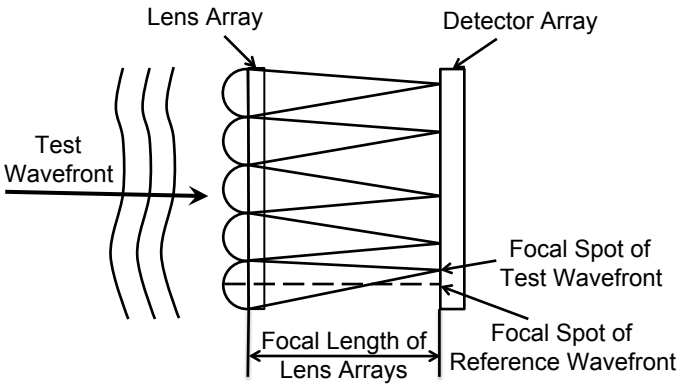

Figure 2.21: Measurement setup of Shack Hartmann wavefront sensor. The test wavefront is made incident on a lens array. Arrayed detector placed at the focal length of each of the lens measure the resultant focal spot positions.

based on Shack Hartmann wavefront analysis[39] compares deviation of a test wavefront transmitted through the HPDLC to an ideal reference wavefront. Software analysis of the two wavefront enables accurate computing of the aberrations in the test wavefront. A flat wavefront traversing through an HPDLC structure encounters interfacial roughness between the LC rich and the polymer rich layers. Also within the LC rich layer index inhomogeneities exists due to variation in droplet size and distribution[40]. Thus the wavefront transmitted through the HPDLC structure gather an RMS variation profile in terms of phase variations from each of the interfaces. These wavefront surface phase variations carry information regarding the interfacial morphology of the HPDLC. Looking at the final RMS wavefront aberration values and the Strehl ratios [41] indicated by the wavefront analyzer a general prediction of the HPDLC morphology can be made. Low RMS variations and higher Strehl ratios are indicative of smoother interfacial roughness for an HPDLC.

The setup inside the wavefront representing the measuring of test wavefront focal spot is illustrated in Figure 2.21.

2.6.4 Scattering Analysis

In reflection type HPDLCs the coherent scattering from the periodic structure of LC rich and polymer rich layers contribute to the Bragg reflected wavelength. However weak incoherent scattering also exists due to the polydispersity in the LC droplet size, shape, density, orientation and refractive index.

There are two principle types of scattering depending on the size of the LC droplets. When the LC droplets are of a size of up to tenth of the wavelength of interacting light the scattering is mainly Rayleigh scattering. When the droplet sizes are of the order of the wavelength of light Mie scattering takes place. Both these types of scattering for nematic droplets have been extensively studied by Zumer et. al. using Rayleigh-Gans approximation(RG) approximation[42] and anomalous diffraction approximation[43] for nematic droplets. In the reflection type HPDLC systems typically the LC droplet sizes range from about 50nm-150nm which predominantly contribute to Rayleigh scattering of visible light.

The phase shift $\triangle$ of incident radiation transmitting through a scattering LC droplet compared to that of light passing through the surrounding non scattering polymer can be used to develop the scattering models. Here each unit of the scattering medium reradiates the incident radiation. Thus the scattering medium changes the phase of the incident plane wave spatially[44]. Interference of the spatially phase varying light in far field results in the change in direction, angle and polarization of the transmitted radiation. A complete model to interpret scattering is extremely challenging. This is because the parameters that effect scattering such as polydispersity in shape, LC orientation inside the droplets, irregularity of the droplet shape along with droplet interconnectivity are variable. RG approximation assumes that

the maximum phase shift induced by the nematic droplets is $<< 1$, i.e. [8]

$$\triangle = 2kR \left| \frac{n_{LC}}{n_p} - 1 \right| << 1$$

where $k = 2\pi/\lambda$, R is the radius of the scattering object and n_{LC} and n_p are droplet and polymer refractive index.

The scattering cross section σ of the droplets by RG approximation is determined as [17]

$$\sigma = \sigma_0 \left(kR\right)^4 f$$

where σ_0 is the geometric scattering cross section and f is a function of the incident angle, scattering angle, polarization, refractive index of the LC droplet and polymer matrix.

The scattering cross section σ and the scattering intensity I_s have a dependence on the factor $(kR)^4$. Rayleigh scattering intensity $I_s \propto 1/\lambda^4$ results in the visible light to have higher scattering near the 400nm range compared to the 700nm range as observed in the interaction of HPDLC with visible wavelength.

In review this chapter is a brief overview of the raw materials of HPDLCs and holography technique basics for their fabrication. A few important characterization techniques are examined here. This chapter lays the ground work to understand the different techniques required for broadband HPDLC gratings. The next chapter delves into the recipes used in this dissertation for HPDLC fabrication, different fabrication setups and some of the widely used characterization techniques used for analysis.

3. Materials and Experimental Methods

This chapter details the HPDLC recipe used, its fabrication and experimental techniques to characterize HPDLCs.

3.1 Materials

The LC and the two optimized acrylate and thiolene monomer based HPDLC recipes used in this dissertation are detailed in this section.

3.1.1 Liquid Crystals

Commercially available liquid crystal BL038 from Merck is a key ingredient used in the HPDLC recipe. It is a blend of short chain and long chain cyano biphenyls, 4-cyano-4'-n-pentylbiphenyl(5CB) and 4-cyano-4'-n-pentyloxybiphenyl(50CB)). It consists of rod shaped mesogens, which exist in the nematic liquid crystal phase between ambient temperature upto a clearing temperature T_c of 373.2 K. This is preceded by a nematic to isotropic (N-I) coexistence region of about 3 K. The LCs have an optical refractive index anisotropy value of 0.2720 and ordinary refractive index of 1.5270, which is index matched to the polymer refractive index of the HPDLCs.

3.1.2 Holographic Polymer Dispersed Liquid Crystals -Recipes

Two optimized acrylate and thiolene monomer based recipes are used for HPDLC formation.

Acrylate formulation

The acrylate based recipe is shown in Table 3.1. A photoinitiator mix consisting of Rose Bengal(RB), N-Vinyl Pyrrolidinone (NVP) and N-Phenyl Glycine(NPG) all

Table 3.1: Acrylate prepolymer recipe formulation

Ingredients	Product Name	Weight(%)
Liquid Crystal	BL038	32.4
Tri-Functional Oligomer	UCB4866	22.5
Hexa-Functional Oligomer	UCB4833	22.5
Photoinitiator	Rose Bengal	0.6
Coinitiator	N Phenyl Glycine	1.2
Solvent	N Vinyl Pyrrolidinone	10.8
Surfactant	Tween 80	10.0

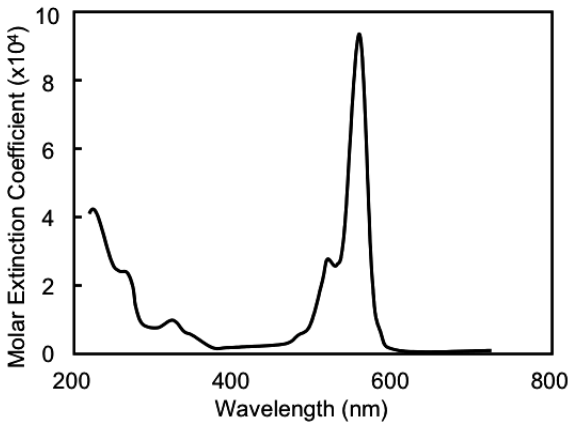

Figure 3.1: Absorption spectrum of Rose Bengal (source: http://www.sigmaaldrich.com)

purchased from Sigma Aldrich is added to a blend of tri and hexa-functional acrylate oligomers(Cytec), LC BL038(Merck) and surfactant Tween 80(Sigma Aldrich). After the prepolymer mix is uniformly blended it is placed between AR-ITO coated glass substrates spaced evenly using glass spacers(EMD). 5,10 and 20 μm thick spacers are typically used.This uniformly thick sandwich is placed in the holography setup to fabricate the HPDLCs.

The photo initiated polymerization takes place by the method of chain polymerization detailed in Sec.2.2. The photoinitiator RB has an absorption spectrum with peak absorption in the vicinity of laser wavelength 532nm as shown in Figure 3.1. RB sensitizes the prepolymer syrup to the laser wavelength. During the photopolymerization process RB absorbs the incident radiation and participates in electron transfer reaction with NPG where it is transformed to a radical by donating an electron[25].This NPG radical participates in the free radical polymerization of the acrylate oligomers. The NVP in the mixture furthers the cross linking of the polymers. At the bright regions of the laser interference patterns caused by the intereference of coherent 532nm laser beams, polymerization takes place. The monomers in the dark regions of the standing wave intensity pattern diffuse to the brighter regions to polymerize. LCs diffuse to the dark regions and they are now immiscible with the polymer, phase separating into droplets. The surfactant Tween80 used here reduces the electric field required to make the HPDLC optically transparent, improving its electro optic response. This is credited to change in the anchoring properties of the LC molecules at the polymer/LC interface[45].

One of the drawbacks of these acrylate based recipe are the long term stability of the HPDLCs in the presence of remnant unreacted photoinitiator which can generate free radicals deteriorating the quality of the polymer and LC. The monomer conversion is low in these systems due to early gelation time and the remnant monomer

Table 3.2: Thiolene prepolymer recipe formulation

Ingredients	Product Name	Weight(%)
Liquid Crystal	BL038	25.0
Monomer	NOA65	68.0
Photoinitiator	Rhodamine 6G	0.4
Coinitiator	Benzoyl Peroxide	3.0
Solvent	N Vinyl Pyrrolidinone	3.6

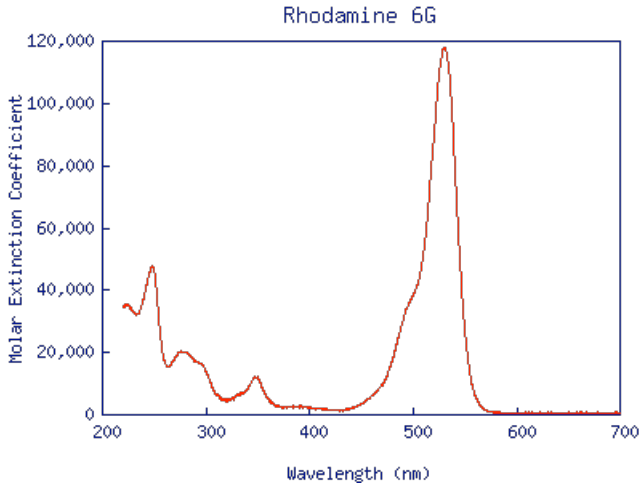

Figure 3.2: Absorption spectrum of Rhodamine 6G (source: http://omlc.ogi.edu)

further polymerize even after the grating is formed, resulting in negative effects of increased field bias required to transform them to an optical transparent state[46]

Thiolene Formulation

The thiolene recipe is shown in Table 3.2. Here the monomer NOA65(Norland Optical Adhesives) is uniformly blended with LC BL038 and the initiator components Rhodamine 6G(RH6G), Benzoyl Peroxide(BzO_2) and N-Vinyl Pyrrolidinone(NVP) all procured from Sigma Aldrich. This prepolymer blend is uniformly sandwiched

using spacers between ITO coated glass slides and placed in a holography setup.

Figure 3.2 is the absorption of the initiator spectrum of RH6G. It can be noted that it has a high absorption spectrum at 532nm. Here BzO_2 is a coinitiator with NVP being a good solvent in the reaction. In the presence of light radiation electron transfer takes place between the initiator and the coinitiator. The coinitiator BzO_2 forms the radical benzoyl-oxy which initiates the polymerization[47]. The polymerization takes place by the method of step polymerization explained in detail in Sec.2.2.

The growth of polymer is different for the acrylate and thiolene formulation. In the step polymerization technique in thiolene formulation the monomers tend to be exhausted fast in the beginning of the reaction and they slowly form higher molecular weight polymeric chains and then react with each to form longer chains. The morphology of the HPDLC formed imaged using SEM indicate almost spherical LC droplets without much overlapping due to the lower reaction speed during fabrication. They also tend to have polydispersity in their size.

In the chain polymerization technique of acrylate the growth mechanism of the polymer chain is very fast. Most of the conversion of monomers to high molecular weight polymers is simultaneous. The growing polymers chains do not tend to react with each other but the polymer chain react with monomeric units. The morphology of the HPDLCs for acrylate formulation from SEM indicate polydispersity in the droplet size and shape. Typically the LC droplets are elongated along the LC layer and they tend to overlap. The fast polymeric conversion and unreacted monomers during the polymerization contribute to heterogeneity during the polymerization and contribute to the irregular shaped LC droplet formation.

3.2 Experimental Methods

In this section the holographic setup used for HPDLC fabrication and the characterizing techniques to analyze the HPDLCs are discussed.

3.2.1 Holography Formation Technique

A solid-state 5W output Verdi laser from Coherent Inc is used for hologram formation. Inside the laser, ND:YAG crystal is placed as a gain medium along with a doubling crystal for frequency doubling, which outputs a wavelength of 532nm. The laser output has a long coherence length and also has frequency, pointing and power stability making it ideal for hologram formation.

Two types of setups are assembled based on fabrication of transmission or reflection mode grating. The interference pattern generated from these holography setup are made incident on uniformly spaced HPDLC prepolymer cells to create the desired type of gratings.

Transmission Grating Fabrication Setup

The schematic for transmission grating fabrication is shown in Figure 3.3(a). Here the laser source is split into two equal intensity beams by a 50/50 beam splitter. The two coherent beams are made incident on the same side of the HPDLC sample cell as shown in the figure. The grating formed has its Bragg planes perpendicular and grating vector parallel to the glass substrate.

Reflection Grating Fabrication Setup

Two beam method, one beam method and prism method are primarily used for reflection grating fabrication. In a reflection type grating the Bragg layers are parallel and the grating vector perpendicular to the glass substrate.

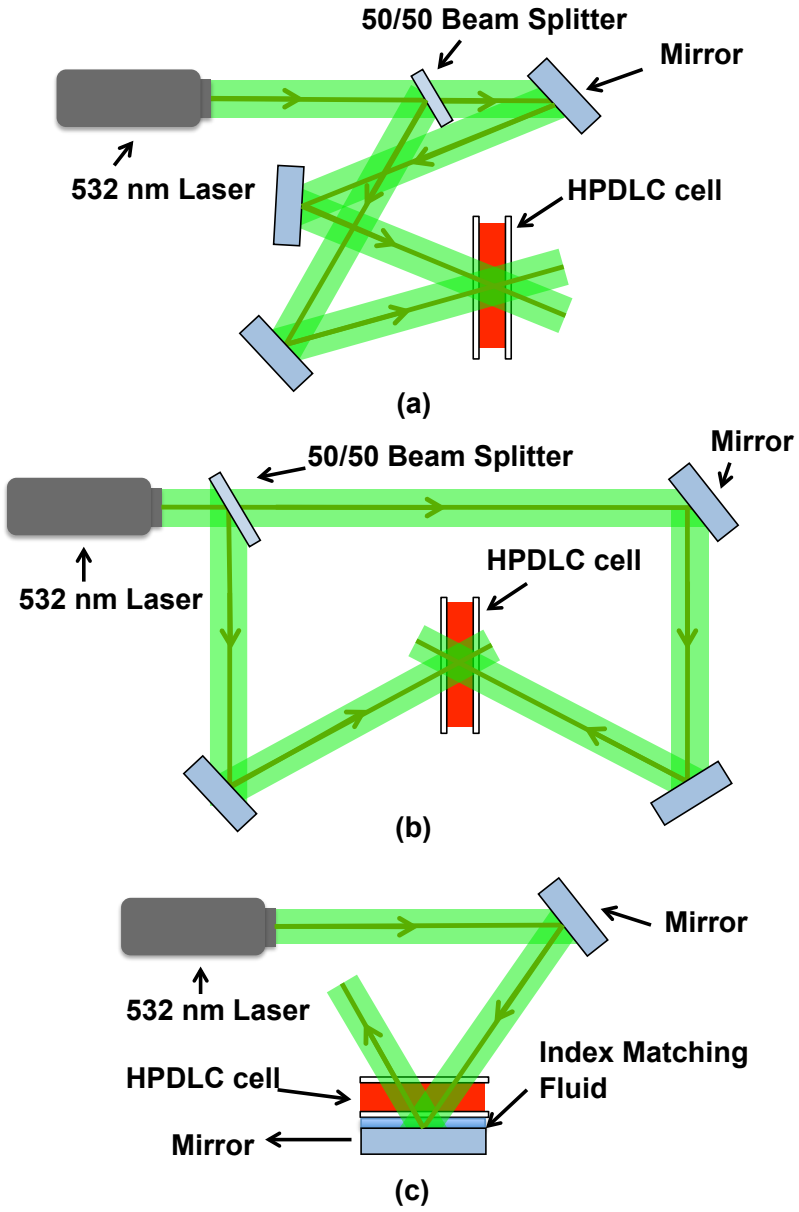

Figure 3.3: Schematic of the fabrication setup for (a) transmission grating (b) two beam reflection grating and (c) one beam reflection grating

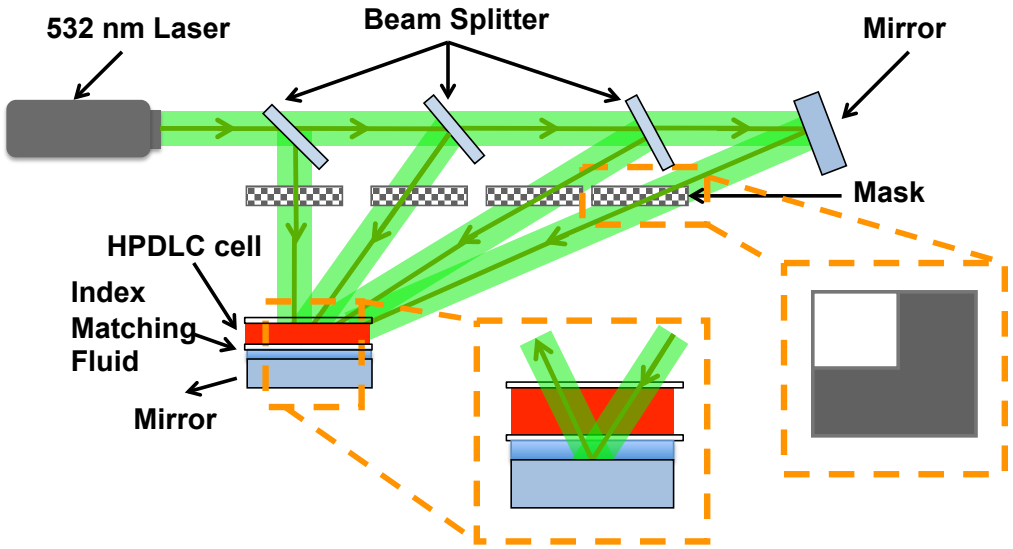

Figure 3.4: (a) Fabrication configuration for Pixelated Setup

Two Beam Technique and One Beam Technique In the two beam geometry shown in Figure 3.3(b) the laser source is split into two equal power beams using a beam splitter and made to interfere on the opposite sides of the HPDLC prepolymer cell with the aid of mirrors.

In the one beam setup shown in Figure 3.3(c), a mirror is placed flush against the sample cell with the index matching fluid glycerine placed between them. When the laser beam is incident on the cell it transmits and then reflects back through it due to the mirror. The transmitted and reflected counter propagating beams interfere and the prepolymer cell forms a reflection Bragg HPDLC.

Both two beam and one beam methods can be used to create HPDLCs with different reflection notches by varying the angle of incidence of the laser beam on the sample cell during fabrication. These methods of formation are used to create multiple gratings which are stacked serially for the spectrometer application. To create spatially arranged pixilated HPDLCs one beam method is used. Four square HPDLCs are fabricated in a single medium. In this setup the laser beam is split into

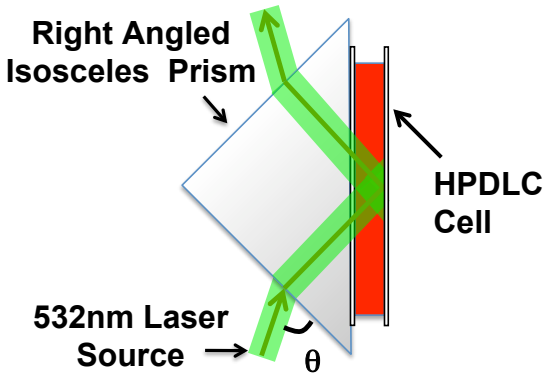

Figure 3.5: Schematic of the HPDLC fabrication using the prism method

four equal intensity beam as shown in Figure 3.4. Inset of the sample cell shows one of the four beams creating a HPDLC pixel using one beam method. The other inset shows the mask used to create each of the four HPDLCs.

Prism Technique A single-beam prism coupled geometry is used for the hologram formation. The glass prism geometry is 90° isosceles. The prepolymer sample is placed against the hypotenuse or long side of this right angled prism using an index matching fluid. In this technique interference between the incident and the reflected beam (generated by total internal reflection of incident beam) at the long edge of the prism results in the formation of reflection gratings. The schematic for HPDLC fabrication using prism setup is depicted in Figure 3.5.

Rotating the prism geometry different grating pitches can be generated. Anticlockwise prism rotation without moving the laser source resulting in increasing values of θ reduces the grating pitch of the fabricated HPDLCs. Rotating prism clockwise results in increased grating pitch of HPDLCs.

Grating Superimposing Technique This technique uses the prism method to create multiple gratings in a single medium. Figure 3.6 is the schematic depiction

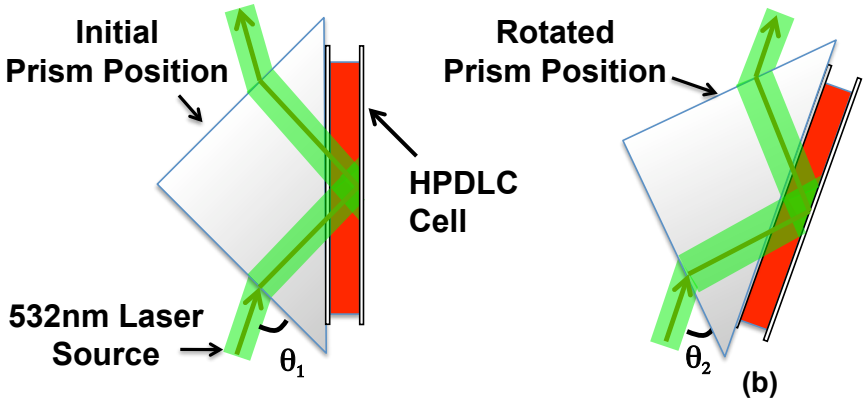

Figure 3.6: Schematic of the superimposed grating fabrication setup by prism rotation.(a) Grating fabrication setup with the prism in its initial position with the laser incident at an angle of θ_1 and (b) fabrication setup for superimposing the previously formed grating by moving the prism to form an angle θ_2 with the laser beam

of this setup. Initially a grating is formed at an incident beam angle θ_1 as shown in Figure 3.6(a). Before complete gelation of the grating takes place the prism is rotated to form an angle θ_2 with the incident laser beam as shown in Figure 3.6(b). This results in the formation of superimposed gratings

3.2.2 Traditional Experimental Analysis Techniques

Parameters such as the thickness of the thin film, morphology features, interfacial roughness between the polymer and LC layers, LC orientation in the droplets are important considerations for the electrical and optical performance of the thin films. Hence multiple characterization techniques are used for thin film HPDLC analysis. Spectroscopy, wavefront sensing, interferometry and microscopy are some of the important characterization tools used. A brief review on employing few of these techniques for HPDLC analysis is described here.

Field Response

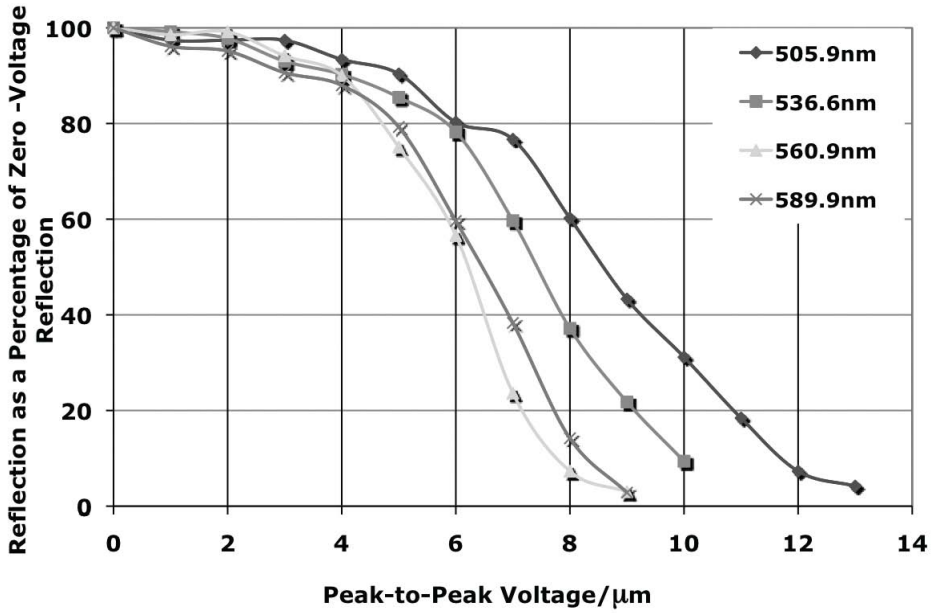

Figure 3.7: Transmission intensity response of the individual layers of the stacked HPDLCs for varied applied voltage

Reorientation Field When a voltage applied across the HPDLC is sufficiently high it is rendered optically transparent reversing its wavelength selective property. The required voltage V varies with the thickness of the grating and a better characterizing term is the field E determined by V/d where d is the thickness of the HPDLC film. Different characteristic properties of the HPDLCs control the field required for reorientation of LC molecules. Some of the parameters are LC droplet size, shape, dielectric anisotropy and its anchoring at the LC/polymer interface, polymer composition and HPDLC film conductivity and its dielectric constant. Electron spin resonance spectroscopy detailed in Section 4.2 aid in the understanding of the effect of field on the droplet orientation.

The field applied reorients the LC droplets by overcoming the confinement effect which oppose their reorientation. Critical field to reorient the LC molecules in micron sized PDLC droplets with bipolar orientation has been determine by Wu et. al. and

can be applied to the nanometer sized HPDLC globules. Critical field E_c is determined as [48]

$$E_c = \frac{1}{3a}(\frac{\sigma_2}{\sigma_1} + 2)\sqrt{(\frac{K(l^2-1)}{\triangle\varepsilon}} \tag{3.1}$$

where a and b are the length of the semi major and minor axis with l determining the aspect ratio of the droplets. σ_1 and σ_2 are the conductivities of the polymer and the LC material. $\triangle\varepsilon$ is the dielectric anisotropy of LC and K is defined as the deformation constant. From this equation it can be inferred that bigger sized LC droplets defined by the parameter a but with low aspect ratio l improve the switching field of the HPDLCs. LCs with high dielectric anisotropy and low conductivity, while polymer matrix with higher conductivity also aid in improving the field response.

To experimentally measure the field response a 1 kHZ square voltage varying from 0 to $200V_{pp}$ is applied to the conductive leads soldered on to the ITO electrodes coated on the HPDLC substrates. Here V_{pp} is the peak to peak voltage measurement. Variable square wave voltage was generated by an Agilent 33220A arbitrary wavefront generator. Its maximum output voltage of $10V_{pp}$ was amplified by Trek PZD 700 voltage amplifier and applied across HPDLC film.

The field response was measured by detecting the diffraction efficiency response by a spectrometer for variable voltage. The accuracy of the variable voltage source for switching was measured using a multimeter.

Figure 3.7 shows the switching response of four different wavelength of HPDLCs for acrylate recipe. From the Bragg grating equation of 2.13 the reflected wavelength $\lambda_R \propto \Lambda$. Thus HPDLCs with higher reflected wavelength have bigger droplet domains. This improves the switching response as determined by Equation 3.1 where critical field $E_c \propto 1/a$. As seen in the Figure 3.7 graph higher wavelength reflecting HPDLCs have lower switching voltages compared to the lower wavelength reflecting HPDLCs, primarly due to bigger LC globules. Sometimes HPDLCs show increased reflectance

instead of the expected decrease at lower applied fields. This is because the low field aid confinement effects in improving the refractive index mismatch of LCs in some of the droplets of the polydisperse LC droplet distribution. However as the field is increased the LC molecules overcome the confining effects and reorient in the direction of the field.

The acrylate based recipe require higher fields compared to the thiolene based HPDLCs for reorientation. High droplet shape anisotropy l and rough LC/polymer interface which may contribute to stronger anchoring at the interface, of acrylate based HPDLCs make it more difficult to reorient the LC molecules. In comparison thiolene based HPDLCs have almost spherical droplet shapes and smoother interfaces as observed from SEM micrograph.

The average value of switching field for acrylate recipe is in the range of $12V_{pp}/\mu m$ while that for the thiolene recipe used here is in the range of $6V_{pp}/\mu m$.

Response time The field response time defined by the parameters rise time τ_{on} and fall time τ_{off} quantify the time required for the HPDLC to transform between a wavelength selective state and optically transparent state and are important considerations for HPDLC switch applications. The rise time is the time taken by the HPDLC film to respond to applied electric field E_{app} and change to optically transparent state. This response determined by Wu et. al for PDLCs which can be conveniently applied to HPDLCs and is determined as[48]

$$\tau_{on} = \frac{\gamma_1}{K\left(l^2-1\right)/a^2 + \triangle\varepsilon E_{app}^2}$$

The fall time which defines the time taken by the HPDLC film to transform from optically transparent state to wavelength selective state when the applied field is

removed is [48]

$$\tau_{off} = \frac{\gamma_1 a^2}{K\left(l^2 - 1\right)}$$

where γ_1 is defined as the rotational viscocity coefficient.

From the rise time and fall times it can be inferred that larger droplets have a slower response time since $\tau \propto a^2$ while droplets with higher shape anisotropy l have a better response time.

Experimentally the rise and fall time of the reflection type HPDLC thin film can be measured by analyzing the HPDLC response to a incident source whose wavelength corresponds to its Bragg wavelength, when a field is applied or removed. Source wavelength corresponding to Bragg wavelength of HPDLC is made incident using Newport's Oriel monochromator. The transmitted intensity variation due to field response of HPDLC is detected by a fast response PIN photodiode connected to a oscilloscope. The oscilloscope displays the HPDLCs intensity response with time as a waveform. The rise and fall times are determined by following the change from 10% to 90% of the intensity variation when field is applied or removed. The rise time and fall time for acrylate formulation determined by this method was $330\mu s \pm 15\%$ and $280\mu s \pm 15$. The response time of thiolene is typically much slower than acrylate formulation. It has been determined to be 5 times slower for thiolene formulation comparatively[49]. One of the reasons is that acrylates have bigger shaper anisotropy l resulting in better response times since τ decreases with increasing l.

Thus difference in polymer morphology, elasticity, LC droplet shapes, LC/polymer interface contribute to different fields for complete switching and response times for acrylate and thiolene based HPDLC recipes.

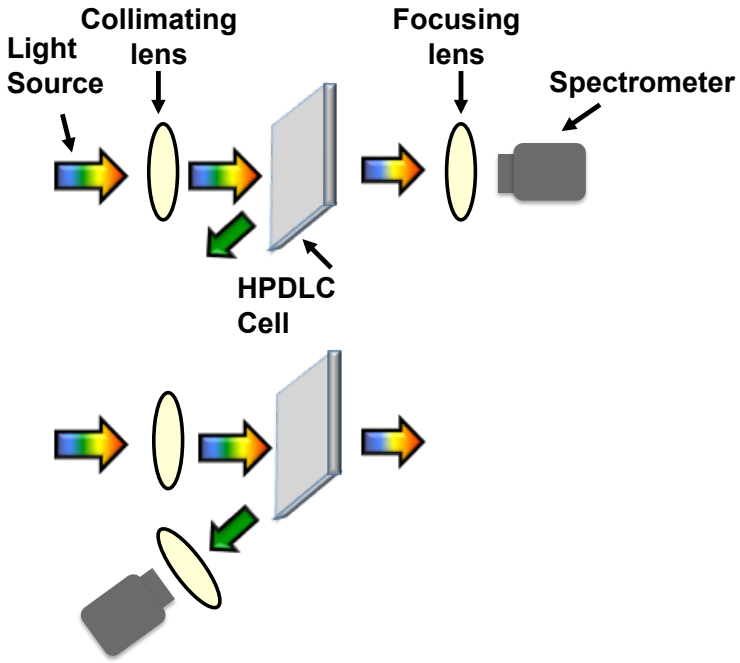

Figure 3.8: Spectrometer setup for measuring the transmission and reflection spectrum of HPDLCs

Spectrometry

Optical charaterization of the HPDLC gratings are made by using a HR4000CG-UV-NIR spectrometer(Ocean Optics). The spectrometer characterizes the wavelength spectrum using a dispersive diffraction grating. This is a useful technique to determine the grating formation, quality of the grating, measurement of the diffraction efficiency. All the reflection and transmission spectra in this dissertation were analyzed with this spectrometer.

Figure 3.8 shows the positioning of the spectrometer in a setup to capture the transmitted and reflected spectrum from HPDLCs.

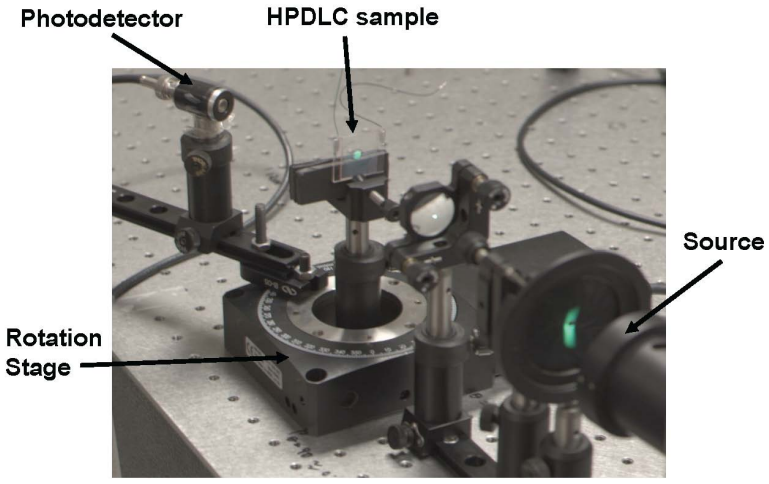

Figure 3.9: Setup for analyzing the scattering profile of HPDLCs

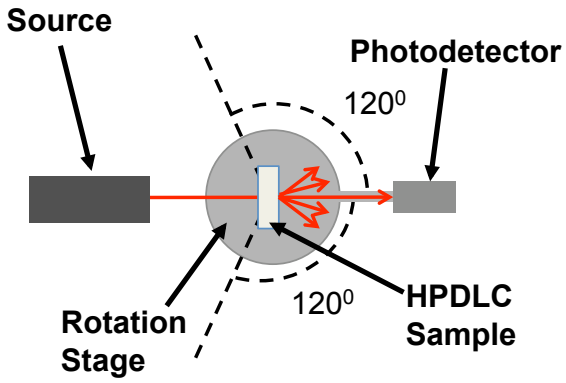

Figure 3.10: Setup

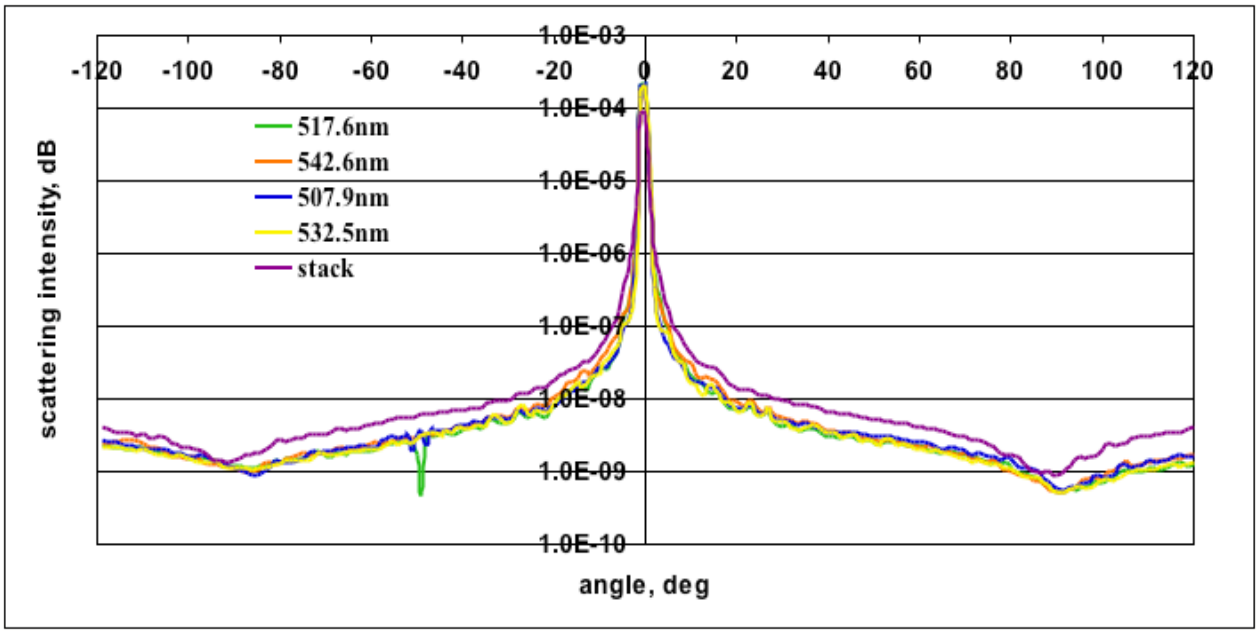

Figure 3.11: Scattering Intensity vs. Angle

Scattering Profile Analysis

The incoherent scattering reduces the transmittance intensity based on the wavelength. When the HPDLCs are stacked this type of scattering is more significant. It can be clearly noticed by comparing the scattering profile of the source wavelength through a HPDLC and a stack of HPDLCs, for different angles. The comparison was performed using the setup shown in Figure 3.9 which is schematically represented in Figure 3.10. A 632 HeNe laser was used as the probe beam for the HPDLC sample. The data was acquired upto 240° angle arc starting at −120° with respect to the forward scattering direction (laser, sample and detector are in-line) to 120°. A photodiode was attached to a rotating stage which captured the intensity scattered from -120 to +120.

The scattering profile obtained by this technique is shown in Figure 3.11. Here two contributions can be seen in the scattering transmittance profile. In the vicinity of 0°

the incident intensity is observed through the HPDLC with weak scattering effects. At wider angles only incoherent scattering is observed. Observing the scattering effect from a stack of four layers we notice that the transmittance of the incident beam is lower and the scattering at wider angles is higher than the single HPDLC layers. This implies that there is a significant loss in transmitted intensity in stacked layers due to incoherent scattering. This study further motivates the need for single layer broadband wavelength interacting HPDLCs in comparison to stacked HPDLCs to reduce the scattering effects.

3.2.3 Wavefront Analysis

It is critical that the interaction of incident wavelength spectrum with HPDLCs should not cause significant unexpected distortions in the spectrum. The quality of the wavefront transmitted through the HPDLCs and the tolerance limits of the final wavefront can be quantified by using interferometric and wavefront sensing techniques.

Interferometer techniques require that the test source is highly coherent such as a laser source. Typically the test source is split into two beams. One of the beams is passed through the test optics and then both the beam are made to interfere. A detector such as a CCD images this and software analysis is performed to determine the wavefront abberation parameters. Some of the prominent interferometer configurations are Twyman-Green, Mach-Zehnder and Fizeau interferometers[50].

Previously interferometric technique analysis was performed on HPDLCs by passing a test wavefront repeatedly twice through the sample[51]. This was analyzed visually and by software to find the distortion effects. It was determined that the surface of the test samples had a peak to valley surface error of 3nm.

Optical profilometers using optical phase shift interferometry technique such as Zygos New View series, accurately determine the HPDLC 3D profile metrology and

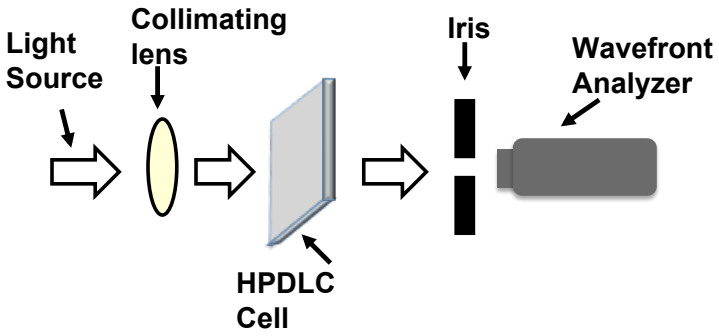

Figure 3.12: Wavefront Analysis Test Setup

Table 3.3: Zernike coefficients of primary aberrations for electric field off and field on state of HPDLC

Aberration Parameters	Electric Field Off	Electric Field On
Z_1, X-Tilt	0.000076	-0.003569
Z_2, Y-Tilt	-0.002449	-0.004120
Z_3, Focus	-0.000000	-0.000000
Z_4, 0-Astigmatism	-0.068296	-0.062906
Z_5, 45-Astigmatism	0.012584	0.005367
Z_6, X-Coma	-0.001767	0.002862
Z_7, Y-Coma	-0.003398	-0.001692
Z_8, Spherical	0.004134	0.001780

will be discussed indepth in the next chapter.

For wavefront sensing techniques a low coherent broadband white light source can be used to determine the quality of the optical grating. In this dissertation we use the Shack-Hartmann wavefront sensing technique[39, 52] to determine the wavefront aberrations effects when a white light is passed through the HPDLC thin film.

‘

Flat and aberration free wavefront diffracted through HPDLC is a critical aspect for many of of its applications. In this section a white light source is made incident on

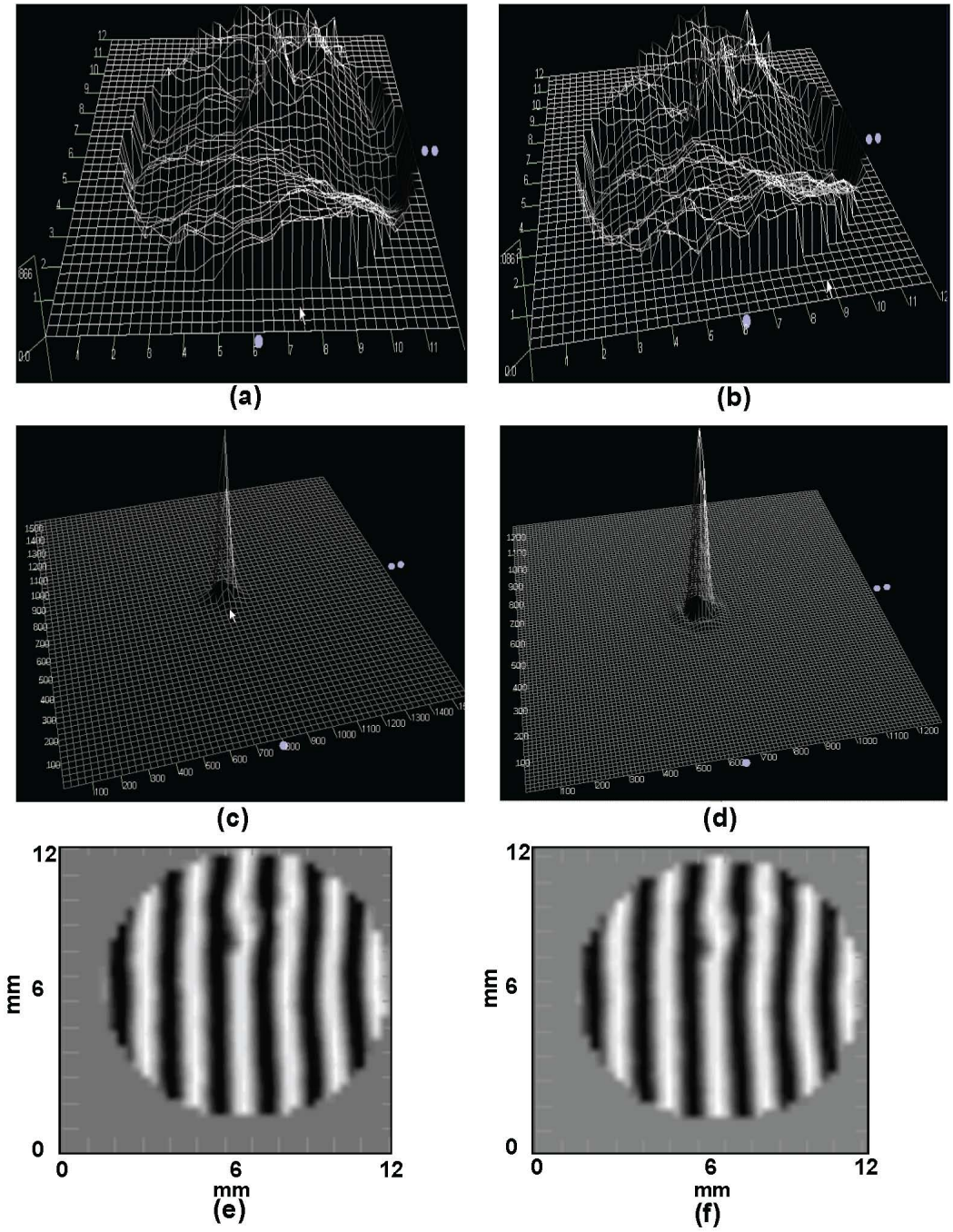

Figure 3.13: 3D view of Optical Phase Delay for (a) field off state and (b) field on state. 3D view of Strehl ratio for (c) field off state and (d) field on state. Fringe pattern generated by the wavefront analyzer characterizing the optical wavefront transmitted from a HPDLC for (e) Field off state and (f) Field on state

Table 3.4: Wavefront characterizing parameter of electric field off and field on state of HPDLC

Parameter	Electric Field Off	Electric Field On
P- V	0.1727	0.1637
Strehl Ratio	0.8666	0.8717
RMS Wavefront Error	λ/16.5	λ/ 18.5

the HPDLC and the wavefront transmitted through it is characterized using a wavefront analyzer. Wavefront analyzer from Adaptive Optics based on Shack Hartmann principle[39] and white light source from Ocean Optics are used.

For the analysis the white light source, HPDLC sample and wavefront analyzer are placed inline as shown in Figure 3.12. Reference wavefront and test wavefront are measured respectively. Reference wavefront is measured by capturing the collimated white light source by the detector directly without HPDLC sample. Test wavefront is measured by transmitting the collimated white light source through the HPDLC before being analyzed by the wavefront analyzer. Inside the analyzer each of the wavefronts are individually passed through an array of lenses of the same focal length called the Micro Lens Module(MLM). This module breaks the entire wavefront into smaller wavefronts and focuses it onto a CCD. The deviation of the incident wavefront from the focal spot of each lens detected on the CCD sensor is sampled, software analyzed and curve fitted for an approximate wavefront envelope. Finally depending on the deviation of the test wavefront focal spots compared to the focal spot of the reference wavefront the aberrations are computed. The test wavefront is characterized for both field off and field on state of HPDLC.

The wavefront emerging from an optical system can be written in terms of the

Zernike polynomial coefficients $Z_i\,(i = 0 \ldots 8)$[41] as :

$$\begin{aligned} W(\rho,\theta) &= Z_0 + Z_1\rho\cos\theta + Z_2\rho\sin\theta + Z_3\left(2\rho^2-1\right) + Z_4\rho^2\cos 2\theta + Z_5\rho^2\sin 2\theta \\ &\quad + Z_6\left(3\rho^2-2\right)\rho\cos\theta + Z_7\left(3\rho^2-2\right)\rho\sin\theta + Z_8\left(6\rho^4-6\rho^2+1\right) \quad (3.2) \end{aligned}$$

where ρ is the radial coordinate and θ is the angular coordinate in the polar coordinate system considered. The Zernike coefficients quantifying aberration parameters tilt, coma, defocus, spherical aberrations and astigmatism are tabulated for both field-off and field-on state in Table 3.3. Other wavefront characterizing parameters Peak to Valley (P-V), RMS wavefront error, and Strehl ratio listed in Table 3.4 are determined for field-off and field-on state. P-V describes the maximum variation of the actual wavefront from the desired wavefront. Since P-V is a measure of the maximum error and does not give a quantification over the entire region where the error occurs it cannot be used as a sole characterizing parameter. A system with a large P-V aberration in a small region maybe better suited than that with a small P-V with a large area wavefront error. The RMS wavefront error is more significant for defining the wavefront quality and it expresses the wavefront variations averaged over the entire wavefront. The rms wavefront error σ and variance σ^2 for a circular pupil expressed in the polar coordinate system (ρ,θ) is defined by [41]:

$$\sigma^2 = \frac{1}{\pi}\int_0^{2\pi}\int_0^1 \left[\Delta W(\rho,\theta) - \Delta\overline{W}\right]^2 \rho d\rho d\theta, \quad (3.3)$$

where ΔW is difference of the actual wavefront relative to a best fit spherical wave and $\Delta\overline{W}$ is the mean wavefront optical path difference between the actual aberrated and ideal wavefront.

Figure 3.13(a) Figure 3.13(b) show a 3D optical phase delay(OPD) map of the wavefront for electrical field off and field on state over a circular pupil. The map

distortions can be characterized by P-V, RMS wavefront error and the Zernike coefficients. The wavefront aberration in a HPDLC system as indicated by the Zernike coefficient, P-V, RMS and Strehl ratio values form Table 3.3 and Table 3.4 are chiefly due to the interfacial roughness between the LC rich and the polymer rich layers and index mismatch between these two alternately placed layers. When an electric field is applied across the HPDLC the refractive index becomes uniform and the wavefront emerging from it has less aberration compared to the unswitched HPDLC as evident in the two tables above. The wavefront characterizing parameter, Strehl ratio is the ratio of the maximum intensity due to a point source in the presence of aberration, to the theoretical maximum intensity of a perfect system without any aberrations. The Strehl ratio expressed in the polar coordinate system (ρ, θ) is given by [41]:

$$\text{Strehl Ratio} \quad = \quad \frac{1}{\pi^2} \left| \int_0^{2\pi} \int_0^1 e^{i2\pi\Delta W(\rho,\theta)} \rho d\rho d\theta \right|^2 \tag{3.4}$$

Figure 3.13 (c) Figure 3.13(d) indicates 3D Strehl ratio plot for the HPDLC in switched and unswitched state.

From the Table 3.4 comparing the switched and unswitched HPDLCs it is evident that the P-V value and the RMS wavefront error decreases by 5.5% and 10.6% respectively and Strehl ratio improves by 5.9% in the switched state suggesting a reduction in aberrations and more intensity at the detector. Overall the abberation values according to the Maréchal criterion suggest that HPDLCs have good optical performance for both electric field applied and no field applied case. This criterion states that a system quality is well corrected if the Strehl ratio is ≥ 0.8 corresponding to an RMS wavefront error of $\leq \lambda/14$[41].

Figure 3.13(e) and Figure 3.13(f) shows the reconstructed optical wavefront viewed as a fringe pattern for both unbiased and biased state. Ideally the fringe pattern or interferogram of a unaberrated optical system exhibits a sharp contrast between the

bright and dark fringes and is perfectly parallel to each other[50]. A slight curvature in the fringes detected in the interferogram primarily result from the astigmatism introduced in the wavefront transmitted through the HPDLC sample as shown Table 3.3. The kink in the top central region of the fringe pattern is due to the presence of air bubble trapped inside the HPDLC during grating formation.

Thus it can be deduced that HPDLCs transmits good optical quality flattened wavefront suitable for multiple application from Figures 3.13(a)-(f), Table 3.3, Table 3.4 and Maréchal criterion.

Imaging Techniques

Imaging techniques such optical microscopy, atomic force microscopy(AFM), scanning electron microscopy(SEM), transmission electron microscopy(TEM) are considerably used for the visual inspection of phase separation between LCs and polymer, the LC droplet diameter, droplet structure, grating pitch, droplet dispersion, droplet density determination etc.,

Optical microscopy is the most basic technique used for imaging the surface topography of thin film PDLCs[8]. It is a convenient technique for observation of surface morphology with feature size in the micrometer range without needing elaborate sample preparation. The micron sized droplets of the PDLCs can be analyzed for director orientation using the polarized optical microscopy(POM) where the sample is placed in a optical microscope between two crossed polarizers.

It can also be used for instant imaging of HPDLC thin films having micrometer scale grating pitch, such as the grating pitch of transmission mode HPDLCs. Here a light microscope images the sample cell placed between crossed polarizers. However due to lack of high resolution imaging capabilities this method cannot be used for extensive morphological analysis.

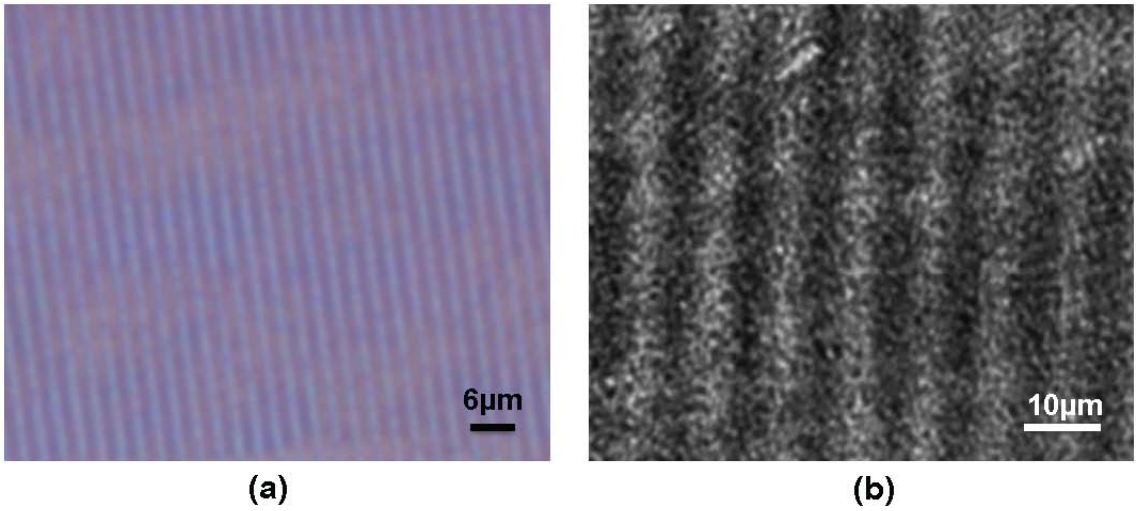

Figure 3.14: (a)Polarized optical microscope image of HPDLC and b) Differential interference contrast microscope image of HPDLC

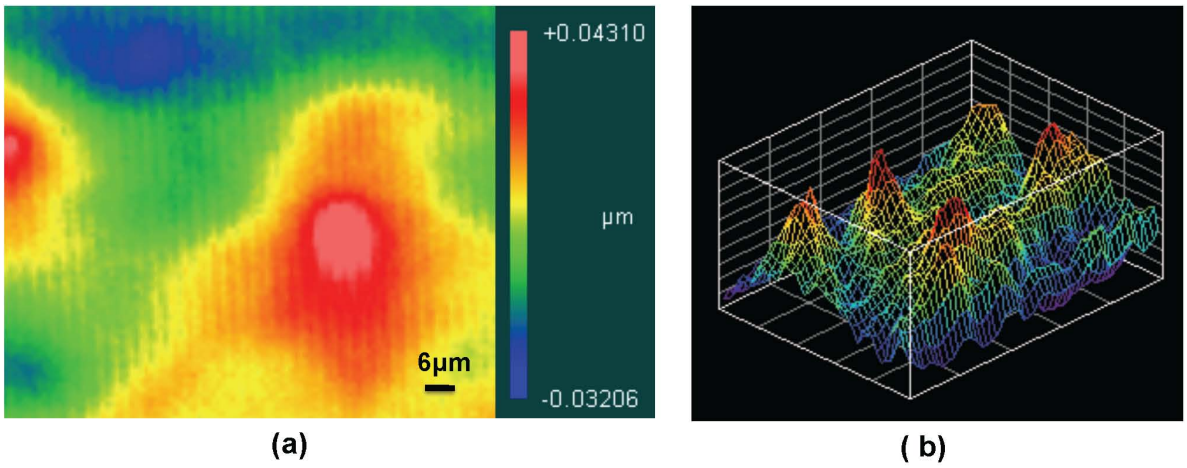

Figure 3.15: (a) Optical Profilometer image of HPDLC grating structure and (b) 3D surface profile

In an HPDLCs the droplets are far smaller than micron size and the LC orientations in the droplets cannot be resolved. However they are a convenient method to find the grating pitch of the transmission mode HPDLCs. The polymers layers appear dark under crossed polarizers and the LCs appear bright because of their phase shifting property denoted by the Equation 2.6 .

A transmission HPDLC with 3μm grating pitch is imaged by Leica DMLP optical microscope under crossed polarizers as shown in 3.14(a).

Differential interference contrast(DIC) is another type of optical imaging technique which requires no sample preparation for fast imaging of micrometer scale features in HPDLCs. DIC enhances the contrast in transparent samples using interferometry technique. Figure 3.14(b) is the transmission HPDLC imaged using the DIC technique.

It is crucial to measure the critical dimensions of an HPDLC, such as its thickness, to ensure its uniformity during holographic fabrication. This guarantees consistent optical and electrical performance. Optical profilometers such as Zygos New View series, which use an optical phase shift interferometry technique, accurately determine the HPDLC 3D profile metrology. This is a quick non-contact method, which is non-destructive to the sample and also does not require sample preparation. Figure 3.15(a) is the surface image of the transmission HPDLC revealing the grating structure obtained by the Zygo New View 6000 optical profilometer. The 3D view of the imaged surface is shown in Figure 3.15(b)

AFM has been used for the analysis of the dimpled polymer structure at the LC/polymer interface of the HPDLCs[53]. Tapping technique was used here to prevent damage to the soft polymer interface. There is a limit on the maximum height and maximum area this technique can image which is the range of several micro meters. Also the image scanning process can take several minutes with increased

likelihood of artifacts in the image.

SEM and TEM are two well-known microscopy techniques used for nanometer scale structural analysis of HPDLCs[54].

The conventional high vacuum SEM(HV-SEM) technique requires the test sample be placed in a near vacuum chamber. The sample preparation involves freezing fracturing the required surface cross section accompanied by LC removal and treatment with a conductive coating as mentioned in Section 2.6.1.

TEM technique used for morphological analysis typically requires an embedding process followed by sectioning. The embedding process results in leaching of impurities into the grating structure leading to alteration of the grating pitch.

The sample preparation of both TEM and SEM are labor intensive. In order to determine the accurate high-resolution features of the grating structure it is essential that LC is not removed from the grating structure and the sample surface is not chemically treated resulting in possible distortion of the features.

Cryo-SEM has been used recently to preserve the grating structure for imaging without LC removal. Here the sample is frozen and imaged without LC removal[55]. Cryo-SEM sample preparation requires initial freeze fracturing of the surface using liquid nitrogen at about a temperature of -182^0C. To apply a conductive coating on the sample the temperature is increased to about -900C and cooled back to -182^0C prior to imaging. The cryogenically fixed sample is imaged in a SEM cryo-stage.

VPSEM and ESEM are two techniques described in detail in the next chapter used here for the first time for morphology study of HPDLCs at high resolution without the need for LC removal or conductive coating. The specimen preparation involves freeze fracturing the sample followed by imaging in the SEM chamber.

This chapter details the recipe of HPDLCs used for the wavelength sensing along with different fabrication setup configuration. Experimental analysis techniques to

analyze the gratings are reviewed. We introduce two new types of high resolution imaging techniques namely VPSEM and ESEM in the next chapter without the need for LC removal or conductive coating. Electro spin resonance spectroscopy technique is detailed to study the confinement effects on LCs in the polymer matrix of the HPDLCs.

4. Novel Experimental Analysis Techniques

To study the nanoscale morphology of HPDLCs variable pressure SEM(VPSEM) and Environmental SEM(ESEM) are used here and compared to the typical HV-SEM imaging used for analysis. Electron spin resonance(ESR) spin probe technique is used to determine the LC droplet organization inside the polymer layers and the local director configuration of nanoscale sized LCs.

4.1 HV-SEM, VPSEM and ESEM

High-resolution scanning electron microscope imaging is an essential tool to understand and analyze the morphological features of electro-optic devices with nanoscale features. SEM of samples under high vacuum(HV) condition is a well-known technique used for high-resolution analysis of HPDLC structure where the LC is removed prior to imaging. In this work the grating structure is imaged for the first time using variable pressure SEM (VPSEM) without LC removal and compared to the imaging from conventional HV-SEM technique. Environmental SEM(ESEM) method is also used for imaging the HPDLC for the first time.

HPDLC is prepared using acrylate formulation shown in Table 3.1. To prepare the HPDLC sample for HV-SEM imaging the sample surface is first cryogenically frozen by placing it in liquid nitrogen dewar. The frozen surface is fractured to attain well preserved requisite sections for imaging. LC is removed by treating it with methanol to prevent damage to the HV-SEM apparatus. The sample is then sputter coated with 3nm thick platinum-palladium coating to enable good contrast, high resolution and prevent charge accumulation in the specimen. For the VP/ESEM imaging the sample is freeze fractured and directly placed in the SEM chamber. Zeiss Supra 50VP

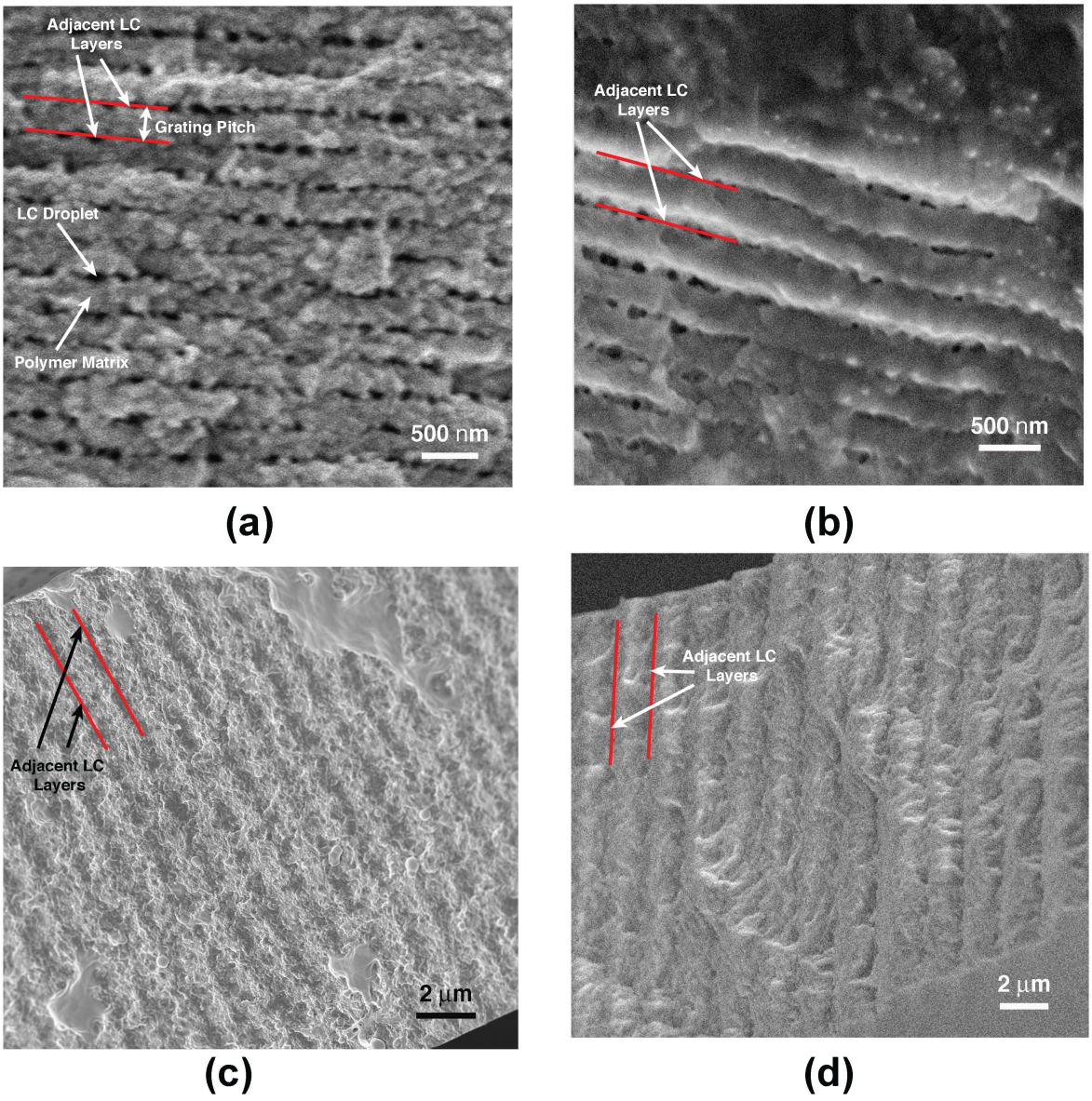

Figure 4.1: SEM images of the cross section of HPDLCs are shown here. a) HV-SEM image of reflection mode HPDLC b) VPSEM image of reflection mode HPDLC c) HV-SEM image of transmission mode HPDLC and d) VPSEM image of transmission HPDLC

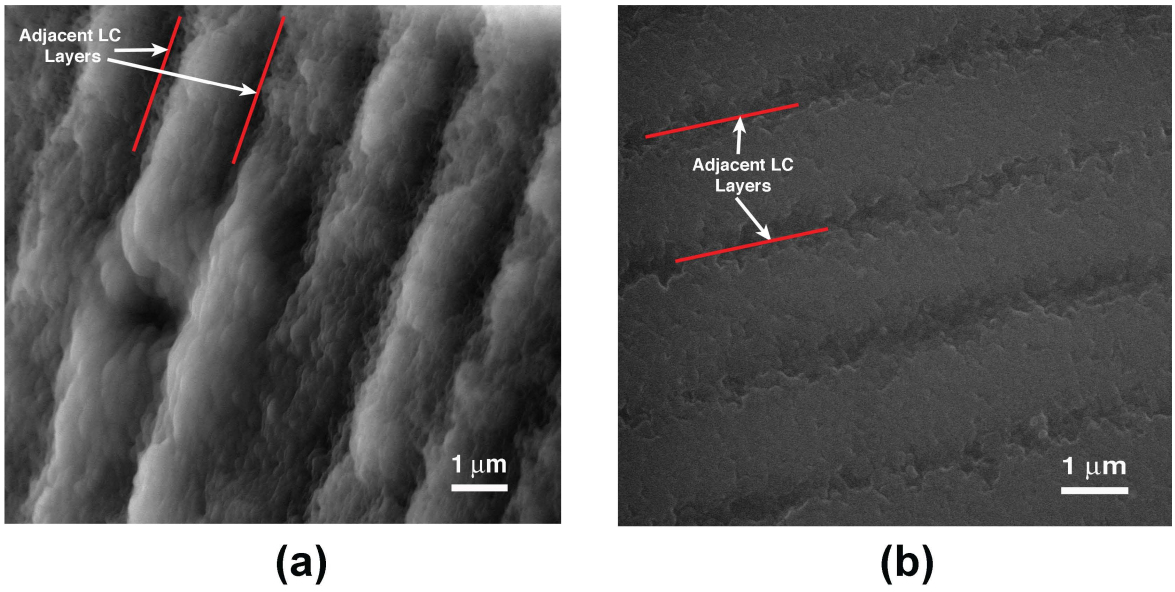

Figure 4.2: ESEM images of the transmission mode HPDLCs are shown here. a) Image of the surface feature and b) image of the cross section

is used for both HV-SEM and VPSEM imaging. FEI XL30 is used for ESEM imaging.

The HV-SEM imaging was performed at an accelerating voltage of 2kV with vacuum like conditions in the SEM chamber. The reflection HPDLC cross section was imaged using SE detector and transmission HPDLC cross section was imaged with Zeisss patented In-lens SE detector. The VPSEM was performed at 4 kV with VPSE detector was used for both reflection mode and transmission mode HPDLC imaging. Chamber pressure was set at 20Pa. A GSE detector was used for ESEM imaging with beam accelerating voltage of 10 kV. The pressure inside the SEM chamber was set at 3 Torr.

Figures 4.1(a)-4.1(d) show the SEM images of the HPDLC grating structure imaged using the HV-SEM and VPSEM. Figures 4.1(a) and 4.1(b) are the reflection mode HPDLC images and Figures 4.1(c) and 4.1(d) are the transmission mode HPDLC images.

Here the black voids are the LC droplets regions and the area surrounding them is the polymer matrix as indicated in Figure 4.1(a). The LC layered structure is illustrated by drawing lines at the center of two adjacent LC layers shown in Figures 4.1(a)- 4.1(d). Figure 4.1(a) also illustrates the grating pitch, which is the thickness of one layer of polymer and liquid crystal or distance between the centers of two adjacent LC layers. As seen in the SEM images the grating pitch of the reflection HPDLCs are lower typically less than 400nm resulting in smaller LC droplets. The grating pitch of the transmission HPDLCs are greater than about 600nm resulting in larger LC domains in the LC layers.

The LC droplets vary in size, shape and are interconnected in acrylate recipe[8]. These SEM images provide morphological details from the HPDLC cross-section such as the LC size and shape distribution. For reflection mode HPDLCs shown in Figures 4.1(a) and 4.1(b) there is polydispersity of the droplet size and shape and the droplets on an average are elongated along the LC layer. The transmission HPDLCs have larger LC droplet regions and the interconnectivity between them make them appear more as a continuous layer rather than discrete droplet regions as shown in Figures 4.1(c) and 4.1(d).

A comparison of the grating spacing using a image analysis tool between the two types of imaging showed an average decrease of grating pitch by 18.6% for reflection HPDLC imaged in HV compared to VP. A decrease of grating spacing is observed for transmission HPDLCs by 17.5% for these two respective modes.

Overall reduction in the grating pitch contributed by conventional mode HV-SEM imaging is due to removal of LCs. Air replaces the voids created by LC elimination and the polymer matrix contracts around these regions reducing the average pitch of the grating.

Thus In this study two new SEM imaging techniques were used for the analysis

of the morphology of HPDLCs. The significant advantage of VPSEM and ESEM compared to conventional SEM is that they represent the true morphology profile without the need for LC removal or conductive coating. Comparing VPSEM images with HV-SEM images revealed the variation of the grating spacing for acrylate recipe HPDLCs after LC removal. Thus VPSEM was used for the first time to quantify the effect of LC removal on the true morphology of acrylate formulation based HPDLCs imaged and quantify the difference. ESEM has lower resolution compared to HV-SEM mode but can be used to analyze grating morphology of transmission mode HPDLCs with discernable contrast between the polymer and LC rich regions.

4.2 Electron Spin Resonance Analysis

This work is a result of collaboration with the Zannoni Liquid Crystal Group, Bologna, Italy and has resulted in a paper "Order and Dynamics Inside H-PDLC nanodroplets: an ESR Spin Probe Study" published in Journal of Physical Chemistry B

Investigating the birefringent LC orientation and behavior in confined polymer matrix of HPDLCs enables better understanding of its electro optic response. Nuclear magnetic resonance (NMR) spectroscopy has proved to be a suitable technique to study the orientation and dynamics of the LC inside the polymer matrix[56]. NMR was used for the first time to study the configuration of directors and dynamics in PDLCs by Golemme et al.[16, 57] Early NMR analysis on PDLC revealed a first order nematicisotropic (NI) phase transition for large droplets of LC. For droplets below the critical diameter of ≈35 nm, the NI phase transition showed a continuous variation from an ordered N phase to a weakly ordered I phase.[57] Iannacchione et al. performed deuteron NMR (DNMR) studies on HPDLCs and surmised that an

homeotropic LC configuration is present at the LC-polymer interface.[58] Their results indicated also a lower orientational order in the nanodroplets compared to the bulk LC. Vilfan et al.[33] used DNMR and dynamic light scattering (DLS) to study the orientational order and dynamics of a BL038-5CB LC mixture in a HPDLC. DLS showed that the onset of the N phase occurs at a temperature about 40 K lower, compared to the bulk, and takes place gradually. This is possibly due to a polydispersity of nanodroplet sizes having different compositions of non-liquid-crystalline ingredients. DNMR indicated that the structure of the director configuration is macroscopically isotropic and composed by a smaller fraction of a powder-like (low fluidity) nematic polydomain, with high local order, whereas the larger part of the LC is still in the I phase, even at room temperature. However, the bulk BL038 LC, at room temperature, shows a highly ordered N phase. The authors suggested that the locally ordered structure is located on the nanodroplet surface, since its contribution to the total DNMR spectrum is small and its translational diffusion is two orders of magnitude slower than that found in the bulk of the droplet cavity.

The lack of NMR results indicating, at least, a small fraction of nematic order along the NMR magnetic field is surprising and appears to be in contrast with the operating principle hypothesized for a HPDLC device, when a field is applied. To shed further light on the internal nematic director configuration of the nanodroplets, the local molecular order and dynamics, and to compare the observed behavior with that found in the bulk, ESR spin probe technique is performed here by doping the nematic BL038 LC with a stable nitroxide radical at a very low (10^4w/w) concentration and monitoring its spectra in different conditions. This technique, hitherto unused on HPDLC studies, allows the direct study of an actual device, due to its very high sensitivity.

Nuclear magnetic resonance (NMR) spectroscopy has been extensively used to

study the LC orientation inside confined LCs . Here a thorough investigation of the order and dynamics of the LC entrapped in nanodroplets of a reflection mode HPDLC is performed by using the electron spin resonance (ESR) spin probe technique for the first time. These results are then compared to the ESR spectroscopy findings performed on the bulk LC without the confinement effect of polymer.

The macroscopic configuration of the LC local nematic domain director and a model of the nanodroplet organization inside the layers are determined. The spectroscopic analysis was conducted at a series of temperatures ranging from the nematic to the isotropic phase of the LC.

In the ESR spin probe technique, the nematic LC is doped with a stable nitroxide radical and its spectra recorded at different temperatures and orientations of the sample cell in the ESR chamber.

From this technique we can infer that the orientational order of the elongated LC droplets is preserved at room temperature even in the presence of strong magnetic field. However at higher temperatures the larger sized droplets realign in the direction of the field and have a nematic monodomain configuration in the direction of the field whereas the smaller ones form an isotropic state most likely due to the confinement effects of the polymer and do not orient along the field.

The ESR spectra obtained is considered to be additive of the spectra of spin probes found in different regions of the LC droplets. The fractional contribution of each of these regions to the whole ESR spectrum is considered proportional to the amount of LC present in that region.

The HPDLC for analysis is fabricated using the acrylate recipe. For optimal results the recipe had 4% less LC compared to the standard formulation used for sample cell fabrication in this dissertation work shown in Table 3.1. The HPDLC were spaced 20 microns apart to enable good S/N ratio. The LC is doped with the

nitroxide spin probe 3β-DOXYL-5α-Cholestane(CSL) free radical explained in detail in Section 2.6.2

The ESR spectra was acquired by Bruker EMX spectrometer equipped with an ER 041XG microwave X-band (9.5 GHz) Gunn Diode bridge and a rectangular ER 4102 cavity hosted at Bologna University. The samples were thermostated with a nitrogen flux through a variable temperature unit Bruker B-VT 2000.

To study the effects due to annealing, spectra recorded from freshly prepared cells were compared with those recorded after either field cooling(FC) or zero field cooling (ZFC) the sample. FC was done by heating the sample at 353.2 K then slowly cooling it to 323.2 K, approximately 1 K/min, with the magnetic field set at 6300 G (the highest available on the ESR spectrometer) and then equilibrating for 20 min. In the ZFC the same heating process was followed by a cooling process in the absence of the magnetic field. Finally, the cell was brought to the required temperature for the measurement.

Final ESR spectra were recorded across the temperature interval 285.2-383.2 K which was chosen to be wide enough to study all the significant spectral changes exhibited by the system

To measure the ESR spectrum a capillary tube glued to the border of the cell is used to hold it in the chosen position and orientation within the ESR cavity (see experimental scheme in Figure 4.3(a) and (b)). The HPDLC test cell was placed in two types of orientations with respect to the magnetic field **B**.

The ESR cavity is cylindrical with 6mm diameter and length spanning 25mm. Cells longer than 25mm can be placed inside the test cavity. Rectangular HPDLC cells of dimension 5mmx 35mm were placed in the ESR cavity. This rectangular cell could be easily rotated around the X axis of the cavity but not around the Y axis due to the diameter limitations of the ESR cavity.

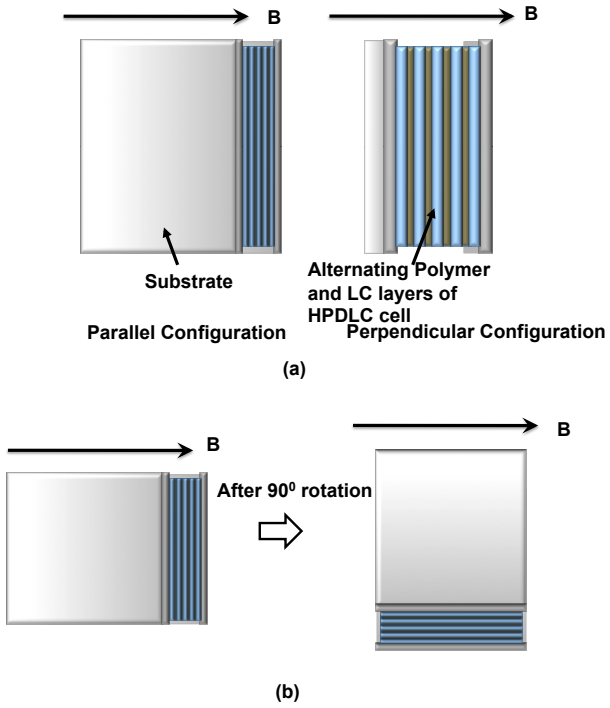

Figure 4.3: (a)Parallel and perpendicular configuration and (b) rotation around the Y axis

To find the director configuration from ESR spectra when the HPDLC cells are rotated along the Y axis smaller HPDLC cells of dimensions $5mm \times 5mm$ were used.

A typical rigid limit(RL) spectra was recorded at 153.2 K in the parallel geometry($\|$). The spectra recorded at 285.2 K after FC in $\|$ configuration had key features similar to the RL spectra, suggesting that part of the spectra was still in the rigid limit region. The spectra for ZFC was almost similar to FC spectra.

The spectra for the perpendicular configuration($\perp$) of the HPDLC cell was clearly different.

Here the spectra at 285.2 K could be consistently modeled by adopting a 2 site model consisting of RL and 2D components. The 2D model for best fit had its symmetry axis perpendicular to the LC/polymer layers and had two different components of $2D_{\|}$ and $2D_{\perp}$.

By adopting this model, a consistent temperature dependence of the best-fit parameters was recovered from the global analysis of the parallel and perpendicular spectra recorded in the temperature range 285.2 - 308.2 K, after FC in the parallel geometry. Results of the fits are presented in Figure 4.4(a) (experimental: dashed line, fits: solid line; $\|$ and $\perp$ geometry, respectively) and show excellent agreement with experiment.

In the interval 337.2 - 343.2 K, a more consistent behavior of the parameters was obtained by adopting a 3-site model of 3DPOP, 2D with low local $\langle P_2 \rangle$ and RL contribution. In the temperature interval 345.2 - 373.2 K, a consistent temperature dependence of the best-fit parameters was obtained by a model composed of N, ISO and RL contribution. Results of the fits are presented in Figure 4.4(b) (experimental: dashed line, fits: solid line). The lineshapes of the N contribution decrease at increasing temperature becoming barely visible at 373.2 K, where its fraction is estimated to be lower than 10 %. Above 373.2 K the sample is fully isotropic.

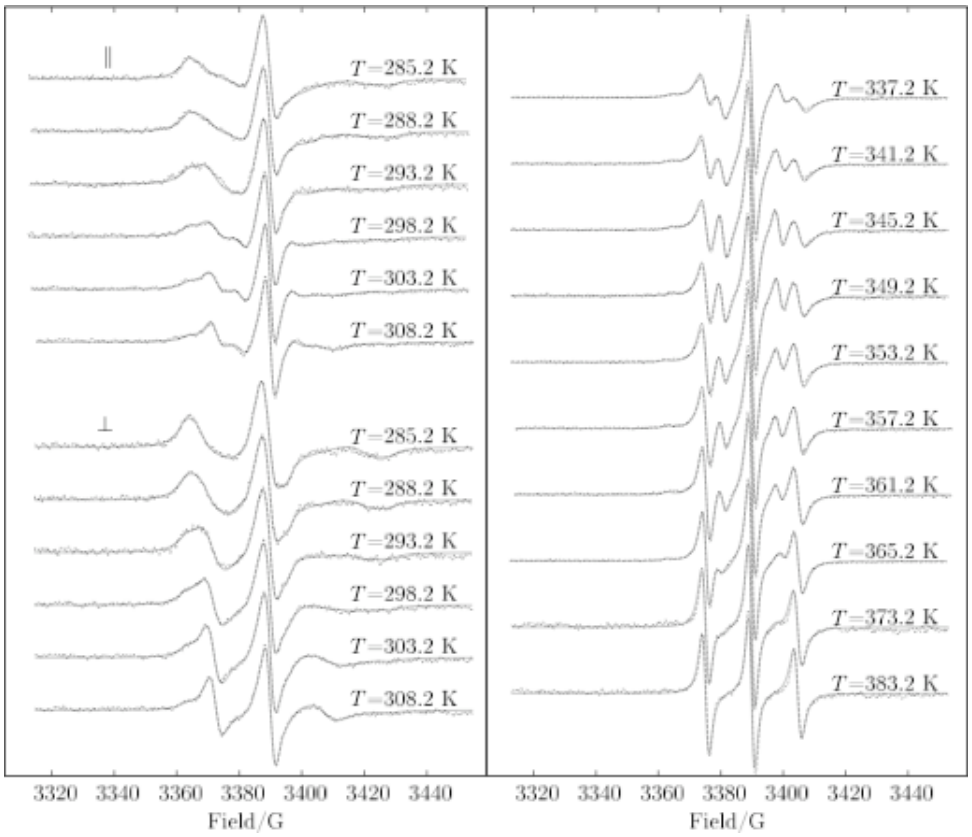

Figure 4.4: (a)Temperature dependence of typical ESR spectra (dashed line) and fits (solid line) to a 2- site model formed by RL + 2D spectral component. (b)Temperature dependence of typical ESR spectra (dashed line) of the H-PDLC cell recorded, after FC, in the parallel geometry and fits (solid line) to two different 3-site models (at 337.2 K and 343.2 K the spectral components are: RL + 3DPOP+2D; at 345.2373.2 K the components are: RL + N + ISO or to a single site, isotropic model (383.2 K).

The analysis of the FC spectra recorded in the temperature region 313.2 - 335.2 K proved to be the more difficult one, since all the spectral components described so far are present. A 3-site model composed by a RL, 2D and 3DPOP component was adopted which provided more stable best-fit parameters with a consistent temperature dependence.

In the temperature range 285.2 - 353.2 K, the spectra recorded in the parallel and perpendicular geometry could be globally fitted to the same values of the fractions of the components, local $\langle P_2 \rangle$ and dynamics, in the assumption that the ordered fraction did not realign along the magnetic field after the 90^0 rotation. Individual (not global) analysis of the spectra in the perpendicular geometry indeed indicated that the ordered fraction rotated as a whole with the sample, remaining essentially unaffected by the magnetic field up to 353.2 K. At 357.2 K, the best-fit local $\langle P_2 \rangle$ decreased from 0.60, before the rotation, to 0.31 after it and at higher temperatures the order of the N fraction was completely disrupted, becoming isotropic.

The fractional contribution of the ordered component was always larger after FC the sample compared to ZFC. In particular, the effects of annealing the cell in the magnetic field were more evident in an intermediate temperature region(310 - 350 K) and decreased at the lowest and highest temperatures.

In Figure 4.5 the local $\langle P_2 \rangle$ of the ordered components is compared to that observed in the bulk BL038 LC. Figure 4.6 shows the temperature dependence of the rotational diffusion tensor, $D_\perp$, of the various components together with a comparison to the bulk BL038 LC (values close to the T_c and in the bulk BL038 NI coexistence region, have been removed).

The effect of a 90^0 rotation of the square H-PDLC cells around the Y axis as shown in Figure 4.3(b) was studied at selected temperatures, after FC. In all cases, spectra recorded before and after the rotation (not shown) were identical and very

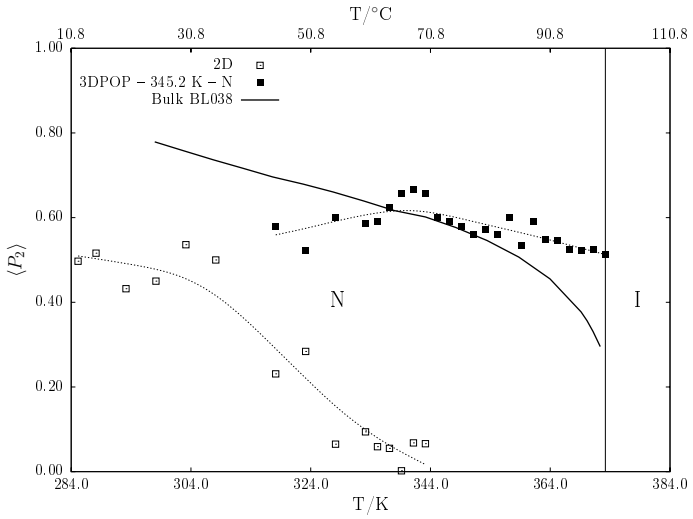

Figure 4.5: Temperature dependence of the local orientational order parameter,$\langle P_2 \rangle$, of the bidimensional (2D), three dimensional, partially ordered polydomain (3DPOP) and nematic monodomain (N) spectral components compared to the bulk BL038 liquid crystal. Thinner, dashed lines are a guide for the eye. The vertical line at 373.2 K indicates the bulk BL038 Tc.

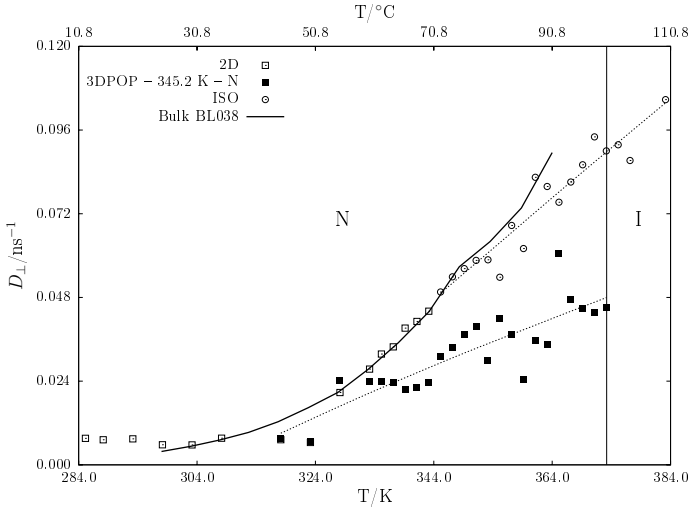

Figure 4.6: Temperature dependence of the tumbling diffusion coefficient, $D_\perp$, of the bidimensional (2D), three dimensional, partially ordered polydomain (3DPOP), nematic monodomain (N) and isotropic (ISO) spectral components compared to the bulk BL038 liquid crystal. Thinner, dashed lines are a guide for the eye. The vertical line at 373.2 K indicates the bulk BL038 T_c

similar, albeit relatively noisier, to those taken at the same temperature, after FC, from the rectangular cells.

The consistency of the ESR spectra of different replicas of the HPDLC sample cells, even when comparing replicas prepared from separate batches, indicated the high reproducibility of the process involving their manufacturing and photocuring.

The spectral analysis indicates that the director configuration inside the HPDLC nanodroplets is more complex than what has been previously found[56, **?**, 58, 33].

The clear difference observed between spectra recorded in the parallel and the perpendicular geometry (rotation of the sample cell around the laboratory X axis, see Figure 4.3), in the temperature range 285.2-373.2 K, unambiguously indicated the presence of a macroscopically anisotropic contribution. At 285.2 K the FC, parallel spectrum was only slightly different from that recorded after ZFC or that of a freshly prepared cell. In an intermediate temperature range (310-350 K), the differences between FC and ZFC or the fresh cell were the largest and tended to decrease again at higher temperatures. This behavior suggests a model where, at the lowest temperatures, the director configuration is governed mainly by the confinement and is, therefore, less sensitive to the annealing, whereas at higher temperatures, due to increased mobility, a fraction of the molecules will align along the magnetic field without the need of the annealing, to form a 3DPOP or a N. In the intermediate temperature region, between the confinement induced and the field-induced director configuration, FC the sample produces the largest effects.

The nature of the suggested confinement-induced director configuration can be further understood by considering that the ordered fraction, observed in the spectra recorded in the parallel geometry, after FC also in the parallel geometry, did not realign along the magnetic field when the cell was rotated to the perpendicular geometry, but instead either rotated as a whole with the sample (up to 353.2 K), remaining

essentially unaffected by the field, or it was disrupted by the field, becoming isotropic (above 357.2 K). This indicated that the ESR magnetic field is not able to reorient the local nematic directors around the X axis, to induce an alignment perpendicular to the layers.

Spectra of the square H-PDLC cells, recorded at selected temperatures, after FC, before and after a 90^0 rotation around an axis perpendicular to the layers (Y axis, Figure 4.3(b)) were identical in all cases. In the temperature interval 285.2-308.2 K, this result is in agreement with the expected overall bidimensional (radial) symmetry around the Y axis of the director distribution corresponding to the best-fit spectral components (RL + 2D). The onset of a 3DPOP and then of a N component, detected in the temperature interval 313.2373.2 K, changes a fraction of the 2D distribution into a new one where the director is either partially (3DPOP) or fully (N) aligned along the magnetic field. This change must involve a reorientation of the local directors at least around the Y axis, breaking in this way the 2D symmetry. The lack of change in the spectra, when the cell is rotated around the Y axis, confirms that a reorientation of the LC local directors around this axis can indeed occur.

Models for the director configuration inside the nanodroplets Throughout the modeling, no assumptions about the preferred orientation of the LC at the nanodroplet surface (e.g. homogeneous or homeotropic) was made since (i) this information is not directly achievable from the analysis of the ESR spectra and (ii) both orientations were compatible with the final analysis. The only assumption, in this respect, is that the RL contribution is due to CSL located in the fraction of the LC molecules close to the surface whereas the interior of the nanodroplets shows a larger mobility. It is also important to recognize that the ESR data do not reveal whether the different environments, where the CSL can be located, coexist within each droplet. From this point of view, there might be nanodroplets entirely RL, even

if this seems rather unlikely, and other nanodroplets fully ISO or 3DPOP. We can instead examine the various arrangements of the different domains inside the same droplet.

In the model here, an equilibrium between LC molecules forming a layer on the droplet surface, with a very limited mobility, and molecules in the remaining volume, the droplet cavity, with a faster dynamics is postulated. As the temperature increases, less and less molecules remain frozen on the surface layer, thus increasing the size of the cavity. At each temperature, the observed spectral components are the result of a different equilibrium between the surface layer and two molecular environments, determined by a critical dimension of the droplet cavity. Above this dimension, the constraints induced by the surface layer to the LC structure in the cavity are relatively small, the local $\langle P_2 \rangle$ is thus bulk like and, upon FC, a 3DPOP or a N, oriented along the magnetic field, can be formed. Below this dimension, the surface induced distortions lower the local $\langle P_2 \rangle$ and the T_c, compared to the bulk. The effects of FC are very similar to ZFC, indicating that the director configuration is mainly dictated by the confinement and not by the magnetic field. As the temperature increases, a larger fraction of nanodroplets reaches the T_c thus becoming isotropic.

Possible microscopic director configurations, typically suggested for this kind of confined systems are radial and bipolar[59].

To determine which microscopic director configuration is compatible with our results, we need a model to relate the microscopic configuration to the macroscopic one. In the assumption that the microscopic configuration is determined, at least to some extent, by the confinement, this means to establish a model for the organization of the nanodroplets. Therefore, our further discussion hinges on the assumption, based on the inspection of SEM images, that the shape of the nanodroplets is, on the average, elongated and has the long axis preferentially oriented parallel to the layers.

Model for the nanodroplet distribution The observed macroscopic 2D director distribution could stem from (i) a director configuration with a 2D (radial) symmetry inside each nanodroplet or could be the result of (ii) a 2D distribution of the elongated nanodroplets having inside a uniaxial director configuration. We found that across the whole temperature range 313.2-373.2 K, when the orientational director distribution changes from 2D to 3DPOP and then N, the ESR magnetic field is able to reorient the LC local directors around the Y axis but not around the X axis. This would suggest that a 2D symmetry does not depend from the temperature but is present in the very structure of the H-PDLC material and would be compatible with the second option above.

In particular, a uniaxial LC director configuration inside the elongated nanodroplets would be compatible with the macroscopic 2D distribution, observed at lower temperature, in the assumption that the axis of the director configuration is parallel to the nanodroplet long axis and that this axis is, in turn, randomly oriented in a plane parallel to the layers. Furthermore, it appears reasonable that, as the molecular mobility increases, at higher temperature, this uniaxial configuration can be more easily aligned along the magnetic field when this is parallel to the layers, thus forming the observed macroscopic monodomain or quasi-monodomain (3DPOP).

Given the nature of the ESR experiment, a more detailed description of the director field of this uniaxial configuration is not possible. Figure 4.7 shows example of bipolar director configuration often found in literature as the most likely orientation of the droplets.

A radial director configuration with a defect line along the droplet axis would not be compatible with the findings here since the resulting macroscopic director distribution would have a 2D symmetry only if all the nanodroplets were elongated perpendicularly to the layers, but clearly this is not observed in any of the SEM

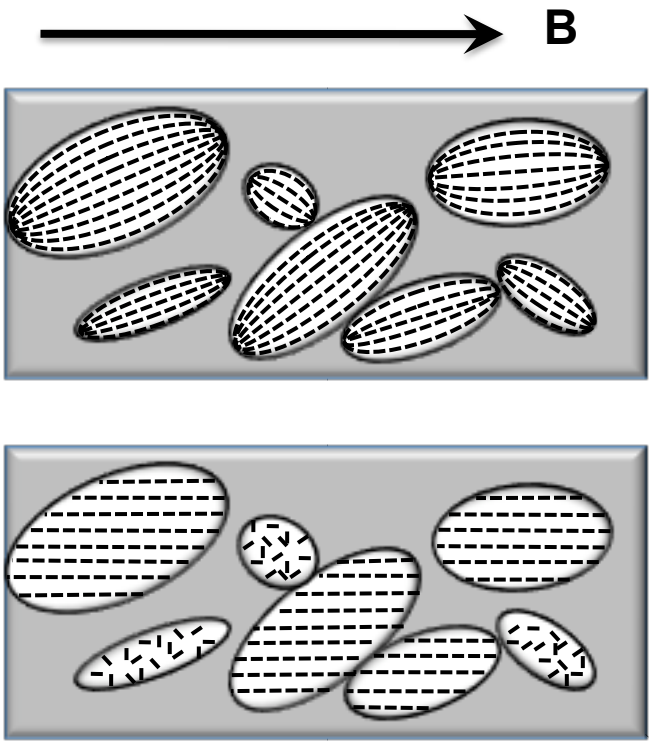

Figure 4.7: Inplane view of a HPDLC's LC droplet layer showing effect of temperature in the presence of a magnetic field.(a) At lower temperatures, (285.2-308.2 K) due to predominant effect of confinement in droplets, bipolar orientation is seen and (b) at higher temperatures (345.2-373.2 K) larger sized droplets tend to align in the direction of the field and smaller ones become isotropic

images. The model of the droplet orientation is shown in Figure 4.7.

The next chapter details the Berreman matrix technique to analyze the HPDLC gratings and incorporate the parameters obtained from the characterization studies to examine the grating behavior.

5. Light Wave Propagation in Periodically Stratified Systems

HPDLC technology used for multiple electro-optic components such as lenses, filters and switches have found wide-ranging application in the design of integrated optics. Some of the other currently evolving applications of HPDLCs are tunable photonic crystals, controllable photomasks and dynamic beam steering devices.

Efforts have been made to broaden the interaction wavelength using various techniques. The peak interacting wavelengths of the HPDLCs can be broadened to reflect multiple wavelengths or have a continuous broadened reflection peak using methods such as changing material composition, stacking and multiplexing techniques.

In this chapter we review some of the techniques used to predict the optical output lineshapes of HPDLC holograms.

To analyze the interaction of light with diffraction gratings and predict the reflected and transmitted output we start with summarizing Maxwell's equations and wave equations. Maxwell's equations are spatial and temporal partial differential equations, depicting the properties of electromagnetic fields. The notation used here are

$\mathbf{k}$	Propagation constant	$\mathbf{E}$	Electric field vector	$\mathbf{H}$	Magnetic field vector
μ_0	Permeability in vacuum	ε_0	Permittivity of vacuum	$\mathbf{D}$	Electric displacement
ε_r	Relative permittivity	χ	Electric susceptibility	μ_r	Relative permeability

In a nonmagnetic, nonconducting and uncharged medium the standard form of

Maxwell's equations are written as[60, 61, 27]

$$\nabla \times \mathbf{E} = -\mu_0 \frac{\partial \mathbf{H}}{\partial t} \tag{5.1}$$

$$\nabla \times \mathbf{H} = \varepsilon_0 \varepsilon_r \frac{\partial \mathbf{E}}{\partial t} \tag{5.2}$$

$$\nabla \cdot \varepsilon_0 \varepsilon_r \mathbf{E} = 0 \tag{5.3}$$

$$\nabla \cdot \mathbf{H} = 0 \tag{5.4}$$

For an electrically isotropic medium the relative permittivity ε_r is given by $1+\chi$. For an electrically anisotropic medium the relative permittivity $\varepsilon_{\mathbf{r}}$ is a symmetric tensor.

Considering an electrically isotropic medium and solving the Equations 5.1-5.4 for electric field vectors $\mathbf{E}$ we can write the wave equation as [61]

$$\nabla^2 \mathbf{E} - \mu_0 \varepsilon_0 \varepsilon_r \frac{\partial^2 \mathbf{E}}{\partial t^2} = 0 \tag{5.5}$$

Solution to this differential wave equation is a plane harmonic wave equation represented as

$$\mathbf{E} = \mathbf{E_0} exp\left[i(\omega t - \mathbf{k} \cdot \mathbf{r})\right] \tag{5.6}$$

where $\mathbf{E_0}$ is the amplitude vector, $\omega = 2\pi f$ is the angular frequency (f is the frequency of the wave), t is time, $\mathbf{k}$ is the propagation wave vector with magnitude $2\pi/\lambda$ (λ is the wavelength in the medium) and $\mathbf{r}$ is the displacement vector from the origin. The propagation velocity of this electromagnetic plane wave in a medium of refractive index n is

$$v = \frac{c}{n} = \frac{1}{\sqrt{\mu_0 \varepsilon_0 \varepsilon_r}}$$

where c is the propagation velocity in vacuum. Taking time differential of the complex

solution of the plane harmonic wave solutions of Equation 5.6, the wave Equation 5.5 can be rewritten as

$$\left(\nabla^2 + \frac{\omega^2}{c^2} n^2\right) \mathbf{E} \;=\; 0 \tag{5.7}$$

These equations are used for analyzing the diffraction efficiency of gratings.

The diffraction grating structure can be classified as an amplitude or phase grating, based on the amplitude or phase modulation of the interacting light. In the amplitude grating, variation of absorption coefficient results in the formation of diffraction grating. Modulation of optical thickness or refractive index, changes the phase of interacting light forming a phase grating. However this classification is ambiguous because absorption modulation or loss in a medium tends to change the real part of the refractive index. Also the phase grating tends to vary the amplitude of the light. For our purpose we will study the optical interaction of transparent lossless phase gratings.

The phase grating can be further classified to operate in three regimes namely Raman-Nath, Bragg regime and form birefringence.

In the form birefringence regime interaction of grating with its pitch much less than optical wavelength is considered[62]. The gratings display birefringence even in isotropic medium due to periodic structure. These structures have negative refractive index and will not be considered in this dissertation.

Raman-Nath and Bragg regime of operation can be distinguished by the number of diffraction orders. Raman-Nath regime has multiple diffraction order while a grating in a Bragg regime usually has 0^{th} and 1^{st} order diffraction. Figure 5.1(a) is a schematic representation of Raman-Nath grating. Figure 5.1(b) and Figure 5.2 is the schematic representation of transmission and reflection Bragg grating. They vary chiefly in the direction of interaction of the incident wavelength propagation vector with the

grating. Here L is the length of the grating and Λ is the grating pitch.

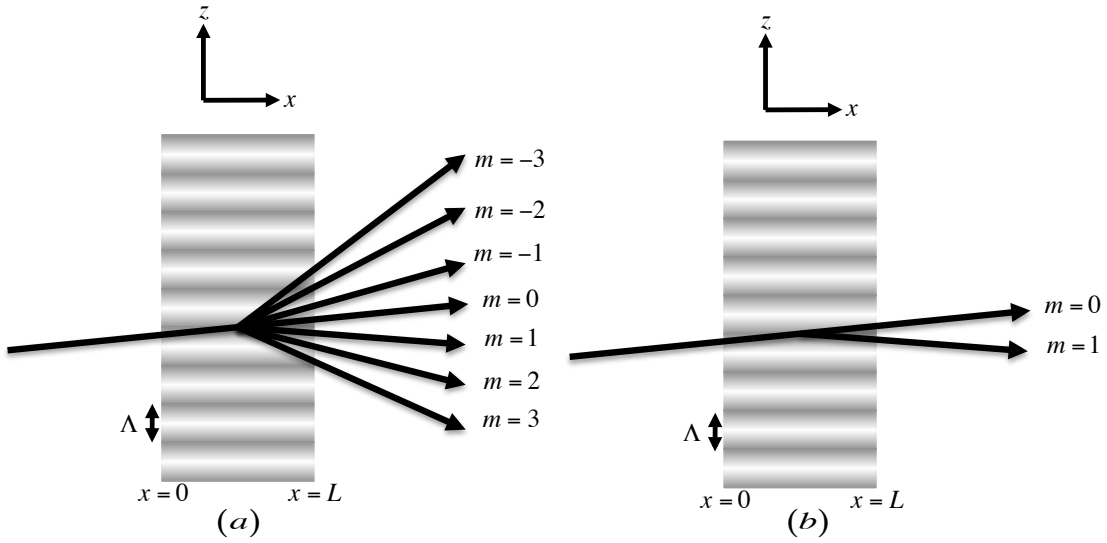

Figure 5.1: (a)Raman Nath and (b) Transmission Bragg grating

The Cook and Klien parameter also known as the Q parameter is extensively used in literature[63, 64] to segregate the Raman-Nath and Bragg regimes. The Q parameter is defined as

$$Q = \frac{2\pi\lambda L}{n\Lambda^2}$$

where λ is the incident wavelength,L is the film thickness, n is the average refractive index and Λ is the grating pitch. The regime where $Q < 1$ is defined as the Raman-Nath regime. When $Q > 1$ is defined as the Bragg regime and the grating is called the Bragg grating.

However Raman-Nath grating behavior is observed at high values of Q and cannot be completely relied upon, for a clear cut differentiation in the regimes as explained by Moharam et al. [63, 65]

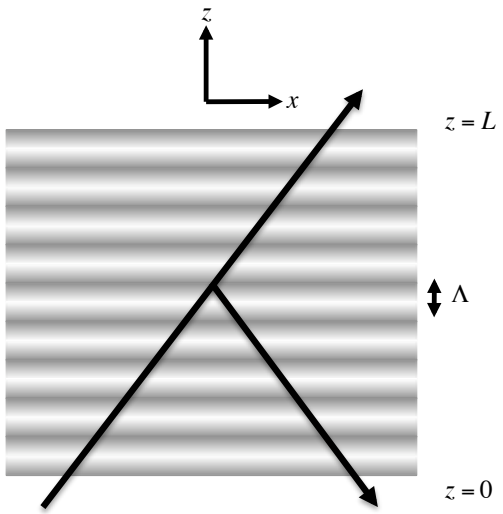

Figure 5.2: Reflection Bragg grating

Raman-Nath and coupled wave equations have been used to theoretically predict the output of the Raman-Nath and Bragg gratings respectively. These phase gratings can be assumed to have sinusoidally varying refractive index represented in Equation 2.14

A brief overview of calculating the diffraction efficiency of Raman Nath and Bragg grating is indicated in the following sections. This is followed by matrix method of analyzing the Bragg grating and determination of parameters for simulation.

5.0.1 Raman-Nath Theory*

Consider an optical field wave of amplitude $\mathbf{E_0}$ incident on a Raman-Nath(RN) sinusoidal phase grating as shown in Figure 5.1(a) with its propagation vector $\mathbf{k}$ parallel to the xz plane in a 3 dimensional xyz cartesian coordinate system. $\mathbf{K}$ is the grating wave vector along the z direction. Let the field be s polarized parallel to the y direction. Thus xz plane is the plane of incidence formed by $\mathbf{k}$ and $\mathbf{K}$ and

*adapted from the book Introduction to Photorefractive Nonlinear Optics[27]

the propagation vector of the transmitted field lies on this plane. The incident field on the RN phase grating from Equation 5.6 and transmitted field through it can be written as

$$\mathbf{E_i} = \mathbf{E_0} exp\left[i(\omega t - \mathbf{k}\cdot\mathbf{r})\right] \tag{5.8}$$

$$\mathbf{E_t} = \mathbf{E_0} exp\left[i(\omega t - \mathbf{k}\cdot\mathbf{r}) - i\delta\cos\left(\mathbf{K}\cdot\mathbf{r}\right)\right] \tag{5.9}$$

where δ termed as the modulation index is

$$\delta = \frac{\omega n_1 L}{c\cos\theta}$$

Here θ is the angle of incidence between the $\mathbf{k}$ vector and x axis. The Bessel function identity

$$exp\left(-i\delta\cos x\right) = \sum_{m=-\infty}^{m=\infty} J_m(\delta)(-i)^m exp\left(-imx\right)$$

is substituted into the transmitted field and this field is rewritten as

$$E_t = E_0 \sum_{m=-\infty}^{m=\infty} J_m(\delta)(-i)^m exp\left[i\left(\omega t - \mathbf{k}_m\cdot\mathbf{r}\right)\right] \tag{5.10}$$

where $\mathbf{k}_m$ is the wave vector and $J_m(\delta)(-i)^m$ is the amplitude of the m^{th} order diffracted wave. From the Equation 5.10 we can infer that transmitted field is equal to a sum of diffracted plane waves of order m. Also from the law of conservation of energy, the sum of the intensities of all the diffracted waves of order m is equal to the incident intensity. In the Equation 5.9, $\delta\cos\left(\mathbf{K}\cdot\mathbf{r}\right)$ is the phase change component of the transmitted wave, resulting from traversing the phase grating. The diffraction

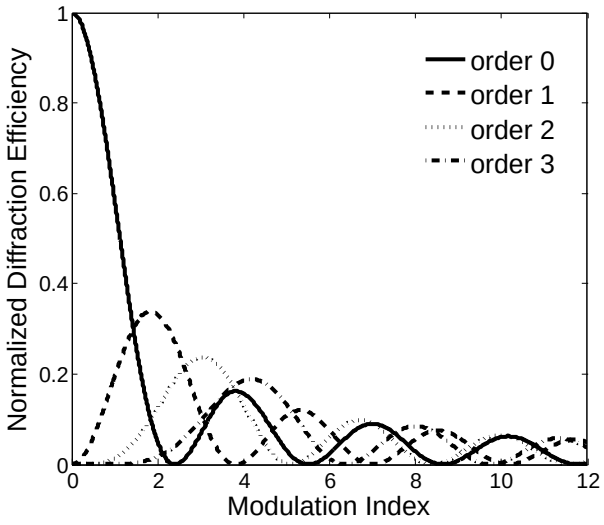

Figure 5.3: Diffraction Efficiency as a function of modulation index $\delta = \frac{\omega n_1 L}{c \cos\theta}$

efficiency of a RN grating of order m is determined from the Equation 5.10 as

$$\eta_{\mathbf{m}} = J_m^2(\delta) = J_m^2\left(\frac{2\pi L n_1}{\lambda \cos\theta}\right) \tag{5.11}$$

Figure 5.3 plots the diffraction efficiency as a function of the modulation index as shown. Here the diffraction efficiency is calculated for 0^{th}, 1^{st}, 2^{nd} and 3^{rd} order.

5.0.2 Coupled Wave Theory*

In the coupled wave theory approach, developed by Kogelnik in 1969 the dielectric medium of the grating is assumed to be isotropic and the refractive index varies in a sinusoidal fashion[64]. The diffracted beam is coupled to the incident beam, giving an expression for the energy transfer efficiency. Coupled mode theory predicts the diffraction efficiency of gratings in the Bragg regime which by definition have only one diffraction order. Figure 5.1(b) shows a transmission grating and Figure 5.2 shows reflection grating in Bragg regime. The coupled mode analysis treatment varies for

*adapted from the book Introduction to Photorefractive Nonlinear Optics[27]

these two modes. Depending on whether a transmission or reflection grating is considered the amplitudes of incident and diffracted wavelengths are dependent on different interaction parameters. Here we will briefly review both these techniques. Consider the Bragg gratings shown in Figure 5.1(b) and Figure 5.2 having a sinusoidally varying refractive index denoted by Equation 2.14. Here a transverse electric(TE) or s-polarized electric field is considered which is parallel to the y direction incident on the two types of Bragg gratings of length L. The incident wave propagation vector $\mathbf{k_1}$ parallel to the xz plane. The amplitudes of the incident and the diffracted waves are represented by A_1 and A_2 respectively. $\mathbf{k_2}$ is the propagation vector of the diffracted wave. Thus xz plane is the plane of incidence formed by $\mathbf{k_1}$ and grating wave vector $\mathbf{K}$(along z direction) and $\mathbf{k_2}$ lies on this plane.

The electric field of the incident and diffracted wave can thus be written as

$$E = A_1 exp\left[i\left(\omega t - \alpha_1 x - \beta_1 z\right)\right] + A_2 exp\left[i\left(\omega t - \alpha_2 x - \beta_2 z\right)\right] \tag{5.12}$$

where ω is the angular frequency of the fields, β_1 and β_2 are the z component and α_1 and α_2 are the x component of the propagation vectors $\mathbf{k_1}$ and $\mathbf{k_2}$ respectively represented by

$$\alpha_1 = \frac{2\pi}{\lambda} n_0 \cos\theta_1 \quad \alpha_2 = \frac{2\pi}{\lambda} n_0 \cos\theta_2 \quad \beta_1 = \frac{2\pi}{\lambda} n_0 \sin\theta_1 \quad \beta_2 = \frac{2\pi}{\lambda} n_0 \sin\theta_2 \tag{5.13}$$

where θ_1 and θ_2 are the incident and diffracted angles.

Bragg Transmission Gratings

Reconsider the transmission grating in the Bragg regime shown in Figure 5.1(b) having a sinusoidally varying refractive index denoted by Equation 2.14. The electric field of the incident and diffracted field is represented by Equation 5.12. To satisfy

the Bragg condition for well coupled transmission grating considered the angle between the incident beam and x axis should be very small. For simplification of the analysis we assume that the grating is infinite along the z direction and the amplitude of the incident and diffracted wavefront are dependent on the x components. By substituting the above field Equation 5.12 into the wave Equation 5.7 and mathematical manipulation of the resultant equations we can derive the coupled equations for transmission gratings denoted as

$$\frac{d}{dx}A_1 = -i\kappa_{12}A_2 e^{-i\Delta\alpha x}, \qquad \frac{d}{dx}A_2 = -i\kappa_{21}A_1 e^{i\Delta\alpha x} \tag{5.14}$$

where

$$\kappa_{12} = \frac{\pi n_1}{\lambda\cos\theta_1}, \quad \kappa_{21} = \frac{\pi n_1}{\lambda\cos\theta_2} \quad \text{and} \quad \Delta\alpha = \alpha_2 - \alpha_1 = \frac{2\pi}{\lambda}n_0\left(\cos\theta_2 - \cos\theta_1\right) \tag{5.15}$$

as long as $\beta_2 = \beta_1 \pm K$ is satisfied. Here θ_1 and θ_2 are related by the equation

$$\sin\theta_2 = \sin\theta_1 \pm \frac{\lambda}{n_0\Lambda} \tag{5.16}$$

We consider the coupled wave equations for the cases of perfect phase match and phase mismatch when $\Delta\alpha = 0$ and $\Delta\alpha \neq 0$ respectively

Case 1: $\Delta\alpha = 0$ For a perfectly phase matched case we have $\cos\theta_2 = \cos\theta_1$. This implies that $\theta_2 = -\theta_1$. Substituting this condition in Equation 5.16 we can write the Bragg angle of incidence as

$$\theta_B = \sin^{-1}\left(\frac{\lambda}{2n_0\Lambda}\right) \tag{5.17}$$

For this incident angle the coupled wave Equation 5.14 can be rewritten as

$$\frac{d}{dx}A_1 = -i\kappa A_2, \quad \frac{d}{dx}A_2 = -i\kappa A_1 \tag{5.18}$$

where

$$\kappa = \frac{\pi n_1}{\lambda \cos\theta_B} \tag{5.19}$$

Finding the solutions $A_1(x)$ and $A_2(x)$ of the coupled wave equations we can compute the diffraction efficiency. Diffraction efficiency is the ratio of the transmitted beam intensity at $x = L$ to the incident beam intensity at $x = 0$ given as

$$\eta = \frac{I_{diffracted}}{I_{incident}} = \frac{|A_2(L)|^2}{|A_1(0)|^2} = \sin^2 \kappa L \tag{5.20}$$

Case 2: $\Delta\alpha \neq 0$ In the phase mismatched case the incident angle is deviated from the Bragg angle by a small quantity represented by $\Delta\theta$ in this case. The incident angle can be rewritten as $\theta_1 = -\theta_B + \Delta\theta$. Substituting in Equation 5.16 and satisfying the Bragg condition, θ_2 can be determined where $\theta_2 = \theta_B + \Delta\theta$. The momentum mismatch Equation 5.15 for $\Delta\alpha$ can be rewritten by substituting the values of θ_1 and θ_2 as

$$\Delta\alpha = -2k\Delta\theta \sin\theta_B \tag{5.21}$$

Solving the coupled Equation 5.14 and substituting $\Delta\alpha$ value we can determine the solution $A_1(x)$ and $A_2(x)$. The diffraction efficiency for a grating with momentum mismatch is computed as

$$\eta = \frac{|A_2(L)|^2 \cos\theta_2}{|A_1(0)|^2 \cos\theta_1} = \frac{\kappa^2}{\kappa^2 + \left(\frac{\Delta\alpha}{2}\right)^2} \sin^2 \left\{ \kappa L \left[1 + \left(\frac{\Delta\alpha}{2\kappa} \right)^2 \right]^{1/2} \right\} \tag{5.22}$$

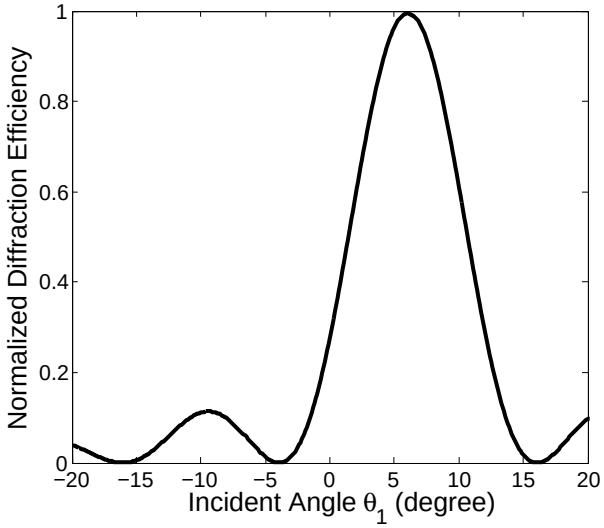

Figure 5.4: Diffraction Efficiency as a function of incident angle θ_1

Figure 5.4 plots the diffraction efficiency as a function of variation of the incident angle θ_1 The Bragg grating angle should be small for good coupling. The incident wavelength and the grating pitch Λ are considered accordingly. Thus considering $\Lambda = 2\mu m$ with incident wavelength of He-Ne of 633nm, $n_0 = 1.5, n_1 = 0.03$ we get $\theta_B = 6$. Plotting these values for varying incident angles between -20 to 20 degree we get the a plot as shown in Figure 5.4 . From the plot we can note that the maximum diffraction efficiency is at the Bragg angle of 6^0.

The same coupled wave theoretical treatment can be applied for the transverse magnetic (TM) or p-polarized incident field parallel to the xz plane by substituting the coupling coefficient κ with κ_p. For the grating considered in Figure 5.1(b) the coupling coefficient κ_p is determined as[64]

$$\kappa_p = -\kappa \cos(2\theta_B) \tag{5.23}$$

Here for the trivial case when the Bragg angle $\theta_B = 45°$, it corresponds to the Brew-

sters angle and diffraction angle of 90° resulting in κ_p and the diffraction efficiency η_p to be 0.

Bragg Reflection Gratings

Consider the reflection grating in Bragg regime as shown in Figure 5.2 with sinusoidally varying refractive index medium represented by Equation 2.14. The electric field of the incident and diffracted field(reflected in this case) is denoted by Equation 5.12.

Applying boundary conditions $\alpha_1 = \alpha_2$ and field amplitudes A_1 and A_2 are functions of z only. Also since $\alpha_1 = \alpha_2$, $\theta_1 = -\theta_2$ from the Equation 5.13. We can now rewrite field Equations 5.12 for s-polarized waves as

$$E = \{A_1(z)\, exp\,[i(\omega t - \beta_1 z)] + A_2(z)\, exp\,[i(\omega t - \beta_2 z)]\}\, exp\,(-i\alpha x) \tag{5.24}$$

This equation is substituted in the wave Equation 5.7. By mathematically manipulating the resulting equation the coupled wave equations can be written as

$$\frac{d}{dz}A_1 = -i\kappa A_2 e^{-i\Delta\beta z}, \quad \frac{d}{dz}A_2 = i\kappa A_1 e^{i\Delta\beta z} \tag{5.25}$$

where

$$\Delta\beta = \beta_2 - \beta_1 \pm K \;\text{ and }\; \kappa = \frac{\pi n_1}{\lambda \sin\theta_1} = \frac{2\pi n_1 n_0 \Lambda}{\lambda^2}$$

The coupled wave equation are solved for 2 cases of phase match ($\Delta\beta = 0$) and phase mismatch ($\Delta\beta \neq 0$) respectively.

Case 1: $\Delta\beta = 0$ For this phase matched condition the coupled wave Equation 5.25 can be integrated and solved to obtain

$$A_1(z) = A_1(0)\frac{\cosh\kappa(z-L)}{\cosh\kappa L}, A_2(z) = iA_2(0)\frac{\sinh\kappa(z-L)}{\cosh\kappa L} \tag{5.26}$$

The diffraction efficiency η is defined as

$$\eta = \frac{|A_2(z=0)|^2}{|A_1(z=0)|^2} = \tanh^2(\kappa L) \tag{5.27}$$

Case 2: $\Delta\beta \neq 0$ The efficiency obtained from the solving the coupling wave Equation 5.25 with boundary condition $A_2(L) = 0$ is

$$\eta = \frac{|\kappa|^2 \sinh^2 sL}{s^2\cosh^2 sL + \left(\frac{\Delta\beta}{2}\right)^2 \sinh^2 sL} \tag{5.28}$$

where

$$s = \sqrt{|k|^2 - \left(\frac{\Delta\beta}{2}\right)^2},$$
$$\Delta\beta = \frac{2\pi}{\Lambda} - \frac{4\pi}{\Lambda}n_0\sin\theta_1$$

In Figure 5.5 we plot the Bragg reflection response for different wavelengths to a grating with phase matched system($\Delta\beta = 0$). Consider a HPDLC Bragg grating with n_0=1.5, normal incidence and index modulation of $n_1 = 0.01, 0.03, 0.05, 0.07$, $\Lambda = 183nm$. From Bragg grating equation we have the peak reflective wavelength at 550nm.

This theoretical treatment of coupled wave equation for Bragg reflection gratings is developed here for s-polarized waves. For p-polarized incident electric field the diffraction efficiency is determined by replacing κ by κ_p as represented by Equa-

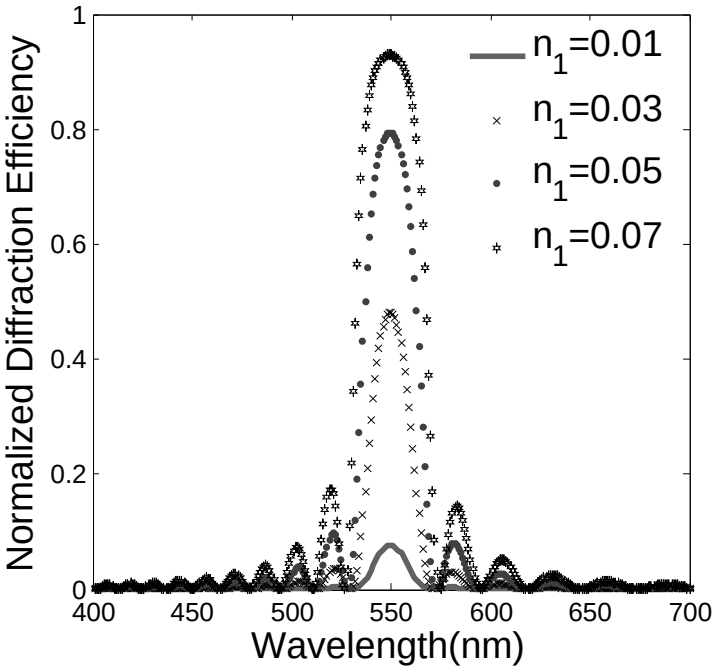

Figure 5.5: Simulated effect of refractive index modulation parameter n_1 on the optical output response of Bragg gratings using coupled wave theory

tion 5.23. Since the coupling coefficient κ_p of p-polarized wave is a fraction of the s-polarized wave, the diffraction efficiency of p-polarized wave is less than or equal to that of s-polarized wave depending on the Bragg angle θ_B. However experimentally for certain types of acrylate recipe based HPDLCs the DE for p-polarized incident have been observed to be much higher than DE for s-polarized beams[54]. For thiolene monomer based formulation the DE for both types of polarization have been observed to be similar[46]

5.0.3 Matrix Method

Different matrix approaches can also be used to deduce the output of the HPDLCs by considering Maxwells equations in a matrix form. A 2×2 matrix approach has 2 element field vectors. In a 4×4 matrix approach there are 4 field vectors corresponding

to electric and magnetic fields for 2 independent polarization modes. The transfer matrix method employed is explained more in detail in the next section.

5.0.4 2×2 Matrix Formulation

There are two types of 2×2 transfer matrix approaches typically used. In these techniques the optical response of the individual layer of LCs and polymers are analyzed and then the final response is modeled by considering the layers as a stack. Here all the layers are assumed to be isotropic and homogeneous. The layers are denoted by the numbers $1, 2, 3, \cdots n$. One of the two polarization modes of incident radiation is considered for computation.

In the first technique the electric field and magnetic field transmitted through each layer is related to the polarized incident field by a 2×2 characteristic matrix. For a system of n layers this is computed as[66]

$$\begin{bmatrix} E_1 \\ H_1 \end{bmatrix} = M \begin{bmatrix} E_{n+1} \\ H_{n+1} \end{bmatrix} = \begin{bmatrix} m_{11} & m_{12} \\ m_{21} & m_{22} \end{bmatrix} \begin{bmatrix} E_{n+1} \\ H_{n+1} \end{bmatrix} \tag{5.29}$$

where the 2×2 matrix M can be represented as

$$M = M_1 M_2 M_3 \cdots M_n$$

Here $M_1, M_2 \cdots M_n$ are the characteristic matrix of each of the layers and are a function of its refractive index and thickness.

In the second type of technique only the electric field is determined for forward and backward moving electric field radiation instead of the resultant electric and

magnetic field computation of the first method. This is represented as[67]

$$\begin{bmatrix} E_i \\ E_r \end{bmatrix} = P \begin{bmatrix} E_t \\ 0 \end{bmatrix} = \begin{bmatrix} p_1 & p_3 \\ p_2 & p_4 \end{bmatrix} \begin{bmatrix} E_t \\ 0 \end{bmatrix} \tag{5.30}$$

Here E_i, E_r and E_t are the incident, reflected and transmitted radiation respectively. The matrix P is represented by

$$P = I_{01}\Phi_1 I_{12}\Phi_{02}\cdots\Phi_n I_{ns}$$

Here I_{ij} matrix represents the propagation between layer i and j and T_j denotes field propagation through the j^{th} layer.

The reflectance and transmitted intensity are thus computed from the transmitted field using transfer matrix approach.

5.0.5 Berreman Theory*

There are different 4×4 matrix techniques to compute the electric fields through layered media[69, 70, 71]. Berreman 4×4[72] technique is used to model the output wavelength intensity in this dissertation for HPDLCs. The characteristic matrix for each of the LC and polymer layers beginning from one end of the stack is computed and then the field vectors are propagated to the other end of the stack by taking the product of the individual layer transfer matrices.

Berreman 4×4 method is used to denote wave propagation equation in both isotropic and anisotropic medium. They are the result of mathematical manipulation of the Maxwell's equation written in matrix form.

Equation 5.1 and 5.2 relate the electric and magnetic fields. The spatial variation in one field state corresponds to the temporal change in the other. In cartesian coor-

*adapted from the book Birefringent Thin Films and Polarizing Elements[68]

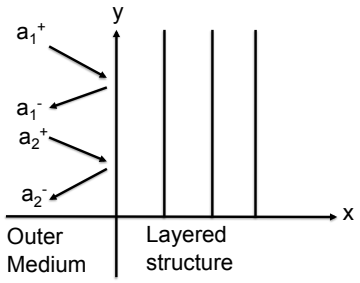

Figure 5.6: Convention used in the layered structure

dinate system each equation can be expanded into 3 equations for all permutations, by writing it out in terms of x, y and z coordinates. Thus the Maxwell's equation is written in 6×6 matrix form. A plane propagating wave in the xy plane incident on layered structure is considered here where the direction of propagation is x. The relative permittivity $\hat{\varepsilon}$ for the plane of propagation is represented as

$$\hat{\varepsilon} = \begin{bmatrix} \varepsilon_{xx} & \varepsilon_{xy} & \varepsilon_{xz} \\ \varepsilon_{xy} & \varepsilon_{yy} & \varepsilon_{yz} \\ \varepsilon_{xz} & \varepsilon_{yz} & \varepsilon_{zz} \end{bmatrix}$$

Here 2 of the field elements along the propagation direction namely E_x and H_x can be eliminated since they are constant.

The direction of the remnant 4 fields are represented in terms of propagation direction angle θ and refractive index n. By mathematical manipulation the 4 Maxwell

equations can now be written in the eigen form as

$$\begin{bmatrix} -\frac{\beta\varepsilon_{xy}}{\varepsilon_{xx}} & z_0 - \frac{z_0\beta^2}{\varepsilon_{xx}} & -\frac{\beta\varepsilon_{xz}}{\varepsilon_{xx}} & 0 \\ \frac{\varepsilon_{yy}}{z_0} - \frac{\varepsilon_{xy}^2}{z_0\varepsilon_{xx}} & -\frac{\beta\varepsilon_{xy}}{\varepsilon_{xx}} & \frac{\varepsilon_{yz}}{z_0} - \frac{\varepsilon_{xy}\varepsilon_{xz}}{z_0\varepsilon_{xx}} & 0 \\ 0 & 0 & 0 & -z_0 \\ \frac{\varepsilon_{yz}}{z_0} + \frac{\varepsilon_{xy}\varepsilon_{xz}}{z_0\varepsilon_{xx}} & \frac{\beta\varepsilon_{xz}}{\varepsilon_{xx}} & \frac{\beta^2}{z_0} + \frac{\varepsilon_{xz}^2}{z_0\varepsilon_{xx}} - \frac{\varepsilon_{zz}}{z_0} & 0 \end{bmatrix} \begin{bmatrix} E_y \\ H_z \\ E_z \\ H_y \end{bmatrix} = \begin{bmatrix} \alpha_1^+ & 0 & 0 & 0 \\ 0 & \alpha_1^- & 0 & 0 \\ 0 & 0 & \alpha_2^+ & 0 \\ 0 & 0 & 0 & \alpha_2^- \end{bmatrix} \begin{bmatrix} E_y \\ H_z \\ E_z \\ H_y \end{bmatrix} \tag{5.31}$$

Here $\beta = n\cos\theta$ and $\alpha = n\sin\theta$. In this equation α is represented by a 4×4 matrix in terms of parameters α_1 and α_2.

Representing the 4×4 matrix of Equation 5.31 consisting of components of $\hat{\varepsilon}$ and β by $\hat{L}$ we can rewrite the eigen equation as

$$\hat{L}\vec{F} = \alpha\vec{F} \tag{5.32}$$

Here $\hat{F}$ is the field matrix vector and is represent in 4×4 matrix form as

$$\vec{F} = \begin{bmatrix} E_{y1}^+ & E_{y1}^- & E_{y2}^+ & E_{y2}^- \\ H_{z1}^+ & H_{z1}^- & H_{z2}^+ & H_{z2}^- \\ E_{z1}^+ & E_{z1}^- & E_{z2}^+ & E_{z2}^- \\ H_{y1}^+ & H_{y1}^- & H_{y2}^+ & H_{y2}^- \end{bmatrix} \tag{5.33}$$

In a layer with four field waves propagating due to multiple reflections and transmissions the field is represented as a basis wave by $\hat{F}$ multiplied by a complex coefficient $\hat{a}$. $\vec{a}$ is column vector denoting complex coefficients. a_1^+, a_1^-, a_2^+ and a_2^- are the elements of the complex coefficient $\vec{a}$. Here + and − represent the right going and left going wave components and the subscripts 1 and 2 denote the multiple reflections and transmissions. This is shown in Figure 5.6.

Thus the field $\vec{m}$ is denoted as

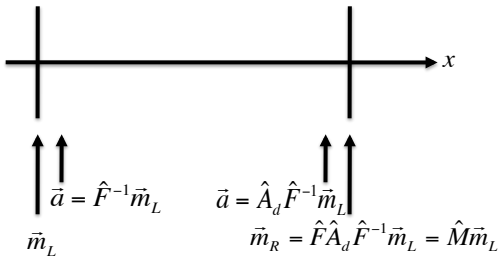

Figure 5.7: The characteristic matrix of a layer

$$\vec{m} \;=\; \hat{F}\vec{a} \tag{5.34}$$

i.e

$$\begin{bmatrix} E_y \\ H_z \\ E_z \\ H_y \end{bmatrix} = \begin{bmatrix} a_1^+E_{y1}^+ + a_1^-E_{y1}^- + a_2^+E_{y2}^+ + a_2^-E_{y2}^- \\ a_1^+H_{z1}^+ + a_1^-H_{z1}^- + a_2^+H_{z2}^+ + a_2^-H_{z2}^- \\ a_1^+E_{z1}^+ + a_1^-E_{z1}^- + a_2^+E_{z2}^+ + a_2^-E_{z2}^- \\ a_1^+H_{y1}^+ + a_1^-H_{y1}^- + a_2^+H_{y2}^+ + a_2^-H_{y2}^- \end{bmatrix}$$

Berreman 4×4 characteristic matrix transform the field elements E_y, H_y, E_z, H_z of Equation 5.31 propagating through a layer from input to output. The characteristic matrix is denoted by

$$\hat{M} = \hat{F}\hat{A}_d\hat{F}^{-1}, \tag{5.35}$$

where $\hat{F}$ is the field matrix and A_d is the phase matrix.

The field matrix which represents the reflection and transmission of the four field vectors inside a layer, transforms the field from inside the layer boundary to its boundary and is represented by Equation 5.33.

The phase matrix A_d which represents propagation of the incident field inside a

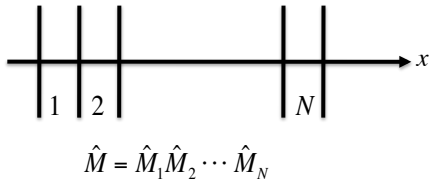

Figure 5.8: Characteristic matrix of a stack of N layers

layer is represented as

$$A_d = \begin{bmatrix} \exp[-i\phi_1^+] & 0 & 0 & 0 \\ 0 & exp[-i\phi_1^-] & 0 & 0 \\ 0 & 0 & exp[-i\phi_2^+] & 0 \\ 0 & 0 & 0 & exp[-i\phi_2^+] \end{bmatrix}$$

where $\phi_1^{\pm} = k\alpha_1^{\pm}d$ and $\phi_2^{\pm} = k\alpha_2^{\pm}d$

The characteristic matrix Equation 5.35 depicting the field propagating in a layer is shown in Figure 5.7. Here $\vec{m}_R$ and $\vec{m}_L$ are the field at the right and left layer shown in the figure respectively.

In this case as shown in Figure 5.7 the characteristic matrix $\hat{M}$ transforms the total field $\vec{m}$ across a layer from left to right. Starting on the left side, the total field $\hat{m}_L$ incident on the layer is transformed by the matrix $\hat{F}^{-1}$ to give the field coefficient $\vec{a}$ just inside the layer, then $\vec{a}$ is transformed across the layer by the phase matrix A_d, and finally transformed by the matrix $\hat{F}$ to give the total field $\vec{m_R}$ at the right layer interface.

The characteristic matrix of a stack of N layers as illustrated in Figure 5.8 is

$$\hat{M} = \hat{M}_1\hat{M}_2\ldots\hat{M}_N \tag{5.36}$$

The characteristic matrices relating the incident and transmitted intensity are

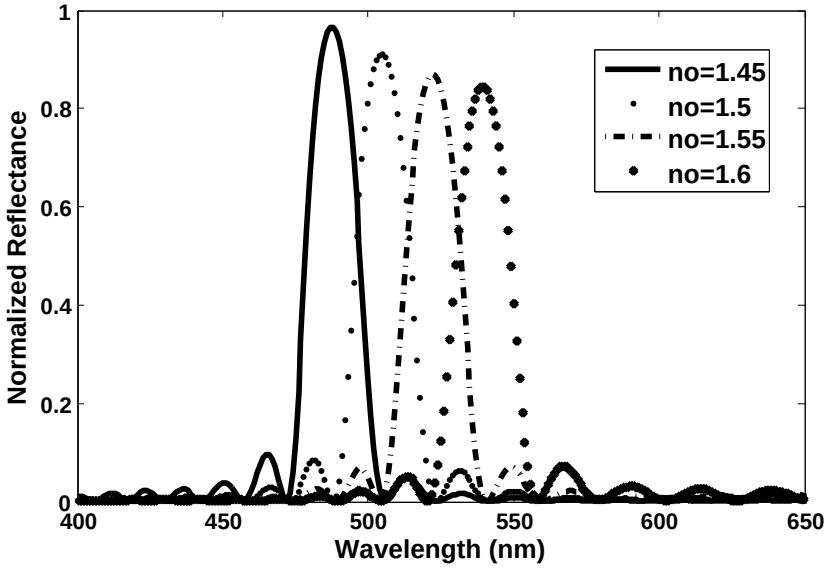

Figure 5.9: Simulated effect of average refractive index n_0 on the optical output response of HPDLCs using Berreman 4×4 matrix technique

now used to calculate the transmitted and reflected intensity.

Using Berreman 4×4 transfer matrix approach HPDLCs can be modeled having different dielectric and refractive index profiles[73].

The refractive index varies periodically along the grating vector K corresponding to the alternately varying polymer and LC layers. For ideal HPDLC gratings the refractive index is defined as a perfectly varying sinusoid.

Sinusoidal grating profile assumes that the layers are isotropic which is not the case for LC layers. However the randomly aligned LC droplets which are smaller than the interacting wavelength of light make it a good assumption in most cases. However for bigger micron sized droplets the refractive index profile is more complex than a simple sinusoid and is beyond the scope of this dissertation.

Figures 5.9 and 5.10 are simulated normalized output reflectance plot for varying parameters in the HPDLC system such as n_0 and n_1 of the sinusoidal refractive index profile depicted by Equation 2.14 using the Berreman 4×4 matrix method.

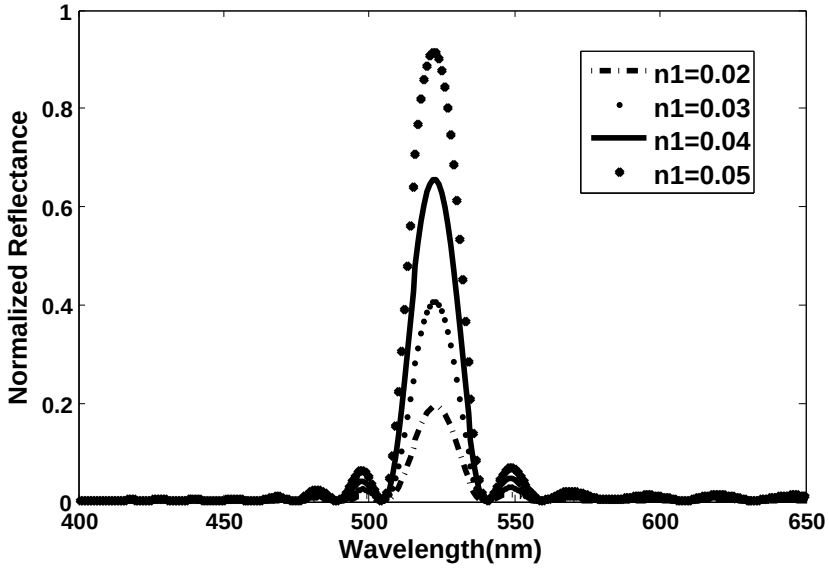

Figure 5.10: Simulated effect of refractive index modulation parameter n_1 on the optical output response of HPDLCs using Berreman 4×4 matrix technique

Here the rest of the parameters such as pathlength and thickness of the grating are maintained constant. These simulated plots indicate variations in optical output response parameters such as reflection efficiency, FWHM and peak Bragg reflection wavelength. Hence this modeling technique is used determine input parameters for a required optimal output response of HPDLC.

The refractive index are assumed to be perfectly sinusoid however perturbations can be added to this to feature the random feature size of the LC droplets [40] and also to show the scattering profile variation for different wavelengths.

In this chapter theoretical prediction techniques used to analyze the optical output of HPDLC gratings namely Raman-Nath theory, coupled wave theory and matrix methods were reviewed. Berreman 4×4 matrix technique was introduced to predict and analyze the output. This technique will be used in this dissertation to theoretically predict the optical output of broadband HPDLCs to tailor specific HPDLC output wavelength bandgap.

In the next chapter the optical output of HPDLCs developed for the wavelength sensing applications are analyzed and simulated using the Berreman 4×4 technique.

6. Spectral Sensing Application of Holographic Polymer Dispersed Liquid Crystals

6.1 Introduction

In this chapter we introduce fabrication techniques namely spatial multiplexing or pixelation, stacking and dynamic fabrication techniques for wavelength sensing application of HPDLCs. Their optical output is analyzed by using the Berreman 4×4 analysis technique detailed in the previous chapter. Phenomenological diffusion model along with the Berreman technique is used to determine the response of the dynamically fabricated HPDLCs.

6.2 Pixilation and Stacking Techniques

In the pixelation technique the HPDLCs gratings are spatially created on a single layer[74]. Multiple grating can be fabricated simultaneously by splitting a single laser beam into many beams or by using more than one laser or a combination of both. Figure 6.1(a) is an illustration of the pixelated structure having 4 HPDLCs. The different colors depict, four HPDLCs having distinct grating pitch resulting in the

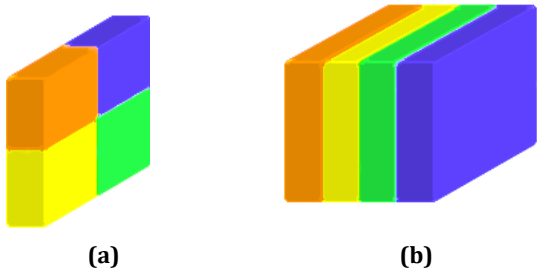

Figure 6.1: (a) Spatially arranged HPDLC configuration and (b) Stacked HPDLC configuration

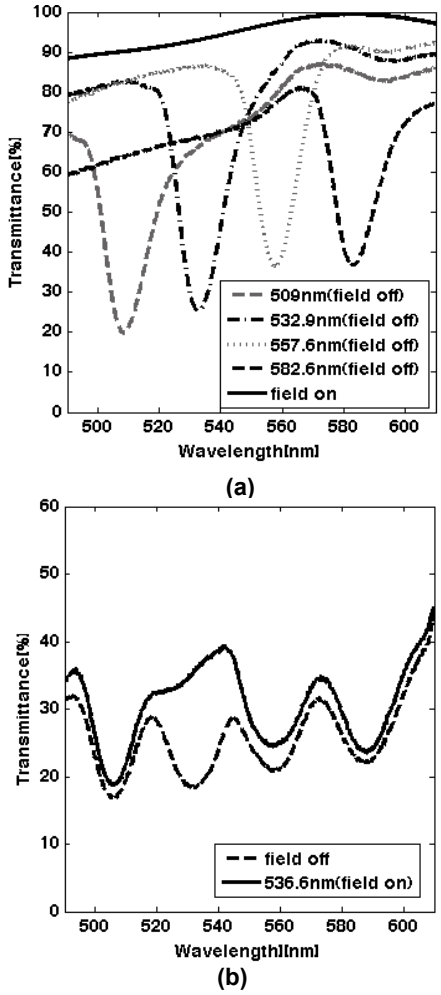

Figure 6.2: Transmitted intensity spectrum through pixilated and stacked HPDLCs from an incident white light source. a) Spectral response of the individual pixels of filter when no bias is applied and when bias is applied. b) Intensity envelope of the stacked HPDLCs with individual Bragg wavelengths of 505.9nm, 536.6nm, 550.9nm and 589.9nm stacked. The envelopes show intensity when all the layers are unbiased and when 536.6nm layer is biased.

reflection of four unique wavelengths when they interact with incident radiation. Pixilation technique is desirable since it creates multiple wavelength reflecting HPDLCs in a single filter layer using a one-step fabrication process.

In the stacking technique individual HPDLC cells are stacked one behind the other as shown in Figure 6.1(b) and they interact with incident wavelength in this configuration. Stacking technique was initially deployed on HPDLC for application development of displays[75].

6.2.1 Experimental Analysis

The response of a 4 pixel mask and 4 layer stacked HPDLC filter outputs are compared in Figure 6.2 for an incident white light spectrum. The individual pixel output characteristics are similar to the individual layer output characteristics of the stack. The FWHM of the pixels and the individual layers are 15nm and reflection efficiency in the order of 55%. Figure 6.2(a) shows the lineshapes of 4 pixel notches with an Ocean Optics white light source incident on them. The detected output is captured by an Ocean Optics spectrometer. The measured wavelengths of the each of the pixel are 509nm, 532.9nm, 557.6nm and 582.6nm. This mask can be fabricated on a substrate to electrically configure individual pixels or all the pixels together. In the output shown here all the pixels were manipulated simultaneous by applying field bias. Thus field biasing the pixilated mask resulted in the transmission of the entire incident source wavelengths as shown in the figure.

The stacked layer wavelengths had peak reflection at 505.9nm, 536.6nm, 550.9nm and 589.9nm. For this layered setup when a bias is applied to a layer the entire source wavelength incident on it, which includes its Bragg wavelength, is transmitted through as shown in the figure for the 536.6nm wavelength notch enabling the detection of the filtered wavelength.

As observed in the figure the reflection efficiency of each of the notch is reduced to 12% after stacking. This is caused by the scattering losses of each layer compounded by stacking the layers together. Thus there is a limitation of the spectral range of the stacked HPDLCs since increasing the layers decreases signal to noise ratio (SNR). However for pixilated filters innumerable pixels can be written without any loss of the SNR thus making it capable of being used for higher wavelength range than stacked HPDLCs. However increasing the number of pixels increases the complexity of the hologram fabrication setup and requires additional lasers to maintain a reasonable range of beam irradiance to form each pixel. Hence there is mainly a tradeoff between complicated fabrication process and wavelength range while considering one of the two filtering methods for broadening wavelength ranges.

6.3 Simulation of Single and Stacked HPDLCs

The expected transmitted wavefront from a single or stacked layer of HPDLCs can be simulated by using the Berreman 4×4 technique explained in detail in the previous chapter.

The optical output and simulated output of a single wavelength reflecting HPDLC formed by a pixel or single layer is shown in Figure 6.3. The optical output of a stack of two layers of HPDLCs is shown in Figure 6.4.

The pixelated and stacked HPDLCs for wavelength sensing applications is explained in detail in Chapter **??**. The next section details the multiplexing technique used for varying the interaction wavelength of single layer HPDLCs.

6.4 Dynamic Multiplexing

Controlling the optical setup during grating formation for broadening the spectral interaction range involves spatial, angular and time multiplexing techniques. Here we

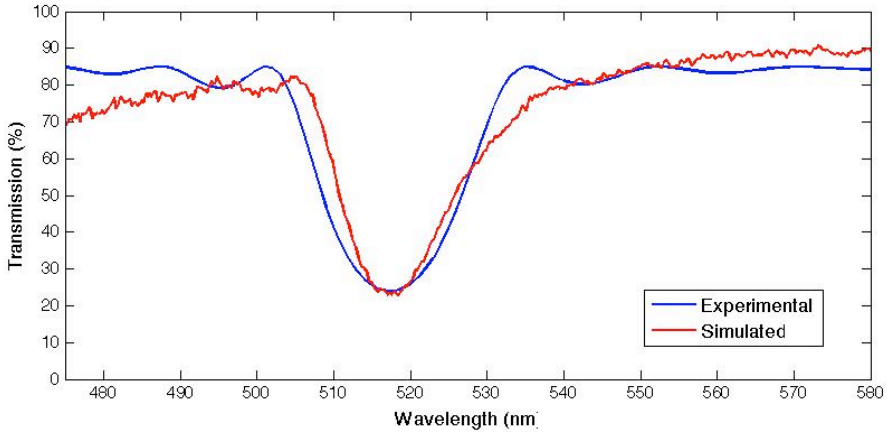

Figure 6.3: Comparison of the simulated wavefront to the experimentally determined spectrum optical output of a single wavelength reflecting HPDLC

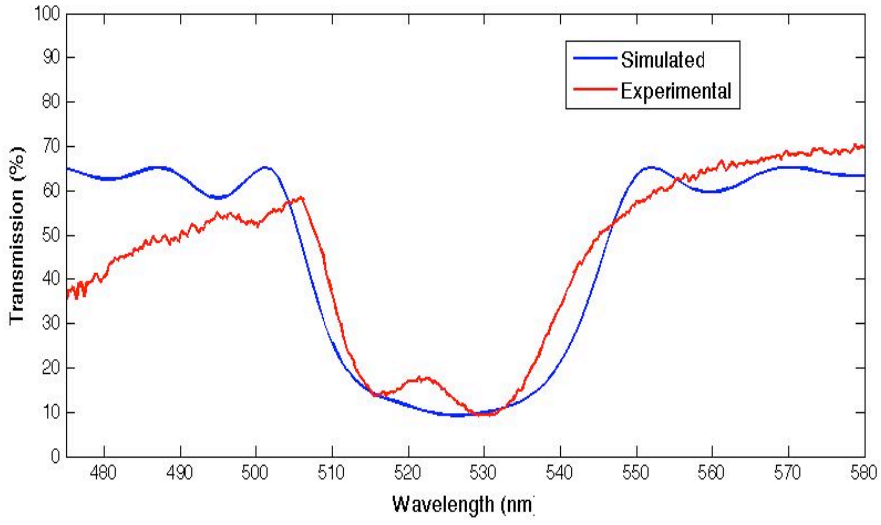

Figure 6.4: Comparison of the simulated wavefront to the experimentally determined spectrum optical output for two single wavelength reflecting stacked HPDLCs

discuss a new technique for forming simultaneously space and time multiplexing. Dynamically varying the exposure angles during grating formation is the key to forming multiple gratings resulting in continuous broadband reflection gratings. Motorized translation and rotation stage are used to continuously vary the incident exposure beam angles during the curing process.

Predictive theoretical modeling of the optical output is useful for obtaining the desired wavelength notches from the gratings. This is helpful in designing the formation configuration for each desired notch wavelength prior to grating formation, thus saving time. To support the predictive modeling, modeling parameters such as LC droplet size, grating pitch and LC orientation order are obtained by experimental analysis of the HPDLC using microscopy and spectroscopy studies and can be applied to the broadband studies. In the next section we study the standard techniques used to study the wavelength interactions in holograms and applying this technique to our system. Here the Berreman technique is applied in depth to the HPDLC analysis and will be applied to the dynamic gratings in the next section.

6.5 Broadband Techniques

6.5.1 Change in Material Composition

Hsiao et al have included acetone in the prepolymer recipe to broaden and improve the HPDLC reflective wavelength[76]. The addition of acetone results in the formation of controllable periodic voids inside the thin film after the acetone evaporates. Peak reflectivity as high as 80% and a broad reflection bandwidth of 80 nm was observed. However, due to the presence of air gaps, these materials are not switchable.

6.5.2 Various Multiplexing Techniques

Multiplexing techniques used for broadening peak wavelength include spatial, time and angular multiplexing methods. Bowley et al have used angular multiplexing to create multiple gratings using 3 beams at different angles[77]. In these HPDLCs there is an interaction of both transmission and reflection gratings, making noisy gratings. Fontecchio et al created multi wavelength reflecting HPDLCs using all the three multiplexing techniques[74]. In the spatial multiplexing method, they used three beam pairs oriented at different angles and three mask pairs to create an RGB color pixel array. During fabrication multiple laser beams were made incident at different angles on a particular area of the HPDLC. Multiple gratings in a single sample can improve the viewing angle and reflection bandwidth by enabling specular reflection off multiple gratings. Angular multiplexing was also performed temporally where two counter-propagating beams were used to expose the sample. They were then blocked off and two other counter-propagating beams pairs at a different angle were made incident on the same region on the sample.

Here we describe the formation of broad wavelength notch spanning, electrically controllable thin films. In this work the reflected notch is attuned during the hologram formation by dynamically varying the formation setup for a broader interaction wavelength range. The thin films are holograms formed of layered liquid crystal and polymer matrix. Applying an electric field across the HPDLC medium controls intensity of the reflected wavelength. The field transforms it from a wavelength selective device to an optically transparent state. Typically HPDLCs have a narrow peak reflection wavelength with a full width at half maximum (FWHM) of 5 to 20nm and the reflected peak corresponds to the Bragg reflecting wavelength. Efforts have been made to broaden the interaction wavelength using various methods. The peak interacting wavelengths of the HPDLCs can be broadened to reflect multiple wavelengths

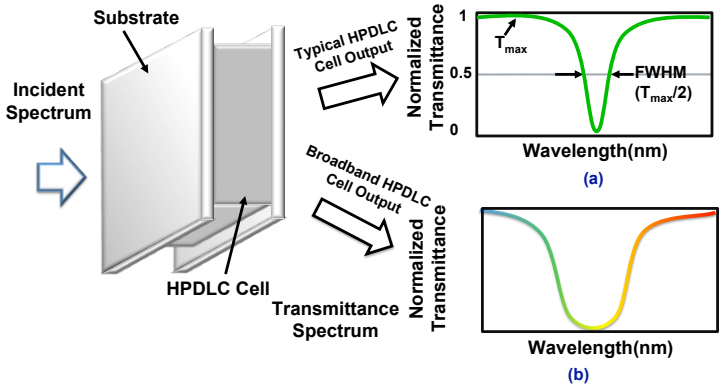

Figure 6.5: Output Response of HPLDC when a white light source is incident on it. (a) Single wavelength reflected. (b) Broadened wavelength reflected

or have a continuous broadened reflection peak using methods such as changing material composition, stacking and multiplexing techniques.

Broadband reflecting HPDLCs are advantageous since they eliminate the need for stacking specific single layer HPDLC filters if a broad interaction range is required and thus reduce losses associated with each layer. Some of the significant applications for broad wavelength spanning HPDLCs are beam steering for instrument clusters, hyperspectral imaging, wavelength filtering and construction of lightweight optics. Broadband reflecting wavelengths is a critical step towards formation of switchable broadband HPDLCs for implementing beam steering capability. The multiple broadband, stacked HPDLCs are able to selectively focus the specific wavelengths for numerous instruments. This clustering is desirable in space borne satellite applications. No moving parts, lightweight and small footprint make them particularly desirable compared to prisms and lenses because vibrations, weight and real estate are critical design parameters. The high color purity of HPDLCs is a desirable feature for applications such as hyperspetral imaging. This device analyzes object using different spectral sections. Since different space objects have distinctive spectral patterns at various wavelengths, studying it will aid in their characterization. Broadband

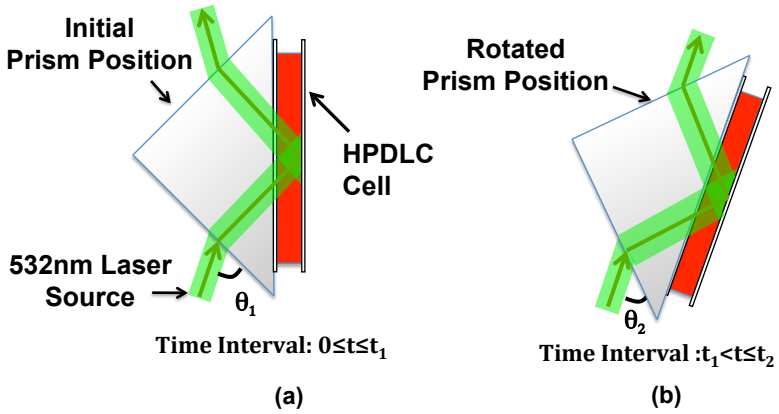

Figure 6.6: Broadband Grating Formation

HPDLCs as light filters aids in higher device sensitivity and reliability along with the added advantage of lightweight optics.

6.6 Dynamic Time Multiplexing

Controlling the optical setup during grating formation for broadening the spectral interaction range involves spatial, angular and time multiplexing techniques. Here we discuss the simultaneously space and time multiplexing technique. Varying the exposure angles during grating formation is the key to forming multiple gratings resulting in continuous broadband reflection gratings. Motorized translation and rotation stage are used to continuously vary the incident exposure beam angles during the curing process.

6.6.1 Fabrication Technique

Reflection hologram using prism method of fabrication and thiolene formulation is considered here. The grating formation using acrylate formulation is faster compared to the thiolene formulation as seen in Section 3.1.2. Experimentally it was determined to be less than 1s for acrylate while it was determined to be in the range of 1.5s for

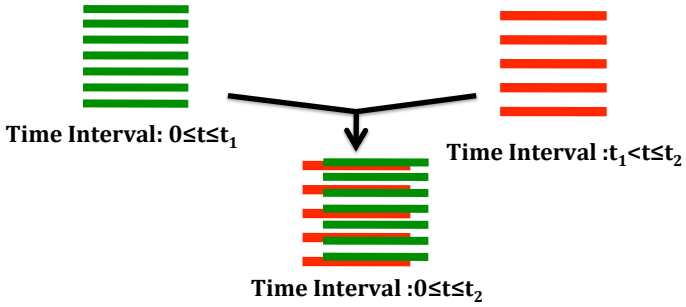

Figure 6.7: Grating Overlap

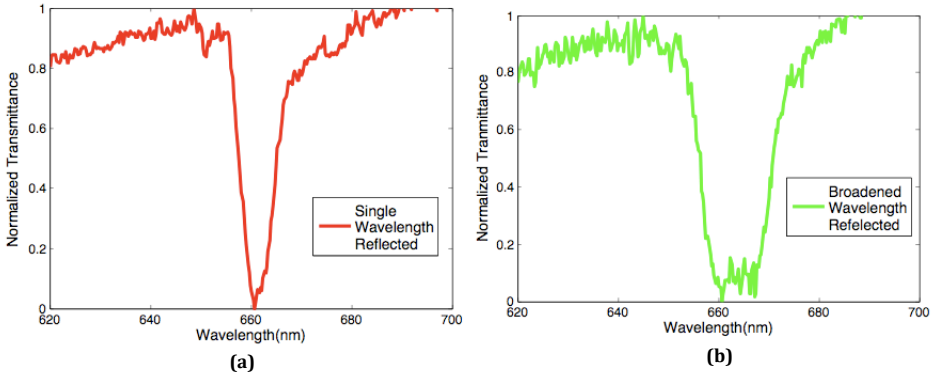

Figure 6.8: Output Transmitted Spectrum through (a) Single wavelength reflecting HPDLC b) Dynamic time multiplexed HPDLC

thiolene. Due to the limitation in the fast moving rotation stage we used the thiolene formulation to fabricate the HPDLCs.

The fabrication setup is shown in Figure 6.6. Varying exposure angle broadens the Bragg grating pitch, which interacts with a band of wavelengths instead of the traditional single wavelength peak.

The overlapping structure formed by this is indicated in Figure 6.7. Here the grating pitches are offset slightly to visualize them better.

6.6.2 Results

Experimental results have indicated that traditional acrylate formulations cure too quickly since the gelation process is less than 1/8th of a second. There is a physical limitation on the speed of the translating mirror, which prevents its operation for this duration. Since the mechanical translating and rotating arm of the setup do not meet this requirement, we use a thiolene formulation, which has a slower gelation process and is hence more controllable. The gelation process takes place at about 1.4s for our thiolene formulation. Multiple gratings were created in a single medium that created peak broadening as shown in the Figure 6.8. The individual Bragg peaks have a FWHM of 9nm at 660.9nm and 662.2 nm reflecting peaks highlighted in red and blue. The broadened peak using the broadband technique has a broadened peak of 15nm as shown in the figure.

SEM Imaging

SEM images of cross sections of HPDLCs fabricated by the new dynamic technique were compared to the normally fabricated technique as shown in Figure 6.9 to understand their morphological features.

The typically fabricated HPDLC SEM images indicate a well defined LC layered structure as shown in Figure 6.9(a). The dark voids indicate the LC droplets arranged in layers surrounded by polymer matrix binders as shown. Since thiolene formulation is used the LC droplets are more spherical and discrete compared to the elongated overlapping LC droplets of acrylate formulation. Here grating pitch is the distance between the centers of adjacent LC layers and is easily determined by SEM image analysis.

For dynamically fabricated HPDLCs grating overlap takes places. Due to this the LC and polymer layers are not well defined. Also the grating pitch cannot be

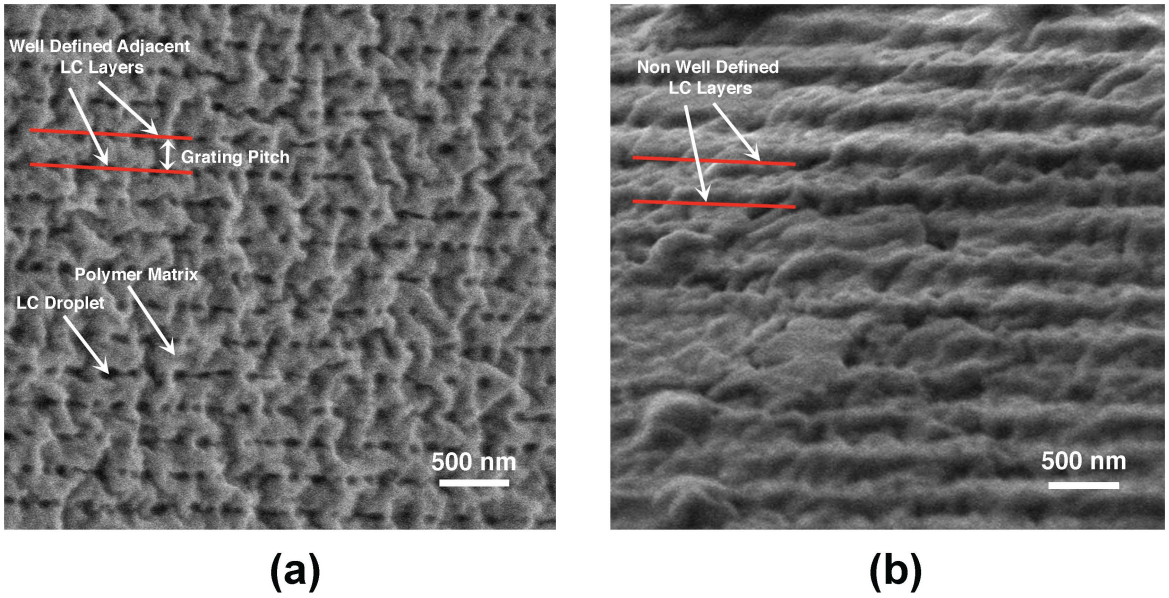

Figure 6.9: SEM images of cross-section of HPDLCs. (a) SEM image showing well defined layered LC/polymer grating structure. (b) SEM image showing non-well defined LC/polymer layered structure due to overlapped gratings

measured since it varies along the cross section as shown in Figure 6.7 and observed in Figure 6.9(b).

Wavefront Analysis

One of the end goals of this research is creation of high quality optical components, using HPDLC films having good wavefront quality. In order to determine how well the devices are formed the quality of the wavefront transmitted through the HPDLC cells are determined using Shack-Hartmann wavefront sensor as described in Section 2.6.3 and Section 3.2.3

To analyze the quality of the gratings the test setup shown in Figure **??** is designed.

Zernike coefficients of Equation 3.2 which quantifying aberrations parameters are experimentally determined and tabulated in Table 6.1 to quantify the difference in the grating aberrations for a single wavelength reflecting and broadband wavelength

Table 6.1: Zernike coefficients of primary aberrations for single and broadened wavelength reflecting HPDLCs

Parameters	Single Wavelength Reflecting HPDLC	Broadband Wavelength Reflecting HPDLC
X-Tilt	0.004864	-0.005948
Y-Tilt	0.004025	0.008941
Defocus	0.000000	0.000000
0-Astigmatism	0.058925	0.069977
45-Astigmatism	0.031647	-0.035237
X-Coma	-0.005784	0.007703
Y-Coma	-0.001627	-0.009458
Spherical	-0.008886	0.002302

Table 6.2: Wavefront characterizing parameters for single and broadened wavelength reflecting HPDLCs

Parameters	Single Wavelength Reflecting HPDLC	Broadband Wavelength Reflecting HPDLC
P-V	0.1574	0.1734
Strehl Ratio	0.8663	0.8551
RMS Wavefront Error	$\lambda/19.25$	$\lambda/16.4$

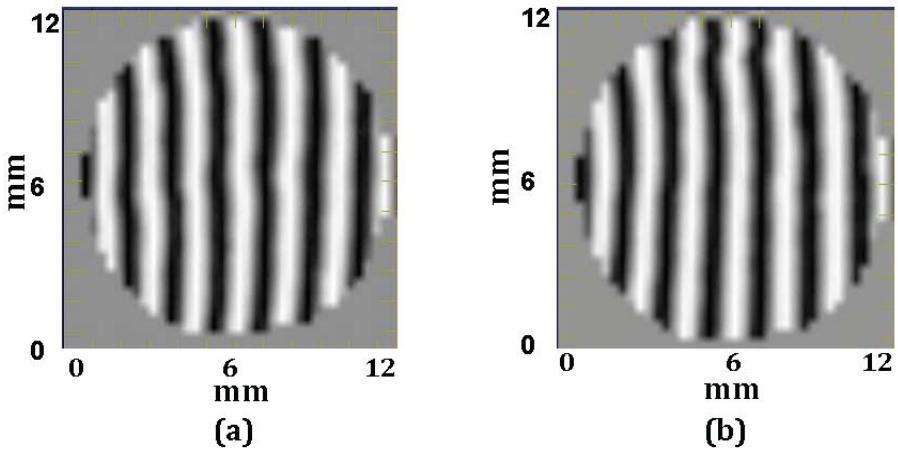

Figure 6.10: Fringe Pattern

reflecting HPDLCs. Other wavefront characterizing parameters Peak to Valley, Strehl ratio and RMS wavefront error are listed in Table 6.2.

From the Table 6.1 it can be seen that minor aberrations are observed in the gratings and the aberration parameters for broadband gratings are marginally higher due to the grating overlapping structure creating more refractive index variation captured by the wavefront sensor. Strehl ratio and RMS wavefront error tabulated in Table 6.2 are $\geq$ to 0.8 and $\leq \lambda/14$ respectively for both types of grating considered here. Hence using Maréchal criteria defined in Section 3.2.3 the system can be defined as well optimized for device applications.

Figure 6.10 shows the reconstructed optical wavefront viewed as a fringe pattern generated by the wavefront analyzer for both these systems. Ideally the fringe pattern should be perfectly parallel to each other. A slight curvature in the fringes detected in the fringe is primarily result from the astigmatism introduced in the wavefront transmitted through the HPDLC sample as indicated in Table 6.1. Thus it can be deduced that broadband grating transmit good optical quality flattened wavefront suitable for device application from factors such as Table 6.1, Maréchal criterion and Figure 6.10 .

6.6.3 Analysis using Berreman's 4×4 Technique

To begin with, the refractive index for the overlapped grating is determined. For single wavelength reflecting HPDLC sinusoidally varying refractive index are assumed and they accurately predict the output behavior. Here a diffusion model is used to predict the refractive index of HPDLCs which is incorporated in to the Berreman 4×4 technique to predict the optical output transmitted by the grating structure.

Refractive Index Modeling

The refractive index variation is predicted using the phenomenological diffusion model for determining the kinetics of grating formation for holographic photopolymers[78, 79] adapted for HPDLC systems[80, 81].

The evolving monomer concentration during HPDLC fabrication is developed from Fick's second law of diffusion for a material in an unsteady state, given by

$$\frac{\partial c}{\partial t} = \frac{\partial}{\partial z}\left[D\frac{\partial c}{\partial z}\right],$$

where c is material concentration, D is diffusion constant and z is the distance diffused in the time interval t.

The spatial and temporal partial differential equations governing the monomer concentration $\phi_M(z,t)$ accounting for their depletion during polymerization can be written implementing Fick's law as [80, 81]

$$\frac{\partial \phi_M(z,t)}{\partial t} = \frac{\partial}{\partial z}\left[D(z,t)\frac{\partial \phi_M(z,t)}{\partial z}\right] - F(z,t)\phi_M(z,t), \tag{6.1}$$

where the parameter $D(z,t)$ is the dynamic diffusion constant and $F(z,t)$ is the reaction rate for the monomers.

The evolving dynamic diffusion constant $D(z,t)$ is defined as

$$D(z,t) = D_0 \exp\left[-\alpha\phi_m(z,t)\right]$$

Here D_0 is the initial diffusion constant of the pure monomer and α is the decay constant. $D(z,t)$ indicates an exponential decrease due to increasing density of the polymer network during fabrication.

The reaction rate is determined by the equation

$$F(z,t) = \gamma(z,t)\sqrt{I(z,t)} = \gamma_0 \exp\left[-\alpha\phi_m(z,t)\right]\sqrt{I(z,t)}$$

where $\gamma(z,t)$ is the polymerization rate coefficient, γ_0 is the characteristic rate coefficient of the monomer and $I(z,t)$ is the intensity of the photopolymerizing laser.

The differential equation to predict polymer concentration $\phi_P(z,t)$ resulting from monomer polymerization during the evolving fabrication process from Equation 6.1 is determined as

$$\frac{\partial\phi_P(z,t)}{\partial t} = F(z,t)\phi_M(z,t)$$

From the determination of the concentration of the polymers and the monomers the concentration of the LC during polymerization can be determined as

$$\phi_{LC}(z,t) = 1 - \phi_M(z,t) - \phi_P(z,t) \tag{6.2}$$

The intensity of the interference pattern generated at the hologram due to counter-propagating laser beams is determined by rewriting the Equation **??** in Section2.4

$$I = I_0(1 + V\cos(2\pi z/\Lambda_1)) \quad for \quad 0 \le t \le t_1$$

$$I = I_0(1 + V\cos(2\pi z/\Lambda_2)) \quad for \quad t_1 < t \le t_2$$

The average refractive index of the grating is expressed as

$$n(z) = \sqrt{n_{LC}^2\phi_{LC}(z) + n_P^2\phi_p(z)}$$

After the photopolymerization is complete, from law of mass conservation we can

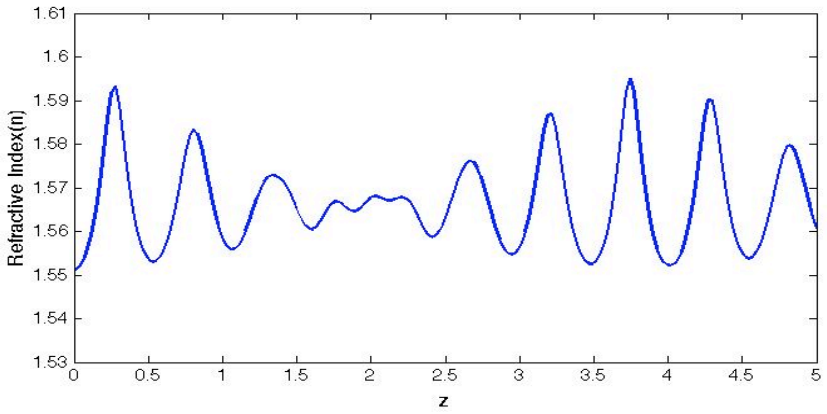

Figure 6.11: Simulation of the refractive index profile for the broadband grating

write the Equation 6.2 as

$$\phi_{LC}(z) = 1 - \phi_P(z)$$

Thus we can rewrite the refractive index equation as

$$n(z) = \sqrt{n_{LC}^2(1 - \phi_P(z)) + n_P^2\phi_p(z)}$$

This is plotted as a function of the thickness of the grating as shown in Figure 6.11.

Hence using the phenomenological diffusion model alongside Berreman 4×4 matrix the broadened output is simulated as shown in Figure 6.12.

Thus in this chapter both the spatial multiplexing and dynamic fabrication techniques were used to filter wavelengths. The techniques used in this chapter are used to develop the wavelength sensing application detailed in the next chapter. SEM imaging and wavefront analysis was performed on the novel broadband grating to understand their microscopic properties and optical quality of the output wavelength. High quality optical wavefront were measured making broadband HPDLCs feasible for device applications. Berreman 4×4 technique and phenomenological diffusion model

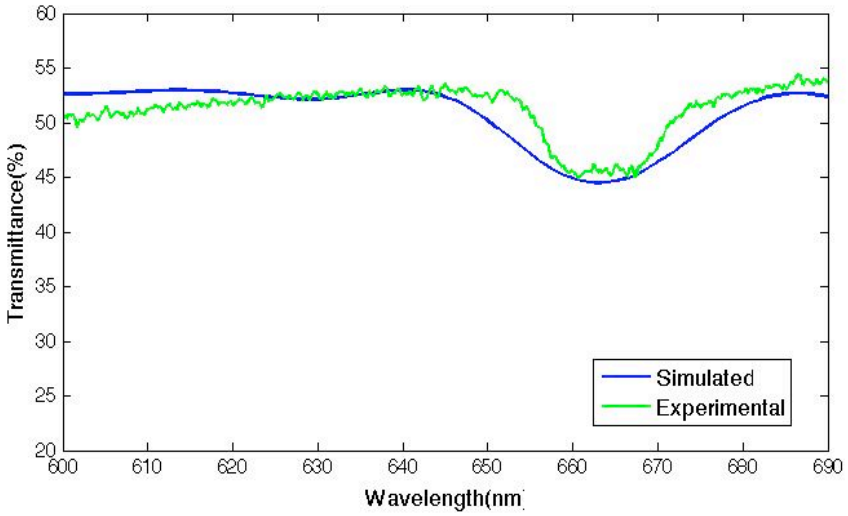

Figure 6.12: Simulation of broadened reflection grating by dynamic time multiplexing

are used together to theoretical predict the optical output in this chapter. They are found to be in close correlation with the experimental results.

7. Applications

The switchable and reflective properties of HPDLCs have been studied extensively for multiple electro-optical applications. Cairns et al have studied the strain sensitivity of the HPDLCs. They observed a spectral blueshift of the reflected wave by increasing physical strain, making applicable optical pressure sensor[82]. Tanaka et al have stacked multiple wavelength reflecting HPDLCs to enable the creation of reflective displays[75]. Domash et al and Ermold et al have created electrically controllable lenses for potential use in remote sensing[83, 84]. Fontecchio et al have used different formation configurations to create filter arrays for display and wavelength filtering[74]. Domash et al have demonstrated the feasibility of using HPDLCs as optical color filters for microdisplays, application specific integrated lenses to perform the function of individual lenses, mirrors, prisms etc, electro optic switches used for routing particular wavelength[85]. HPDLC technology used for multiple electro-optic components such as lenses, filters and switches have found wide-ranging application in the design of integrated optics. Some of the other currently evolving applications of HPDLCs are tunable photonic crystals, controllable photomasks and dynamic beam steering devices.

Here we briefly review the applications of HPDLCs by varying their interaction wavelength. This is done by the method of pixelation, stacking and broadband fabrication. Another application of HPDLCs is in pressure sensors where hydrostatic pressure applied on it changes the grating pitch resulting in varied reflection spectrum. Thus HPDLCs as pressure sensors are used for to sense wavelength changes for device applications. Techniques to improve the pressure response is discussed here.

7.1 Imaging Application

In this work seeking to achieve broadband wavelength reflecting HPDLCs, they are pixilated and stacked HPDLCs for use in an optical spectrometry. In a typical wavelength detecting spectrometer, a prism or diffraction grating separates incident wavelengths based on their refractive index. An arrayed detector captures these separated wavelengths and characterizes them individually. In reflection HPDLC based grating spectrometers, the wavelengths are passed through a filter consisting of multiple HPDLCs. When the incident wavelengths match the HPDLC filters, they are detected. The wavelength reflected by the HPDLCs typically has a full width half maximum (FWHM) of 10 to 25nm. As mentioned earlier, stacking the HPDLCs with different grating pitches, controlling the optical setup during the grating fabrication process and varying the recipe preparation, can broaden the interaction wavelengths. Controlling the optical setup during grating formation for broadening the spectral interaction range involves spatial, angular and time multiplexing techniques[74]. For spectrometer application development we use both spatial multiplexing technique and stacking technique.

7.1.1 Pixelated HPDLC

Pixilation technique is desirable since it creates multiple wavelength reflecting HPDLCs in a single filter layer using one-step fabrication process. Multiple wavelength reflecting HPDLCs are embedded on a pixilated mask which is the wavelength-separating segment of the spectrometer. An arrayed CCD detector measures individual intensities transmitted by each of the pixels. This setup is used to detect the spectral bands corresponding to the pixels. Final detection of a particular source wavelength is a two-step process. In the first step the wavelengths to be analyzed are passed through the mask and its individual pixel intensities is measured at the

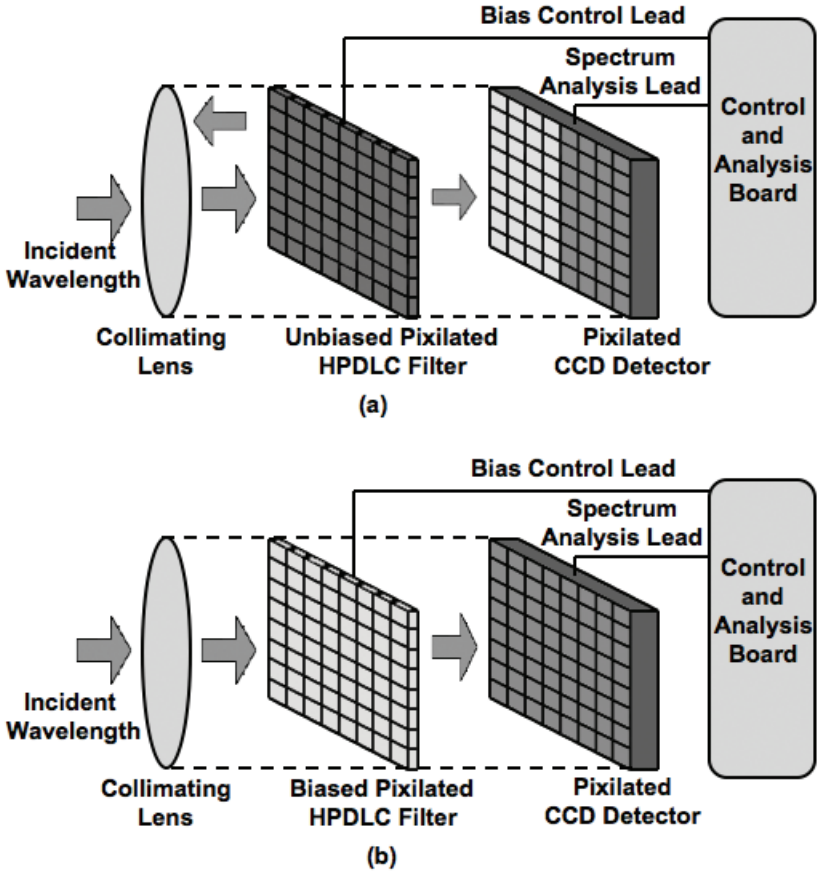

Figure 7.1: Illustration of the working principle of the pixilated spectrometer. A test source wavelength corresponding to left half HPDLC pixels of the filter is incident and the transmitted intensity at the detector is analyzed. a) In the unbiased state, the HPDLC pixels on the left half of the filter reflect incident wavelength matching their Bragg wavelengths. The pixels on the right half of the mask transmit the incident wavelength shown color coded at the detector. b) In the biased state the incident wavelength is transmitted through all the pixels and detected at their corresponding CCD pixels. Evaluating the intensity variation between the unbiased and the biased state the wavelength corresponding to the left half of the mask is detected.

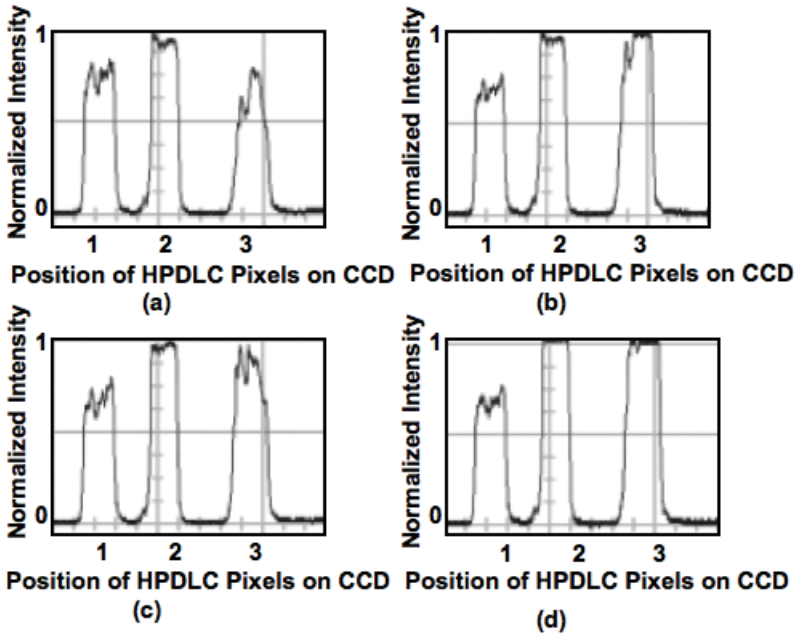

Figure 7.2: Intensity detected at the detector filtered through a 3-pixel filter for different incident wavelengths. a) Incident wavelength is 564nm corresponding to the third pixel wavelength. b) Bias is applied. c) Incident wavelength of 600nm not corresponding any of the pixel Bragg wavelengths. d) Bias is applied

detector end. In the second step a field is applied causing the transmittance of the entire incident wavelength range through the mask and mapping of the complete incident intensity at the detector. A change in intensity detected at the detector pixel after the two-step process results in the wavelength corresponding to the particular wavelength reflected by the pixels to be detected.

To demonstrate the working of this spectrometer a simple setup is shown Figure 7.1(a). Here all the pixels at the left half of the mask have one particular Bragg reflecting wavelength. When a source comprised of this wavelength is incident, the pixels on the left half of the mask reflect it. The pixels at the right half of the mask transmit the test source. Biasing the mask as depicted in Figure 7.1(b) results in the transmittance of the incident wavelength through all the pixels in the mask to the pixilated detector. The change in the intensity at left half of the mask between the biased and the unbiased state is recorded and enables detection of wavelength corresponding to these pixels. No intensity variation detected at the right half of the mask infers that the test wavelength does not correspond to any of these pixels.

To experimentally demonstrate the proof of concept for the pixilated spectrometer a simple setup is constructed consisting of a monochromator light source Cornerstone 74100 from Newport, 3-pixel HPDLC filter and grayscale CCD detector XC-77 from Sony all placed in line. The CCD detector is connected to an oscilloscope to enable convenient viewing of its detected intensity. The pixilated filter is connected to an electric field generating setup to bias and unbias it. For easy interpretation of the output a 3-pixel filter was made with all of them in a single row. The wavelengths of the pixels fabricated into the filter were 506nm, 527nm and 557nm. For demonstration of the pixilated spectrometer concept, the monochromator source is made to output wavelengths sequentially, matching the Bragg peak wavelengths of the 3 pixels for measuring the response of the filter. This is recorded at the CCD detector

end for both unbiased and biased state of the filter. Figure 7.2(a) 7.2(b) shows the oscilloscope output results when 564nm corresponding to the pixel 3 is made incident on the mask. In the unbiased state 3 distinct electric field intensities are detected as shown Figure 7.2(a). Figure 7.2(b) shows an intensity increase of 33% percent only in the third pixel when the filter is biased thus enabling detection of the 557nm pixel wavelength. When a source wavelength other than the pixel matching wavelengths is incident there is no variation in the detected intensity between the unbiased and biased state. This is demonstrated for the wavelength 600nm seen in Figure 7.2(c) and 7.2(d) respectively. Thus the pixilated filter is demonstrated to detect wavelength corresponding to its pixel wavelengths.

7.1.2 Stacked HPDLC

There are two types of spectrometer based on stacking using HPDLCs. The two configurations differ in the placement of the detector. In the reflection mode spectrometer the detector is placed at the reflecting end of the stack[86] and in transmission mode the detector captures the incident wavelength transmitted from the stack[87]. In the transmission mode stacked HPDLC spectrometer each layer of the stack is mapped with the source intensity detected at the detector. The layers are time sequentially biased individually. The stack transmits the source wavelength when the HPDLC layer matching its wavelength is biased. The detected intensity is mapped to the biased layer and the source wavelength is detected.

Figure 7.3 shows schematic of a stack of 4 layers of HPDLCs with each layer color-coded to represent different reflection wavelengths. The optical output response of each of the 4 layers and of the stack(stack response is depicted by a black line) is shown in Figure 7.3 (b). They reflect four individual wavelengths with wavelength peaks of 507.9, 517.6, 532.5 and 542.6nm respectively. When a bias is applied to one

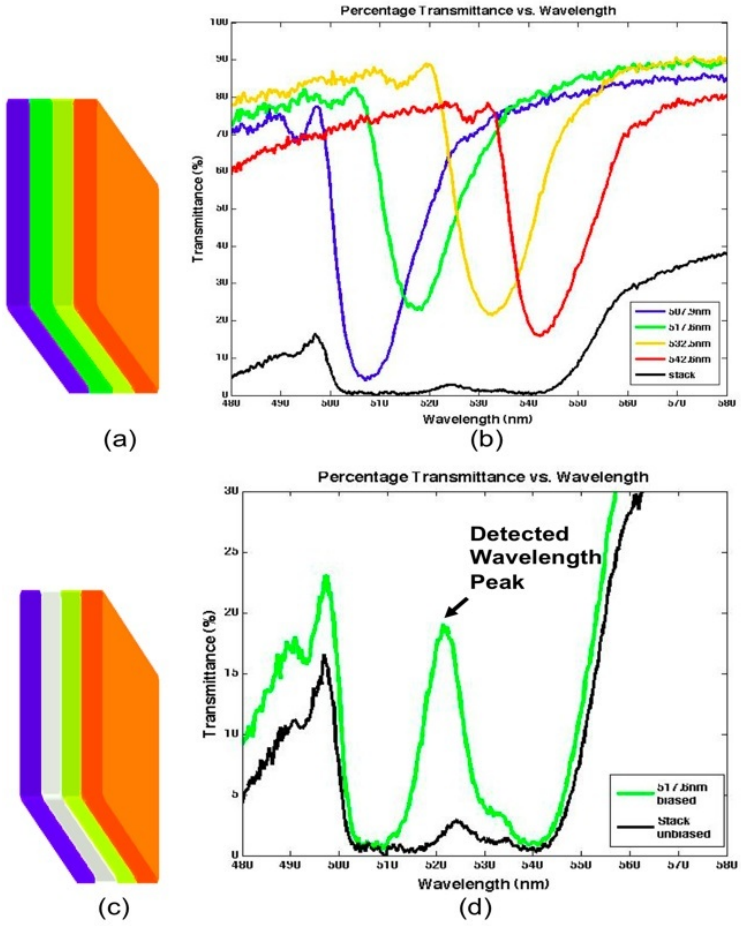

Figure 7.3: Schematic representation of four layers of HPDLCs stacked. Each layer is represented with different colors depicting four different wavelength reflected. (b) Optical response of each of the four layers stacked. The black envelope represents the optical response when all the 4 layers are stacked. (d) Stack representation when an electric field is applied to the second layer. (d)The optical response of the stack indicating the transmission of the wavelength corresponding Bragg reflection wavelength of the second layer

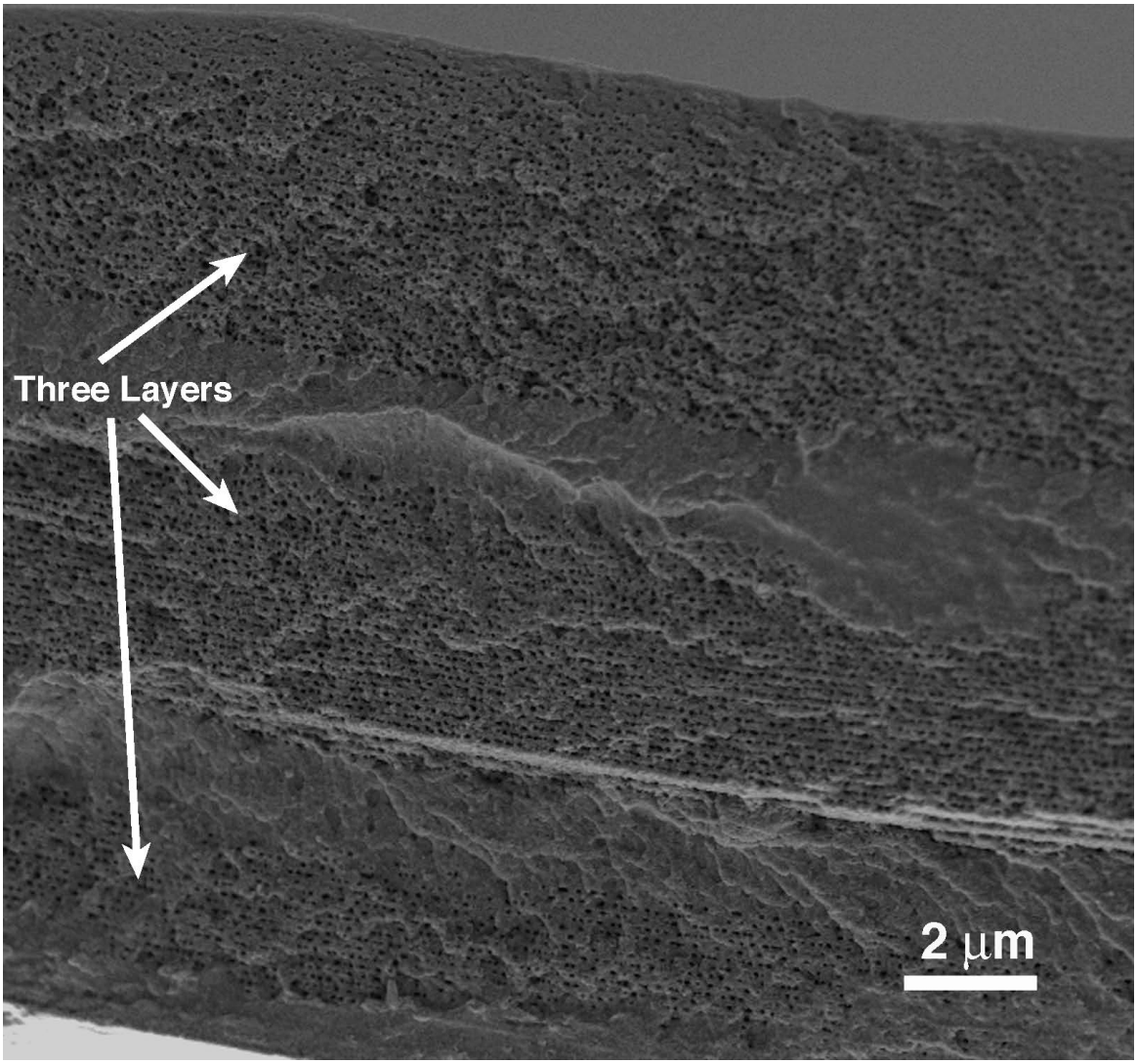

Figure 7.4: Stack of 3 layers of HPDLCs by the method of spin coating

of the 4 layers it become optical transparent. The clear second layer of the stack represents this in the schematic in Figure 7.3 (c). The optical response of the stack shown in Figure 7.3(d) indicates the wavelength corresponding to the switched layer to pass through and be detected by a spectrometer. This feature can be used to develop a low cost spectrometer to detect specific wavelength of light.

Stacking multiple gratings in one composite device creates a broadband HPDLC grating here. For a conventional stack each filter of the stack is prepared individually and then glued one behind the other using index matching glue.

Technique of using double sided ITO coating yielded the best results for stacking. In this alternate technique the number of substrates required to make a stack are reduced and addition of index matching fluid between layers is eliminated hence reducing the optical path length of the stack by 33%. This method also reduces the amount of Fresnel reflection loss and parallax in the stacked filter[88]. Hence in the reduced optical path length stack a substrate (coated with ITO on both sides) is shared by two filters hence reducing the number of substrates required to make a stack maintaining the requirement of individually controllable layers.

Another technique to reduce the stack length is by spin coating the prepolymer syrup on a glass slide and then form a hologram. Again another prepolymer syrup layer is spin coated and fabricated into a HPDLC thus eliminating the substrate completely. Figure 7.4 shows a stack of 3 layers of HPDLCs fabricated this way. For electro optical control a conductive layer can be spin coated between the HPDLC layers. Thus different stacking techniques are explored here for wavelength sensing application.

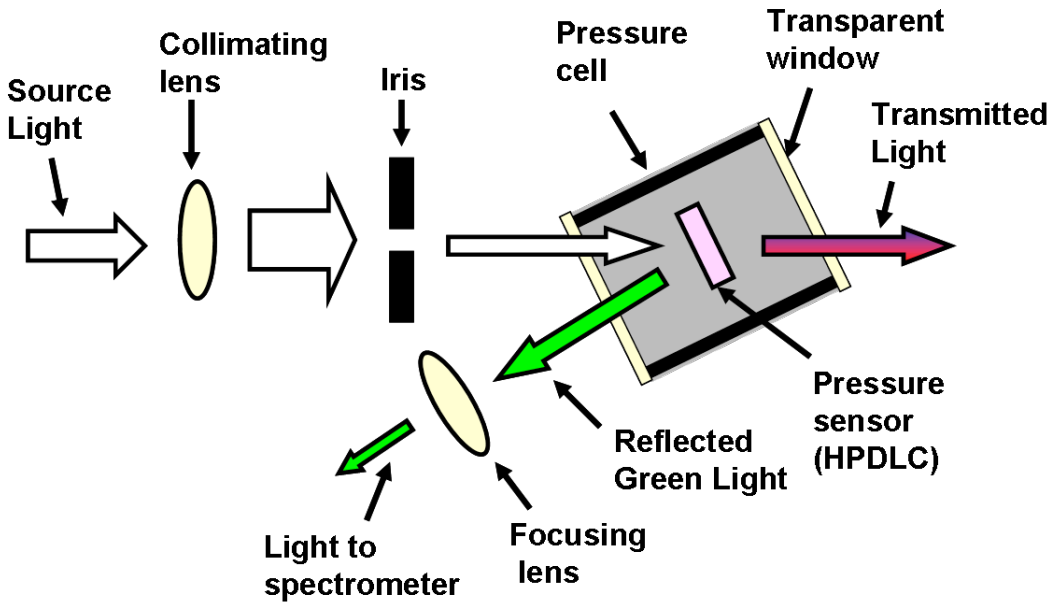

Figure 7.5: Experimental setup of the optical elements for reading the reflected wavelength of HPDLC.

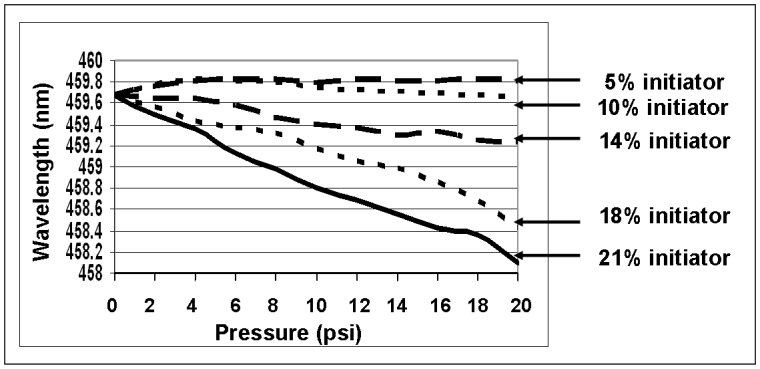

Figure 7.6: Wavelength vs. pressure response of di-functional HPDLC with pressure applied from 0-20 psi.

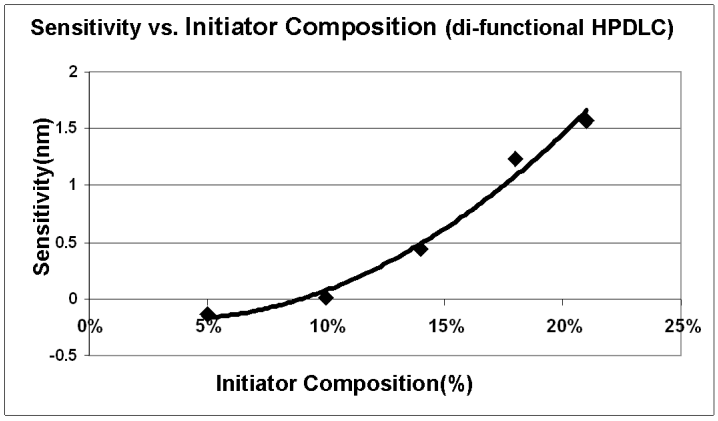

Figure 7.7: Sensitivity (measured as the maximum shift in the reflected wavelength) vs. Initiator composition for the di-functional HPDLC.

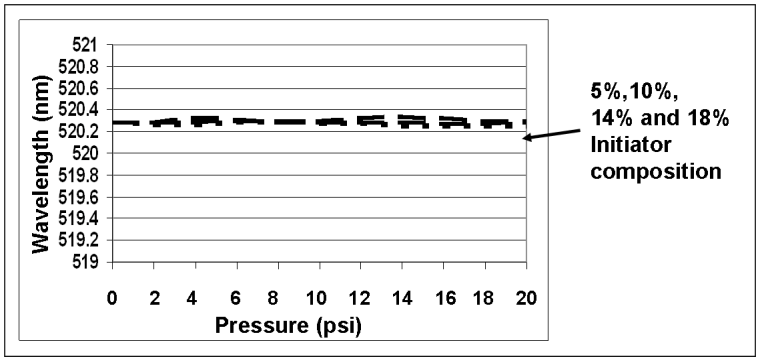

Figure 7.8: Wavelength vs. pressure response of tri-functional HPDLC with pressure applied from 020 psi.

7.2 Pressure Sensor

HPDLCs as pressure sensors is detailed in this section. Here pressure sensing is performed by detecting a varied optical output of HPDLCs in the presence of pressure. Also techniques to improve the pressure response is detailed here.

The Bragg equation for reflection gratings states that the reflected wavelength for normal incidence is denoted by $\lambda = 2n \cos \Lambda$, where Λ is the pathlength of the grating, n is the average refractive index of the grating. Decreasing Λ reduces the wavelength of the reflected light as seen from this equation. This concept can be applied to create an HPDLC pressure sensor. The fringe spacing is reduced by applying pressure perpendicular to the surface of the HPDLC and parallel to the grating vector. Here the wavelength reflected is measured for different applied pressure and the results are analyzed.

Reflective HPDLCs with normal reflection wavelength of $550nm$ are made with a grating pitch $\Lambda = 180nm$ thick for a normal reflecting wavelength. Due to the shrinkage observed in the HPDLC grating pitch after grating formation, the measured reflected wavelength is less than the calculated reflected wavelength by about 9%[89]. The experimental setup for testing the HPDLC for pressure sensing properties is shown in Figure 7.5. In this setup the HPDLC film is taken out of the glass slide sandwich and held firmly between two vertical mounts for mechanical strength. This setup is placed inside a well sealed box by clamping the vertical mounts to horizontal holds inside the box. An inlet to this box regulates the flow of nitrogen gas that applies the required pressure on the film. A white light source from Ocean Optics LS-1 Tungsten Halogen Lamp is incident on the film inside the pressure box, through a collimating lens using optical fibers. The reflected light of the HPDLC is measured using an Ocean Optics USB2000 spectrometer. This collects the reflected light using a detector connected via optical fibers. A focusing lens is placed in between the

HPDLC and the spectrometer detector to focus the reflected light on the detector.

A spectrometer measurement of the reflected light of the HPDLC is taken for different applied pressure ranging from 0 to 20 psi at steps of 2 psi for 1 min interval. A 1 min interval is chosen for the HPDLC to reach steady state after application of pressure. To find the optimal pressure response (highest change in the reflected wavelength) of the HPDLC, the ratio of the initiator is changed and the reflected wavelength vs. pressure is measured. The percentage of initiator composition initially taken is 5%, 10%, 14%, and 18% for di- and tri-functional polymers. Since the di-functional HPDLC shows greater pressure response compared to tri-functional polymer, an additional data point at 21% initiator composition was taken to confirm the response trend. The reflected wavelength for different pressure is noted for these variations. The procedure is repeated 3 times for each of these percentages and the average is graphed.

The spectrometer resolution is low compared to the magnitude of the shift in the mean wavelength of the pressure sensor observed. Hence a detailed numerical analysis is used to determine the pressure induced variation of the peak reflection wavelength [90]. The reflection peak is observed to be Gaussian in nature.

A Gaussian curve is fit to the reflection peak with 98% confidence level using the Kolmogorov-Smirnov Goodness of Fit test. In this method the reflection peak of the spectrometer reading is first separated, normalized and its cumulative distribution function (CDF) is taken. This result is then fit to the CDF of different Gaussian curves until a close fit of 98% confidence level is obtained. Finally, the mean of the Gaussian curve fit data is taken as the value of the peak reflected wavelength. As shown in Figure 7.6 the di-functional polymer displays a steady decrease in wavelength for a steady increase in pressure. A maximum shift rate of 0.08nm/psi was observed for an initiator percentage of 21%.

Increasing the initiator composition makes the HPDLC more elastic as can be seen for the case from 5% to 21%. This is likely due to the fact that at low initiator composition of 5% all the monomers do not polymerize completely to form the polymer matrix and the unreacted monomers hamper the elasticity. Increasing the initiator improve the polymerization. The di-functional monomers form an elastic polymer matrix which responds to applied pressure by Poisson contraction [89] along the direction parallel to the grating vector as observed for the case of 21% initiator composition. The sensitivity seen for the di- functional polymer HPDLC is graphed vs. initiator composition as shown in Figure fig:sensitivity. The sensitivity increases for 5% to 21% initiator composition. In the graph a negative value of wavelength shift seen for 5% initiator composition indicates there is an increase in wavelength with increase in pressure instead of the expected decrease in wavelength. For the initiator composition of 10%, 14%, 18% and 21% in the graph there is a decrease in wavelength with step pressure increase. This matches the expected results, where the application of pressure decreases the grating pitch and hence as observed from Bragg equation the reflected wavelength also decreases.

The HPDLCs with tri-functional polymer have not shown any notable response pattern as seen in Figure 7.8. Tri-functional polymer HPDLCs do not have a steady response to pressure as the higher cross-linking nature of the tri-functional polymer causes the film to be more brittle than elastic and thus there is no significant response.

Di-functional polymer based HPDLCs show increased response compared to tri-functional polymer HPDLCs and a maximum shift rate of 0.08nm/psi for 21% initiator composition is observed. Hence there is a relation to the functionality of the polymers Ebecryl 4833(difunctional) and Ebecryl 4866(tri-functional) and the initiator composition with respect to the pressure response of the HPDLC.

Thus imaging and pressure sensing applications were demonstrated here using

HPDLCs. The next chapter concludes the work done so far in this work on HPDLCs for wavelength sensing applications, their analysis and fundamental characterization studies.

8. Conclusion

Reconfigurable HPDLCs have application as electro-optic devices for applications such as wavelength filtering, beam steering and imaging. In this dissertation we used fundamental studies to understand their morphology and operation and fabricated novel types of HPDLCs for spectral sensing application.

The imaging and spectroscopy techniques aided in developing a further understanding of the HPDLC structure and operation. ESEM and VPSEM imaging techniques were used to interpret grating morphology in the nanometer scale. ESR spectroscopy was used to determine LC orientational order and dynamics at different temperatures.

For application development of wavelength sensing we studied and analyzed multi wavelength interacting HPDLCs formed using pixelation, stacking and a novel method of dynamic time multiplexing technique. These grating optical outputs were analyzed using the phenomenological diffusion model and Berreman 4×4 technique.

8.1 Contribution from Characterization Studies

Numerous characterization techniques are used for analyzing thin film HPDLCs. Here we have used two new microscopy and spectroscopy techniques to understand the macroscopic behavior of thin film HPDLCs by studying their microscopic properties.

8.1.1 Contribution from VPSEM and ESEM studies

Here two types of SEM imaging techniques are introduced for high resolution analysis of HPDLC morphology namely VPSEM and ESEM.

High resolution imaging techniques such as HV-SEM, TEM and Cryo-SEM used

for HPDLC analysis require removal of LC and addition of conductive coating, embedding process and complicated cryo-setup respectively. VPSEM and ESEM techniques are advantageous compared to these techniques since they require no prior sample preparation, less complicated setup and represent the true grating morphology of the HPDLC since there is no LC removal or addition of external material on to the sample for imaging.

In Section 4.1 we compared VPSEM images with the conventional HV-SEM images obtained from acrylate recipe based HPDLCs.

Post fabrication, the shrinkage of the grating structure has been observed in acrylate based HPDLCs[89]. Effect of removal of LC during imaging using conventional HV-SEM is studied here to observe if there is further grating shrinkage. This is done by using VPSEM technique. Comparing the same grating imaged by these two techniques by using an image analysis tool revealed a noticeable difference between the two types of grating for both reflection and transmission HPDLCs. The reflective HPDLCs imaged using HV-SEM showed 18.6% decrease and transmission showed HPDLCs 17.5% decrease in grating compared to VPSEM image.

This indicates air replaces the voids and there is a reduction in the grating pitch. Thus with this kind of technique we can avoid the loss of accuracy in the nanoscale structure analysis and use more accurate nanoscale parameters obtained from the images for analyzing the gratings.

HPDLCs samples were also imaged in an ESEM chamber using ambient conditions. However due to the decreased resolution obtained from this technique only the transmission HPDLC with micron scale structure were imaged with discernible features.

ESEM has lower resolution compared to HV-SEM mode but was demonstrated for use as a quick process without much sample preparation to analyze grating morphol-

ogy of transmission mode HPDLCs with discernable contrast between the polymer and LC-rich regions.

Thus the two imaging methods namely VPSEM and ESEM provide a fast and high resolution method to analyze the true morphology of the gratings without much sample modification and preparation.

8.2 Contribution from ESR studies

Using the ESR studies the molecular organization and the local fluidity of the BL038 LC inside the nano sized droplets of reflection-mode HPDLCs have been analyzed in detail. With this technique, for the first time evidence of the presence of a fraction of LC molecules with a macroscopically anisotropic LC director configuration was found. The main experimental support to this was the consistent difference between ESR spectra of field cooled samples recorded in the parallel and perpendicular geometry which could be observed in the temperature range 285.2-373.2 K (the BL038 LC bulk T_c). This result extends previous NMR studies[58, 33] which found an immobilized LC fraction, close to the polymer surface, and an isotropic fraction. The main findings from the ESR measurements combined with the inspection of the SEM images are compatible with a uniaxial LC director configuration inside elongated nanodroplets. These findings are:

• A global analysis of spectra recorded in the parallel and perpendicular geometry between 285.2 and 308.2 K clearly indicates that the macroscopic LC director configuration is unaffected by the magnetic field and has an bidimensional symmetry with the local nematic domain director uniformly distributed along the nanodroplet layers.

• Between 313.2 and 373.2 K, only in the parallel geometry, a fraction of the LC molecules forms a partially ordered polydomain aligned along the magnetic field, and

hence along the layers, which at 345.2 K becomes a nematic monodomain. When the sample is oriented in the perpendicular geometry, this aligned contribution either maintains the orientation along the layers, retaining almost the same local order (up to about 353.2 K), or it becomes isotropic (above 357.2 K); (iii) SEM images indicate that the nanodroplet shape is, on the average, elongated (prolate ellipsoid), having the direction of the elongation (nanodroplet axis) preferentially parallel to the layers.

The lack of alignment along a direction perpendicular to the droplet layers appears to be in contrast with the usual operational geometry of a reflection-mode HPDLC device, where the electric field-induced alignment should form a monodomain perpendicular to the droplet layers. Moreover, the analysis showed that the local nematic order in the H-PDLC at room temperature is smaller than that observed in the bulk BL038 LC. These findings can explain the rather large electric field needed to switch an H-PDLC device, compared to a standard PDLC device.

The reflection-mode HPDLC technology might be improved by avoiding the LC preferred orientation along the nanodroplet layers, observed at room temperature, which requires a relatively large electric field to be switched to a monodomain perpendicular to the layers. A possible strategy might be that of removing the bidimensional symmetry of the director configuration by favoring, e.g., a three dimensional polydomain director field. A key element, in such a device, would be the presence of spherical, instead of elongated, nanodroplets.

8.3 Contribution from spectral sensing and analysis studies

Three types of techniques were used to control the spectral line shape of the HPDLCs namely assembling the HPDLCs in serial and parallel configuration and using dynamic time multiplexing technique to vary the spectral line shape.

8.3.1 Contribution from assembling the HPDLCs in serial and parallel configuration

Wavelength sensing application of HPDLCs were demonstrated by arranging the HPDLCs in serial and parallel configuration in Chapter 7.

The spectral data mining with these types of devices involve apriori knowledge where the detected spectra is compared with databases for known spectra. With this type of spectrometer devices narrow banded wavelength sources can be precisely detected using line shaping algorithms [87] and it is suitable for detecting wavelengths ranging from UV to IR due to the ability to fabricate HPDLCs with Bragg wavelengths in these ranges.

Innumerable pixelated HPDLC units can be fabricated without any loss of SNR using pixelation technique. However increasing the number of units increases the complexity of the hologram fabrication setup and requires additional lasers to maintain a reasonable value of beam irradiance to form each unit cell. Hence there is a tradeoff between complicated fabrication process and wavelength range for detection.

These arrayed spectrometers have the ability to precisely detect the presence of known wavelengths for remote sensing application. For example to detect presence of life, known spectrums of water molecules can be searched to match with the HPDLC cells wavelength.

Analysis of the wavefront transmitted through the HPDLC determined optical properties such as good Strehl ratio and low aberration making them ideal for real world applications.

8.3.2 Contribution from dynamic multiplexing fabrication of HPDLCs

To broaden the optical response of single layer of HPDLC proof of concept of new methods of fabrication was demonstrated. In the dynamic multiplexing technique

the fabrication setup was varied with time. This technique doubled the FWHM of HPDLCs fabricated by normal methods. Multiple gratings were created in a single layer that caused the peak broadening effect which is evident from the SEM image analysis. The Strehl ratio which quantifies the optical quality of the grating was determined to be 0.8551 which is desirable for real world applications of the HPDLCs. This novel technique is preferable to stacking technique to increase the reflected wavelength range since it reduces the scattering losses associated with increasing thickness of the HPDLCs. Due to limitations in the speed of the rotating fabrication setup the HPDLCs were fabricated spanning two different angles. However this technique can be extended to more than two angles by using high speed rotating stages and controlling the kinetics of the grating formation resulting in more than doubling of the FWHM of the single layer. These types of broad wavelength interacting HPDLCs are useful in applications such as multispectral imaging where the wavelength sensing resolution in the range of 100nm is required. These broadened HPDLCs can be used in parallel with single wavelength reflecting HPDLCs to span a wide range of frequencies and tuned for both hyperspectral or multispectral operation. By integrating them with switchable HPDLC lenses[83] beam steering capability for instrument clusters is achieved.

8.3.3 Contribution from Berreman 4×4 matrix technique and phenomenological diffusion model

Predictive modeling using Berreman 4×4 has been applied to single peak and stacked HPDLCs to accurately simulate their optical output with the grating modeled as having a sinusoidally varying refractive index.

The broadened HPDLC lineshapes using dynamic multiplexing were also modeled using the Berreman matrix method. Here the complex refractive index profile due to

multiple gratings in a single layer was accurately modeled by describing the formation kinetics of multiple gratings using a phenomenological diffusion model.

In this dissertation we thus showed proof of concept of HPDLCs for spectral sensing applications and theoretically predicted the output. This work was accompanied by fundamental studies of HPDLC structures.

Bibliography

[1] F. Reinitzer, "Contributions to the understanding of cholesterol," *Monatshefe fur Chemie (Wien)*, vol. 9, p. 421, 1888.

[2] P. J. Collings, *Liquid Crystals: Nature's Delicate Phase of Matter*, 2nd ed. Princeton University Press, 2002.

[3] P. J. Collings and M. Hird, *Introduction to Liquid Crystals: Chemistry and Physics*. Taylor and Francis Group, 1997.

[4] S. Chandrasekhar, *Liquid Crystals*, 2nd ed. Cambridge University Press, 1992.

[5] W. de Jeu and P. Bordewijk, "Physical studies of nematic azoxybenzenes. ii. refractive indices and the internal field," *Journal of Chemical Physics*, vol. 68, no. 1, pp. 109 – 15, 1978.

[6] E. Morawitz, *Polymers:The Origins and Growth of a Science*. Wiley-Interscience,New York, 1985.

[7] L. H. Sperling, *Introduction to Physical Polymer Science*, 2nd ed. John Wiley and Sons, Inc., 1992.

[8] P. S. Drzaic, *Liquid Crystal Dispersions*. World Scientific, 1995.

[9] R. Hikmet, "Electrically induced light scattering from anisotropic gels," *Journal of Applied Physics*, vol. 68, no. 9, pp. 4406 – 12, 1990.

[10] O. Lehmann, *Flüssige Kristalle (Liquid Crystals)*. Wilhelm Engelmann, Leipzig, 1904.

[11] R. Meyer, "Piezoelectric effects in liquid crystals," *Physical Review Letters*, vol. 22, no. 18, pp. 918 – 21, 1969.

[12] E. Dubois-Violette and E. Parodi, "Emulsions nematiques. effets de champ magnetiques et effets piezoelectriques," *J. Phys. (Paris) Colloq.,*, vol. 30, no. C4, pp. 57–64, 1969.

[13] J. L. Fergason, "Encapsulated liquid crystal and method," 1984.

[14] H. Craighead, J. Cheng, and S. Hackwood, "New display based on electrically induced index matching in an inhomogeneous medium," *Applied Physics Letters*, vol. 40, no. 1, pp. 22 – 4, 1982/01/01.

[15] J. W. Doane, N. A. Vaz, B. G. Wu, and S. Zumer, "Field controlled light scattering from nematic microdroplets," *Applied Physics Letters*, vol. 48, no. 4, pp. 269–71, 1986.

[16] A. Golemme, S. Zumer, J. W. Doane, and M. E. Neubert, "Deuterium nmr of polymer dispersed liquid crystals," *Physical Review A*, vol. 37, no. 2, pp. 559–69, 1988.

[17] S. Zumer, A. Golemme, and J. Doane, "Light extinction in a dispersion of small nematic droplets," *J. Opt. Soc. Am. A, Opt. Image Sci. (USA)*, vol. 6, no. 3, pp. 403 – 11, 1989.

[18] G. Saxby, *Practical Holography*, 3rd ed. Institute of Physics Publishing, 2003.

[19] D. Gabor, "A new microscopic principle," *Nature*, vol. 161, pp. 777 – 778, 1948/05/15.

[20] Y. Denisyuk, "On the reproduction of the optical properties of an object by the wave field of its scattered radiation," *Optika i Spektroskopia*, vol. 15, no. 4, pp. 522 – 532, 1963.

[21] E. Leith and J. Upatnieks, "Wavefront reconstruction with diffused illumination and three-dimensional objects," *Optical Society of America – Journal*, vol. 54, no. 11, pp. 1295 – 1301, 1964.

[22] B. E. Saleh and M. E. Teich, *Fundamental of Photonics*, 2nd ed. John Wiley and Sons, Inc., 2007.

[23] J. D. Margerum, A. M. Lackner, E. Ramos, G. W. Smith, N. A. Vaz, J. L. Kohler, and C. R. Allison, "Polymer dispersed liquid crystal film devices, and method of forming the same," *US Patent # 4,938,568*, 1990.

[24] R. Ingwall and T. Adams, "Hologram:liquid crystal composites," vol. 1555, 1991, pp. 279 – 90.

[25] R. L. Sutherland, L. V. Natarajan, V. P. Tondiglia, and T. J. Bunning, "Bragg gratings in an acrylate polymer consisting of periodic polymer-dispersed liquid-crystal planes," *Chemistry of Materials*, vol. 5, no. 10, pp. 1533–1538, 1993.

[26] K. Tanaka, K. Kato, S. Tsuru, and S. Sakai, "Liquid-crystal/polymer optical device formed by holography for reflective color display applications," in *SID International Symposium Digest of Technical Papers*, vol. 24, 1993, pp. 109 – 111.

[27] P. Yeh, *Introduction to Photorefractive Nonlinear Optics*. John Wiley and Sons, Inc., 1993.

[28] J. Goldstein, D. E. Newbury, D. C. Joy, C. E. Lyman, P. Echlin, E. Lifshin, L. Sawyer, and J. Michael, *Scanning Electron Microscopy and X-ray Microanalysis*, 3rd ed. Springer, 2003.

[29] L. J. Berliner, *Spin Labeling, Theory and Applications*. Academic Press, 1976.

[30] E. Meirovitch and J. Freed, "Analysis of slow-motional electron spin resonance spectra in smectic phases in terms of molecular configuration, intermolecular interactions, and dynamics," *Journal of Physical Chemistry*, vol. 88, no. 21, pp. 4995 – 5004, 1984.

[31] A. Arcioni, C. Bacchiocchi, I. Vecchi, G. Venditti, and C. Zannoni, "A comparison of the effects of dispersed hydrophobic or hydrophilic aerosil nanoparticles on the order and dynamics of the 5cb liquid crystal," *Chemical Physics Letters*, vol. 396, no. 4-6, pp. 433–41, 2004.

[32] I. Vecchi, A. Arcioni, C. Bacchiocchi, G. Tiberio, P. Zanirato, and C. Zannoni, "Expected and unexpected behavior of the orientational order and dynamics induced by azobenzene solutes in a nematic," *Journal of Physical Chemistry B*, vol. 111, no. 13, pp. 3355 – 62, 2007.

[33] M. Vilfan, B. Zalar, A. K. Fontecchio, M. Vilfan, M. J. Escuti, G. P. Crawford, and S. Zumer, "Deuteron nmr study of molecular ordering in a holographic-polymer-dispersed liquid crystal," *Physical Review E (Statistical, Nonlinear, and Soft Matter Physics)*, vol. 66, no. 2, pp. 021 710–1, 2002.

[34] L. T. Muus and P. W. Atkins, *Electron Spin Relaxation in Liquids.* Plenum Press,New York, 1972.

[35] L. J. Berliner and J. Reuben, *Biological Magnetic Resonance. Spin Labeling.* Plenum Press,New York, 1989.

[36] C. Zannoni, G. Pedulli, L. Masotti, and A. Spisni, "The polyliquid crystalline epr spectra of nitroxide spin probes and their interpretation," *J. Magn. Reson. (USA)*, vol. 43, no. 1, pp. 141 – 53, 1981.

[37] E. Meirovitch, A. Nayeem, and J. Freed, "Analysis of protein-lipid interactions based on model simulations of electron spin resonance spectra," *Journal of Physical Chemistry*, vol. 88, no. 16, pp. 3454 – 65, 1984.

[38] D. E. Budil, S. Lee, S. Saxena, and J. H. Freed, "Nonlinear-least-squares analysis of slow-motion epr spectra in one and two dimensions using a modified levenberg-marquardt algorithm," *Journal of Magnetic Resonance - Series A*, vol. 120, no. 2, pp. 155 –, 1996.

[39] B. C. Platt and R. Shack, "History and principles of shack-hartmann wavefront sensing," *Journal of Refractive Surgery*, vol. 17, no. 5, pp. S573–S577, 2001.

[40] R. L. Sutherland, V. P. Tondiglia, L. V. Natarajan, P. F. Lloyd, and T. J. Bunning, "Coherent diffraction and random scattering in thiol-ene-based holographic polymer-dispersed liquid crystal reflection gratings," *Journal of Applied Physics*, vol. 99, no. 12, p. 123104, 2006.

[41] J. C. Wyant and K. Creath, *Basic Wavefront Aberration Theory for Optical Metrology*, ser. Applied Optics and Optical Engineering. Academic Press, 1992, chapter Title:Basic Wavefront Aberration Theory for Optical Metrology.

[42] S. Zumer and J. W. Doane, "Light scattering from a small nematic droplet," *Physical Review A*, vol. 34, no. 3373-86, 1986.

[43] S. Zumer, "Light scattering from nematic droplets: anomalous diffraction approach." *Physical Review A*, vol. 37, no. 4006-14, 1988.

[44] C. F. Bohren and D. R. Huffman, *Absorption and Scattering of Light by Small Particles*. Wiley-Interscience, 1998.

[45] J. Klosterman, L. Natarajan, V. Tondiglia, R. Sutherland, T. White, C. Guymon, and T. Bunning, "The influence of surfactant in reflective hpdlc gratings," *Polymer*, vol. 45, no. 21, pp. 7213 – 7218, 2004.

[46] L. Natarajan, V. Tondiglia, R. Sutherland, D. Tomlin, and T. Bunning, "Electro-optical and morphological properties of bragg transmission gratings written in holographic polymer dispersed liquid crystals by thiol-ene photopolymerization," Warrendale, PA, USA, 2003, pp. 225 – 30.

[47] L. V. Natarajan, D. P. Brown, J. M. Wofford, V. P. Tondiglia, R. L. Sutherland, P. Lloyd, R. Jakubiak, R. Vaia, and T. J. Bunning, "Visible light initiated thiol-ene based reflection h-pdlcs," ser. Proceedings of SPIE - The International Society for Optical Engineering, vol. 5936. San Diego, CA, United States: International Society for Optical Engineering, Bellingham WA, WA 98227-0010, United States, 2005, pp. 1–8.

[48] B. H. Wu, J. H. Erdmann, and J. W. Doane, "Response times and voltages for pdlc light shutters," *Liq. Crys.*, vol. 5, pp. 1453–1465, 1989.

[49] L. V. Natarajan, C. K. Shepherd, D. M. Brandelik, R. L. Sutherland, S. Chandra, V. P. Tondiglia, D. Tomlin, and T. J. Bunning, "Switchable holographic polymer-dispersed liquid crystal reflection gratings based on thiol-ene photopolymerization," *Chemistry of Materials*, vol. 15, no. 12, pp. 2477–84, 2003.

[50] D. Malacara, *Optical Shop Testing*. John Wiley and Sons, Inc., 1992.

[51] A. K. Fontecchio, "Multiplexing studies of holographically-formed polymer dispersed liquid crystals: Morphology, structure, and device applications," Ph.D. dissertation, Brown University, 2003.

[52] B. Welsh, B. Ellerbroek, M. Roggemann, and T. Pennington, "Fundamental performance comparison of a hartmann and a shearing interferometer wave-front sensor," *Appl. Opt. (USA)*, vol. 34, no. 21, pp. 4186 – 95, 1995.

[53] A. K. Fontecchio, G. P. Crawford, and D. Content, "Cavity morphology of polymer dispersed system utilizing atomic force microscopy," 2002, pp. 191 – 6.

[54] T. J. Bunning, L. V. Natarajan, V. P. Tondiglia, and R. L. Sutherland, "Holographic polymer-dispersed liquid crystals (h-pdlcs)," *Annual Review of Materials Science*, vol. 30, pp. 83–115, 2000.

[55] P. F. Lloyd, L. V. Natarajan, J. M. Wofford, R. L. Sutherland, V. P. Tondiglia, and T. J. Bunning, "Cryo-sem study of liquid crystals in a thiol-ene polymer," *Microscopy and Microanalysis*, vol. 13(Suppl 2), no. 1464-1465, 2007.

[56] G. P. Crawford and S. Zumer, *Liquid Crystals in Complex Geometries*. Taylor and Francis Group, 1996, chapter 7.

[57] A. Golemme, S. Zumer, D. W. Allender, and J. W. Doane, "Continuous nematic-isotropic transition in submicron-size liquid-crystal droplets," *Physical Review Letters*, vol. 61, no. 26, pp. 2937–40, 1988.

[58] G. S. Iannacchione, D. Finotello, L. V. Natarajan, R. L. Sutherland, V. P. Tondiglia, T. J. Bunning, and W. W. Adams, "Deuterium nmr and morphology study of polymer-dispersed liquid-crystal bragg gratings," *Europhysics Letters*, vol. 36, no. 6, pp. 425–30, 1996.

[59] J. Doane, *Liquid Crystal: Applications and Uses*. World Scientific: Singapore, 1995, vol. 1.

[60] J. D. Jackson, *Classical Electrodynamics*, 3rd ed. Wiley, 1998.

[61] D. K. Cheng, *Field and Wave Electromagnetics*, 2nd ed. Addison-Wesley Publishing Co., 1989.

[62] C. Gu and P. Yeh, "Form birefringence of layered media and volume gratings," *Journal of the Optical Society of America B: Optical Physics*, vol. 12, no. 6, pp. 1094 – 1099, 1995.

[63] M. Moharam and L. Young, "Criterion for bragg and raman-nath diffraction regimes," *Applied Optics*, vol. 17, no. 11, pp. 1757 – 9, 1978.

[64] H. Kogelnik, "Coupled wave theory for thick hologram gratings," *Bell System Technical Journal*, vol. 48, no. 9, pp. 2909–47, 1969.

[65] E. G. Loewen and E. Popov, *Diffraction Gratings and Applications*. Marcel Dekker, Inc, 1997.

[66] E. Hecht, *Optics*, 4th ed. Addison-Wesley Publishing Co., 2001.

[67] C. K. Carniglia, "Scalar scattering theory for multilayer optical coatings," *Optical Engineering*, vol. 18, no. 2, pp. 104–115, 1979.

[68] I. J. Hodgkinson and Q. H. Wu, *Birefringent Thin Films and Polarizing Elements*. World Scientific, 1997.

[69] P. Yeh, "Optics of anisotropic layered media: A new 44 matrix algebra," *Surface Science*, vol. 96, no. 41-53, 1980.

[70] D. W. Berreman and T. J. Scheffer, "Bragg reflection of light from single-domain cholesteric-liquid crystal films," *Physical Review Letters*, vol. 25, pp. 577–581, 1970.

[71] S. Teitler and B. W. Henvis, "Refraction in stratified anisotropic media," *J. Opt. Soc. Am.*, vol. 60, pp. 830–834, 1970.

[72] D. Berreman, "Optics in stratified and anisotropic media: 4x 4-matrix formulation," *Journal of the Optical Society of America*, vol. 26, no. 4, pp. 502–10, 1972.

[73] E. N. Bramley and P. Bos, "Modeling volume holograms using berreman 4 x 4 method," vol. 4296. SPIE-Int. Soc. Opt. Eng, 2001, pp. 282–91.

[74] A. K. Fontecchio, C. C. Bowley, S. M. Chmura, L. Le, S. Faris, and G. P. Crawford, "Multiplexed holographic polymer dispersed liquid crystals," *Journal of Optical Technology*, vol. 68, no. 9, pp. 652–6, 2001.

[75] K. Tanaka, K. Kato, S. Tsuru, and S. Sakai, "Holographically formed liquid-crystal/polymer device for reflective color display," *Journal of the Society for Information Display*, vol. 2, no. 1, pp. 37–40, 1994.

[76] V. K. S. Hsiao, T.-C. Lin, G. S. He, A. N. Cartwright, P. N. Prasad, L. V. Natarajan, V. P. Tondiglia, and T. J. Bunning, "Optical microfabrication of highly reflective volume bragg gratings," *Applied Physics Letters*, vol. 86, no. 13, p. 131113, 2005.

[77] C. C. Bowley, A. K. Fontecchio, G. P. Crawford, L. Jau-Jeng, L. Le, and S. Faris, "Multiple gratings simultaneously formed in holographic polymer-dispersed liquid-crystal displays," *Applied Physics Letters*, vol. 76, no. 5, pp. 523–5, 2000.

[78] G. H. Zhao and P. Mouroulis, "Diffusion-model of hologram formation in dry photopolymer materials," *J. Mod. Opt.*, no. 1929-1939, 1994.

[79] V. L. Colvin, R. G. Larson, A. L. Harris, and M. L. Schilling, "Quantitative model of volume hologram formation in photopolymers," *J. Appl. Phys. (USA)*, vol. 81, no. 9, pp. 5913–5923, 1997.

[80] C. C. Bowley and G. P. Crawford, "Diffusion kinetics of formation of holographic polymer-dispersed liquid crystal display materials," *Appl. Phys. Lett. (USA)*, vol. 76, no. 16, pp. 2235–2237, 2000.

[81] J. Qi, M. E. Sousa, A. K. Fontecchio, and G. P. Crawford, "Temporally multiplexed holographic polymer-dispersed liquid crystals," *Applied Physics Letters*, vol. 82, no. 11, pp. 1652–1654, 2003.

[82] D. R. Cairns, C. C. Bowley, S. Danworaphong, A. K. Fontecchio, G. P. Crawford, L. Li, and S. M. Faris, "Optical strain characteristics of holographically formed polymer-dispersed liquid crystal films," *Applied Physics Letters*, vol. 77, no. 17, pp. 2677–9, 2000.

[83] M. L. Ermold and A. K. Fontecchio, "Electrically switchable holographic parabolic mirrors," *Journal of Applied Physics*, vol. 99, no. 9, pp. 093 111–5, 2006.

[84] L. H. Domash, C. Yong-Ming, B. Gomatam, C. M. Gozewski, R. L. Sutherland, L. V. Natarajan, V. P. Tondiglia, T. J. Bunning, and W. W. Adams, "Switchable-focus lenses in holographic polymer dispersed liquid crystal," ser. Proc. SPIE - Int. Soc. Opt. Eng. (USA), vol. 2689. San Jose, CA, USA: SPIE-Int. Soc. Opt. Eng, 1996, pp. 188–94.

[85] L. Domash, G. Crawford, A. Ashmead, R. Smith, M. Popovich, and J. Storey, "Holographic pdlc for photonic applications," ser. Proceedings of SPIE - The International Society for Optical Engineering, vol. 4107. San Diego, CA, USA: Society of Photo-Optical Instrumentation Engineers, Bellingham, WA, USA, 2000, pp. 46–58.

[86] J. W. McMurdy, G. P. Crawford, G. D. Jay, and S. Suner, "A novel medical diagnostic tool for non-invasively measuring hemoglobin utilizing switchable h-pdlc display technology," ser. Digest of Technical Papers - SID International Symposium, vol. 36. Boston, MA, United States: Society for Information Display, San Jose, CA 95112-4006, United States, 2005, pp. 364–367.

[87] A. E. Fox, K. Rai, and A. K. Fontecchio, "Holographically formed polymer dispersed liquid crystal films for transmission mode spectrometer applications," *Applied Optics*, vol. 46, no. 25, pp. 6277–6282, 2007.

[88] S. K. Shriyan, K. K. Rai, A. Bellingham, and A. K. Fontecchio, "Multilayer stacking technique for holographic polymer dispersed liquid crystals," *Applied Physics Letters*, vol. 93, no. 26, 2008.

[89] Q. Jun, M. DeSarkar, G. T. Warren, and G. P. Crawford, "In-situ shrinkage measurement of holographic polymer dispersed liquid crystals," *Journal of Applied Physics*, vol. 91, no. 8, pp. 4795–800, 2002.

[90] M. L. Ermold, K. Rai, and A. K. Fontecchio, "Hydrostatic pressure response of polymer-dispersed liquid crystal gratings," *Journal of Applied Physics*, vol. 97, no. 10, pp. 104 905–1, 2005.

Vita

Education

Ph.D., Electrical Engineering, Drexel University, Philadelphia, PA, USA, 2009
M.S., Electrical Engineering, Drexel University, Philadelphia, PA, USA, 2006
B.E., Electrical Engineering, BMS College of Engineering, Bangalore, India, 2001

Professional Experience

Ph.D. Research Fellow, Drexel University, 09/2004 - 09/2009
Graduate Teaching Assistant, Drexel University, 09/2003- 12/2008

Publications

1. Variable Pressure and Environmental SEM of Thin-Film Liquid Crystal/Polymer Composites, *Kashma K Rai, Sameet K. Shriyan and Adam K Fontecchio*, Microscopy and Microanalysis, 23, Issue 5, 17 (2009)
2. Order and Dynamics Inside H-PDLC Nanodroplets: an ESR Spin Probe Study, *Corrado Bacchiocchi, Isabella Miglioli, Alberto Arcioni, Ilaria Vecchi, Kashma Rai, Adam Fontecchio and Claudio Zannoni*, Journal of Physical Chemistry B, 113, 5391 (2009)
3. Multilayer Stacking Technique for Holographic Polymer Dispersed Liquid Crystals, *Sameet Shriyan, Kashma Rai, Alyssa Bellingham and Adam K Fontecchio*, Applied Physics Letters, 93, 261113 (2008)
4. Holographically Formed Polymer Dispersed Liquid Crystal Films for Transmission Mode Spectrometer Applications, *Anna E. Fox, Kashma Rai and Adam K. Fontecchio*, Applied Optics, 46, 6277 (2007)
5. Optimization of Pressure Response in HPDLC Grating Films Based on Polymer Composition, *Kashma Rai and Adam K. Fontecchio*, Molecular Crystals and Liquid Crystals, 450, 183 (2006)
6. Hydrostatic Pressure Response of Polymer-Dispersed Liquid Crystal Gratings, *Michael L. Ermold, Kashma Rai, and Adam K. Fontecchio*, Journal of Applied Physics, 97, 104905 (2005)

Patent

• Dynamic Time Multiplexing Fabrication of Holographic Polymer Dispersed Liquid Crystals for Increased Wavelength Sensitivity, *Adam K. Fontecchio, Kashma K. Rai*, Docket no: DXU-0278/08-1029D, *U.S. Patent Pending*